Abstract

R. Scott Brock MODELING LIGHT SCATTERING FROM BIOLOGICAL CELLS USING A FINITE-DIFFERENCE TIME DOMAIN METHOD. (Under the direction of Dr. Jun Q. Lu) Department of Physics, January 2007.

The effect of cell morphology on light scattering is investigated using computer simulations. A parallel implementation of the finite-difference time domain (FDTD) method has been developed to simulate the scattering and obtain various scattering properties such as the Mueller matrix and anisotropy factor. In addition, a program which produces 3D cell models for the FDTD program has been developed. Scattering from realistic red blood cell (RBC) and B-cell precursor (B-cell) models has been simulated and the results are compared with those of the simpler sphere and coated sphere models. The RBC models are based on models developed from mechanical principles which impose constraints on the volume and surface area of an RBC under pressure. The B-cell models are created by taking confocal microscopy images of cultured NALM6 cells and applying statistical and geometric methods to produce a realistic 3D model. Validation of the FDTD program against Mie theory results are presented along with performance evaluations on three different parallel computing platforms. Simulations of the more realistic cell models show that the sphere models are not suitable for determining most of the scattering properties; however, a more complex ellipsoid model provides a good approximation for some scattering properties. It was also found that the amount of forward scattered light is closely related to the volume of the cell, while light scattered toward the side is more closely related to the refractive index. Simulations using various nucleus models show that the complexity of the shape of the nucleus and its relative refractive index influence the light scattering in various ways. A comparison with experimental results for cultured NALM6 cells is also presented.

MODELING LIGHT SCATTERING FROM BIOLOGICAL CELLS USING A FINITE-DIFFERENCE TIME DOMAIN METHOD

A Dissertation
Presented to
the Faculty of the Department of Physics
East Carolina University

In Partial Fulfillment
of the Requirements for the Degree
Doctor of Philosophy in Biomedical Physics

by
R. Scott Brock
July 17, 2007

MODELING LIGHT SCATTERING FROM BIOLOGICAL CELLS USING A FINITE-DIFFERENCE TIME DOMAIN METHOD

by

R. Scott Brock

APPROVED BY:

DIRECTOR OF DISSERTATION	Dr. Jun Q. Lu
COMMITTEE MEMBER	Dr. Xin-Hua Hu
COMMITTEE MEMBER	Dr. James M. Joyce
COMMITTEE MEMBER	Dr. Mark W. Sprague
COMMITTEE MEMBER	Dr. Mary A. Farwell
CHAIR OF THE DEPARTMENT OF PHYSICS	Dr. John C. Sutherland
DEAN OF THE GRADUATE SCHOOL	Dr. Patrick J. Pellicane

Dedicated to Ronald G. Hardy (1937–2006)

“Now he has departed from this strange world a little ahead of me. That means nothing. People like us, who believe in physics, know that the distinction between past, present, and future is only a stubbornly persistent illusion.” – A. Einstein

Acknowledgments

I would like to thank the faculty, staff, and graduate students of the Physics Department for their help with my graduate studies. In addition, thanks go to the following: Professor F. E. Bertrand and Dr. Douglas Weidner for providing the cells and confocal images used in this study. Drs. Xin-Hua Hu and Huafeng Ding for providing the experimental results. Dr. Ping Yang for providing a serial FDTD code. Mr. Maxim Yurkin for some discussion which led to improvements in the FDTD code.

I would also like to acknowledge support through NIH grant 1R15GM70798-01 and various grants for computing resources from Teragrid.org, the San Diego Supercomputing Center, the North Carolina Supercomputing Center, the Pittsburgh Supercomputing Center, and the Texas Advanced Computing Center.

Finally, I would like to thank Dr. Jun Q. Lu for her knowledge and patience during my graduate studies, and in particular for her help and guidance with my dissertation research.

Contents

List of Tables

List of Figures

Chapter 1: Introduction

Light scattering occurs when inhomogeneity exists in the path of incident light[2]. The scattering of light by small particles, i.e., particles with a size parameter comparable to the wavelength, is of great interest for a wide range of applications, such as atmospheric scattering[46], scattering by interstellar gas clouds[12], and various biomedical studies[19]. In the context of biomedical physics, it is widely recognized that light scattering by a single cell of inhomogeneous body is very sensitive to its morphology. Thus, the scattered light from a cell may provide a means for determining the characteristics of cell morphology.

Recent research activities in cell scattering have shown that different types of cells can be associated with different scattering patterns. In 1998, the work of Mourant et al. [30] showed that tumorigenic cells, M1 cells, and nontumorigenic cells, MR1 cells, have differences in scattering properties, and it was concluded that at least part of this difference could be attributed to the difference in cell sizes. Drezek et al. [14] combined numerical and experimental approaches in the study of both ovarian cancer cells, OVCA-420 cells, and cervical cancer cells, He-La cells, and concluded that the biochemical and morphological structure of the cells “strongly influenced” the scattering properties. Other research results are related to the improvement of cell modeling. Backman et al. [1] have used experimental data fitted to theoretical models to show that scattered light measurements can be used to “give accurate quantitative estimates” of the size distribution of cell nuclei and that “additional information” is obtained about the refractive indices of cell organelles. In another recent report on cell scattering measurements and data modeling, Mourant et al. [31] used three different polarization configurations, i.e., parallel, perpendicular and cross polarization, when measuring the angular distribution of the scattered light from epithelial cells and isolated cell nuclei. With the aid of analytic models, i.e., Mie theory and T-matrix method, that research provided useful information about refractive index structure variations in epithelial cells and in isolated cell nuclei.

In order to maximize the potential of light scattering analysis as a tool for noninvasive probing of cell morphology, accurate modeling of light-cell interaction is needed. However, light scattering from a biological cell is a complex phenomenon. In general, biological cells are dielectric bodies with an inhomogeneous spatial distribution in their refractive index. Thus, modeling the interaction requires the ability to account for the inhomogeneous distributions. Also, biological cell size parameters range from 0.1 to 100, where the size parameter, x, is defined as $x = 2\pi a/\lambda$ where $2a$ is the characteristic dimension of the scatterer and λ is the wavelength of the incident light. This size parameter range falls between the acceptable sizes for the Rayleigh approximation ($x \ll 1$) and those of geometric optics ($x \gg 1$). This size range requires that the modeling account for the wave nature of light and thus must be based on the Maxwell equations.

In early studies, Mie theory has been used extensively to understand light scattering at the cellular level[2]. Mie theory provides an analytic solution to the problem of light scattering by a homogeneous sphere. More recently, the anomalous diffraction approximation[39], multipole solutions[45], the T-matrix[32] method, the discrete dipole approximation (DDA)[19, 20], and the finite-difference time domain method[41] have been used to study cells with more realistic shapes. Although each of these techniques offers some advantages over Mie theory, most require some geometric or refractive-index contrast limitations that do not apply to the wide range of shapes and refractive indices found in a cell. Mie theory and many implementations of the T-matrix method require symmetries in the scattering particle. The anomalous diffraction approximation used by Streekstra et al. [39] is restricted to a size parameter

$x \gg 1$ and a relative refractive index $|m-1| \ll 1$. The multipole solutions of Videen and Ngo [45] require effective medium substitutions for “more complicated systems containing additional irregularities”[45], i.e., complex media must be replaced with media having a single refractive index to approximate the net effect of the original media.

From the research previously mentioned and other similar ongoing research, it is clear that light scattering from biological cells is a complex phenomenon. The primary goal of this research is to contribute to the understanding of this phenomenon and obtain information that is pertinent to furthering research in biomedical optics.

One of the objectives contributing to this goal is producing a high-performance numerical tool to model light interaction with biological cells. This tool is in the form of a Fortran 90 implementation of the finite-difference time domain (FDTD) method. The FDTD method has been chosen for this research due to the ability to handle a wide range of scattering particles. The FDTD method does not require symmetry in the scattering particles and can handle a wide range of refractive indices. Alternatives to the FDTD method which have some of the same advantages as FDTD are the DDA and the pseudo-spectral time domain method (PSTD). Like FDTD these methods are not restricted to particles having particular symmetries. As mentioned previously, the DDA has already been applied to scattering by biological cells[19, 20]. The PSTD method is similar to the FDTD method, but it also uses the spectral components directly in the solution of the scattering problems. In addition to the reasons already mentioned, FDTD was chosen because of the decades of development of the method that had occurred prior to the start of this research and due to its simplicity. The core of the FDTD method is finite differencing which is both easy to understand and implement. The program has been developed using many of the methods of the well-tested serial code developed by Yang and Liou [46] to study light scattering by atmospheric ice crystals. The development process includes creating the code, verifying results obtained, and evaluating the performance of the code.

Since the time required for the FDTD method increases cubically with the problem size and biological cells can have a size parameter as large as 100, it is practical to use parallel computational methods to increase the amount of computational resources that can be utilized simultaneously. As previous studies have shown[44, 11, 16, 26, 15, 21], parallel computational methods reduce the amount of time needed to acquire results by allowing portions of the calculations to be carried out simultaneously. Parallel FDTD methods have been used previously on a wide variety of platforms including shared-memory systems[7], massively parallel systems[34, 33, 18], and workstation clusters[44]. In each of these cases, FDTD showed "excellent speedups"[40]. The parallel implementation used in this research is a simplification of that described by Taflove [40] and is discussed in detail in chapter 5. The communications for the parallel program are implemented using the Message Passing Interface (MPI) standard.

Another objective is to use the code to simulate the light scattering from biological cells. To satisfy this objective, cell models must be created from information known about the cells. In the case of the RBC, the analysis of Zarda et al. [49] of RBCs under various pressure gradients has been used to create Fortran 90 code which will generate RBC models. For the NALM6 cells, confocal images of NAML6 cells have been obtained, and two other Fortran 90 codes have been written. One of these uses the confocal images to obtain the data necessary to construct a cell model; the other code uses the data obtained to construct the cell model.

The results of this research will contribute to the basic understanding of light interaction with biological cells. In particular, results for scattering from RBCs[5, 25] and NALM6[6, 13] cells has already been obtained. It provides not only these results, but also the information about the performance and accuracy of an implementation of the FDTD method. This will help other researchers in deciding which of the many methods available is suitable for their light scattering research. In addition, further understanding of light-cell interaction will contribute to research methods and interests such as flow cytometry[4, 29], Monte-Carlo modeling of light[27, 10], and possibly even to the diagnosis and treatment of illness or disease.

The remainder of this document is organized in four parts. The first part, chapter 2, contains a description of the physics theory necessary for this research. The second part, chapters 3–6, describes the numerical methods used in this research. The third part, chapters 7–9, presents the results of various numerical calculations which have been carried out. The final part is the conclusion which summarizes the various parts.

Chapter 2: Scattering Theory

In general biological cells have size parameters ranging from 0.1 to 100. Thus, the investigation of light scattering from these cells must consider the wave nature of light. The fundamental equations describing this nature are the Maxwell equations. Using the Maxwell equations, mathematical models are derived to describe the various characteristics of the scattered light. Using these characteristics, comparisons can be made between various particles to better understand the interaction between light and biological cells. The first section of this chapter gives a description of the physical system involved and the assumptions made about this system. Using this description, an equation describing the scattered light is obtained. The second and final section uses the equation derived to define properties of the scattered light which are useful in analyzing the light-cell interaction. All of the definitions and derivations outlined in this chapter are the result of previous work done in the field of electrodynamics and are accepted practices in this field.

2.1 The model system

The system consists of an infinite homogeneous medium containing a scattering particle interacting with an electromagnetic field as shown in Fig. 1. By the superpositioning principle, the field, $\{\mathbf{E}, \mathbf{H}\}$, can be divided into two parts. The first is the incident field, $\{\mathbf{E}_i, \mathbf{H}_i\}$, which is the field as it exists in the absence of the scattering particle. The second is the scattered field, $\{\mathbf{E}_s, \mathbf{H}_s\}$, which is the difference between the existing field and the incident field, $\{\mathbf{E}, \mathbf{H}\} - \{\mathbf{E}_i, \mathbf{H}_i\}$. The incident field is a plane wave with wavenumber vector $\mathbf{k}_i$. The infinite homogeneous medium, referred to as the host medium, has permeability μ_0 and permittivity ε_0 and is non-absorbing,

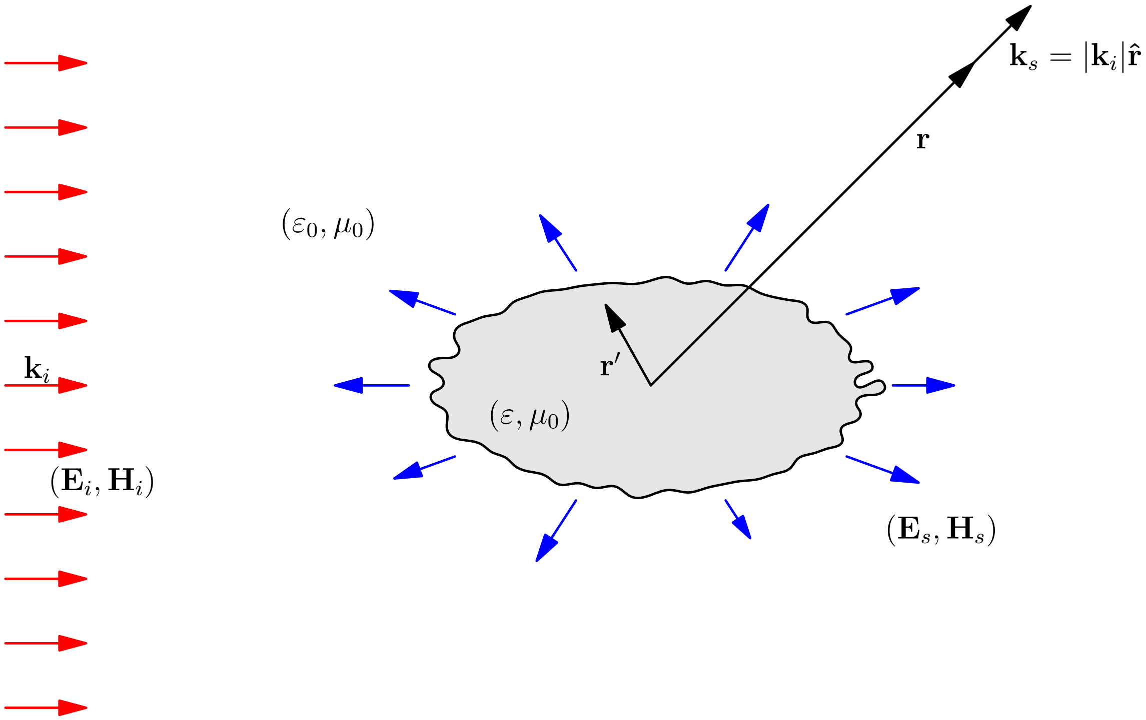

Figure 1: The model system consists of an electromagnetic field interacting with a scattering particle characterized by its permittivity, ε, embedded in a host medium with permittivity ε_0. The incident field, $\{\mathbf{E}_i, \mathbf{H}_i\}$, is a plane wave with wavenumber vector $\mathbf{k}_i$. The scattered field, $(\mathbf{E}_s, \mathbf{H}_s)$, is unknown. The vectors $\mathbf{k}_s$, $\mathbf{r}$, and $\mathbf{r}'$ are shown for reference.

$\Im(\varepsilon_0), \Im(\mu_0) = 0$. The scattering particle is non-permeable, $\mu = \mu_0$, and is characterized by its permittivity, ε. The scattered electric field, $\mathbf{E}_s$, is to be determined.

2.2 The far field solution

The Helmholtz equation for the electric field, $\mathbf{E} = \mathbf{E}_i + \mathbf{E}_s$, is

$$\begin{gathered} \left(\nabla^2 + k^2\right) \mathbf{E}(\mathbf{r}) = -4\pi \mathbf{f}(\mathbf{r}) \\ \mathbf{f}(\mathbf{r}) = \frac{1}{4\pi} \left(\nabla^2 + k^2\right) \left(\frac{\varepsilon(\mathbf{r})}{\varepsilon_0} - 1\right) \mathbf{E}(\mathbf{r}) \end{gathered}, \tag{2.1}$$

where $k = |\mathbf{k}_i|$. Applying the second Green identity with the free space Green's function, G, to Eq. (2.1); and using the fact that the scattered field vanishes at an infinite distance, $\lim_{|\mathbf{r}|\to\infty} \mathbf{E}_s(\mathbf{r}) = 0$, yields

$$\begin{array}{c} \mathbf{E}(\mathbf{r}) = \mathbf{E_i}(\mathbf{r}) + \displaystyle\int_V \mathbf{f}(\mathbf{r}') \, G(\mathbf{r}, \mathbf{r}') \, d^3 r' \\ G(\mathbf{r}, \mathbf{r}') = \dfrac{e^{ik|\mathbf{r}-\mathbf{r}'|}}{4\pi |\mathbf{r}-\mathbf{r}'|} \end{array} , \tag{2.2}$$

where V is the region occupied by the scattering particle. From Eq. (2.2) it is clear that the second term on the right-hand side is the scattered field. In the far field, the limiting form of G,

$$\lim_{kr\to\infty} G(\mathbf{r}, \mathbf{r}') \sim \frac{e^{ikr}}{r} , \tag{2.3}$$

is used along with Eq. (2.2) to give the scattered field

$$\begin{array}{c} \mathbf{E_s}(\mathbf{r}) = \mathbf{F}(\mathbf{k_i}, \mathbf{k_s}) \dfrac{e^{ikr}}{r} \\ \mathbf{F}(\mathbf{k_i}, \mathbf{k_s}) = \dfrac{1}{4\pi} \displaystyle\int_V \left(\nabla^2 + k^2\right) \left(\frac{\varepsilon(\mathbf{r}')}{\varepsilon_0} - 1\right) \mathbf{E}(\mathbf{r}') \, e^{i\mathbf{k_s}\cdot\mathbf{r}'} d^3 r' \end{array} . \tag{2.4}$$

The arguments $\mathbf{k}_s = k\hat{\mathbf{r}}$ and $\mathbf{k}_i$ are explicitly shown to emphasize the dependence on both the direction of the incident field and the direction of scattering. It has been shown that the Helmholtz equation in a dielectric medium can be written[17]

$$\left(\nabla^2 + k^2\right) \mathbf{E} = -\left(k^2 \mathbf{I} + \nabla\nabla\right) \cdot \left(\left(\frac{\varepsilon}{\varepsilon_0} - 1\right) \mathbf{E}\right) , \tag{2.5}$$

where $\mathbf{I}$ is the unit dyad. Eq. (2.4) and (2.5) together yield

$$\mathbf{F}(\mathbf{k_i}, \mathbf{k_s}) = \frac{k^2}{4\pi} \int_V \left(\left(\frac{\varepsilon(\mathbf{r}')}{\varepsilon_0} - 1\right) \mathbf{E}(\mathbf{r}') - \hat{\mathbf{r}}\hat{\mathbf{r}} \cdot \mathbf{E}(\mathbf{r}')\right) e^{i\mathbf{k_s}\cdot\mathbf{r}'} d^3 r' . \tag{2.6}$$

From Eq. (2.4) and (2.6), it is clear that the scattered field is related to both the shape of the scattering particle, V, and the distribution of the permittivity, $\varepsilon\left(\mathbf{r}'\right)$, within the region of the scattering particle. Thus, particles which differ in either of these properties will, in general, have scattered fields that also differ.

2.3 Scattered field properties

Using the model discussed in the previous section, the scattered field can be determined when given an incident field, a host medium, and a scattering particle. However, direct comparison of the scattered fields for different input factors is not practical. Instead, several scattered field properties can be derived to which a physical meaning can be attached. Comparison of these properties allows a better analysis of how the various input factors affect the light scattering. In particular, the Mueller matrix, an angle dependent property, and the anisotropy factor and cross-sections, scalar properties, are used to compare the results of various scattering simulations.

Calculation of the Mueller matrix begins by first calculating the scattering amplitude matrix, $\mathbf{S}$. The scattering amplitude matrix gives a general relation between the scattered field and a plane wave of arbitrary polarization. Using the geometry shown in Fig. 2, this relationship is

$$\begin{pmatrix} E_{\alpha,s} \\ E_{\beta_s,s} \end{pmatrix} = \frac{e^{ikr}}{r} \begin{pmatrix} S_2 & S_3 \\ S_4 & S_1 \end{pmatrix} \begin{pmatrix} E_{\alpha,i} \\ E_{\beta_i,i} \end{pmatrix}, \tag{2.7}$$

where $\hat{\mathbf{e}}_\alpha \perp \hat{\mathbf{e}}_{\beta_s}$, $\hat{\mathbf{e}}_\alpha \times \hat{\mathbf{e}}_{\beta_s} = \hat{\mathbf{k}}_s$, $\hat{\mathbf{e}}_\alpha \perp \hat{\mathbf{e}}_{\beta_i}$, $\hat{\mathbf{e}}_\alpha \times \hat{\mathbf{e}}_{\beta_i} = \hat{\mathbf{k}}_i$, the 2×2 matrix is $\mathbf{S}$, $\mathbf{E}_i = E_{\alpha,i}\hat{\mathbf{e}}_\alpha + E_{\beta,i}\hat{\mathbf{e}}_{\beta_i}$, and $\mathbf{E}_s = E_{\alpha,s}\hat{\mathbf{e}}_\alpha + E_{\beta,s}\hat{\mathbf{e}}_{\beta_s}$. Note that the relationship between the scattered and incident fields is given in terms of components perpendicular and

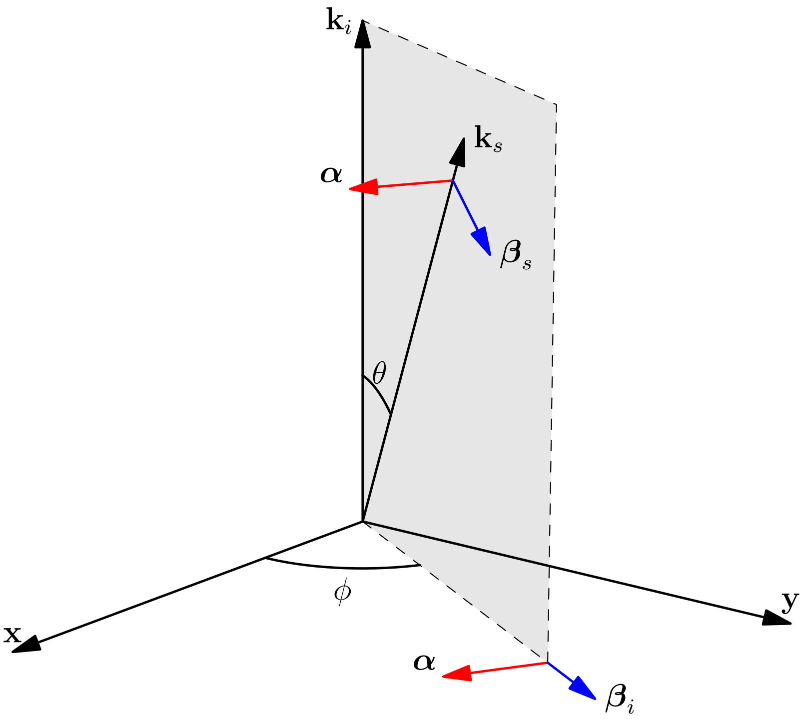

Figure 2: The scattering amplitude matrix is expressed in relation to the scattering plane, shown in grey. θ and ϕ give the polar and azimuthal angles, respectively, of $\mathbf{k}_s$ with respect to $\mathbf{k}_i$. The scattering plane is normal to $(-\sin(\phi), \cos(\phi))$. $\{\hat{\mathbf{e}}_x, \hat{\mathbf{e}}_y, \hat{\mathbf{e}}_{k_i}\}$, $\{\hat{\mathbf{e}}_\alpha, \hat{\mathbf{e}}_{\beta_i}, \hat{\mathbf{e}}_{k_i}\}$, and $\{\hat{\mathbf{e}}_\alpha, \hat{\mathbf{e}}_{\beta_s}, \hat{\mathbf{e}}_{k_s}\}$ are Cartesian basis sets for the various coordinate systems used.

parallel to the scattering plane, thus allowing a 2×2 matrix. Using the $(\hat{\mathbf{e}}_\alpha, \hat{\mathbf{e}}_{\beta_s}, \hat{\mathbf{e}}_{k_s})$ also simplifies Eq. (2.6) by eliminating the second term of the kernel, since $\alpha, \beta \perp \mathbf{r}$. From the geometry, a matrix $\mathbf{R}$ can be defined

$$\begin{gathered}\begin{pmatrix} E_{\alpha,i} \\ E_{\beta_i,i} \end{pmatrix} = \mathbf{R} \begin{pmatrix} E_{x,i} \\ E_{y,i} \end{pmatrix} \\ \mathbf{R} = \begin{pmatrix} \hat{\beta}_i \cdot \hat{\mathbf{e}}_x & -\hat{\beta}_i \cdot \hat{\mathbf{e}}_y \\ \hat{\beta}_i \cdot \hat{\mathbf{e}}_y & \hat{\beta}_i \cdot \hat{\mathbf{e}}_x \end{pmatrix} = \begin{pmatrix} \cos(\phi) & -\sin(\phi) \\ \sin(\phi) & \cos(\phi) \end{pmatrix}\end{gathered}, \tag{2.8}$$

which transforms vector components from the $\left\{\hat{\mathbf{e}}_x, \hat{\mathbf{e}}_y, \hat{\mathbf{k}}_i\right\}$ basis to the $\left\{\hat{\mathbf{e}}_\alpha, \hat{\mathbf{e}}_{\beta_i}, \hat{\mathbf{k}}_i\right\}$

basis. Applying Eq. (2.8) to Eq. (2.7) gives

$$\begin{pmatrix} E_{\alpha,s} \\ E_{\beta,s} \end{pmatrix} = \frac{e^{ikr}}{r}\mathbf{S}\,\mathbf{R}\begin{pmatrix} E_{x,i} \\ E_{y,i} \end{pmatrix}, \tag{2.9}$$

where $\mathbf{E}_i = E_{x,i}\hat{\mathbf{e}}_x + E_{y,i}\hat{\mathbf{e}}_y$. Notice that to find $\mathbf{S}$, four equations are needed. Using Eq. (2.6) will provide two equations, one for each element of $\mathbf{F}$. Thus, Eq. (2.6) must be used twice to get the necessary information, and each result for $\mathbf{F}$ must be linearly independent. So, using Eq. (2.9) and Eq. (2.6), the relation between $\mathbf{F}$ and $\mathbf{S}$ is determined by using two incident fields having orthogonal polarization vectors,

$$\mathbf{S} = \frac{1}{|E_i|}\begin{pmatrix} F_\alpha\big|_{\mathbf{E}_i=E_i\hat{\mathbf{e}}_y} & F_\alpha\big|_{\mathbf{E}_i=E_i\hat{\mathbf{e}}_x} \\ F_\beta\big|_{\mathbf{E}_i=E_i\hat{\mathbf{e}}_y} & F_\beta\big|_{\mathbf{E}_i=E_i\hat{\mathbf{e}}_x} \end{pmatrix}\mathbf{R}^{-1}, \tag{2.10}$$

where $\mathbf{F} = F_\alpha\hat{\mathbf{e}}_\alpha + F_\beta\hat{\mathbf{e}}_{\beta_s}$, or using Eq. (2.6),

$$\mathbf{F}(\mathbf{k_i},\mathbf{k_s}) = \frac{k^2}{4\pi r}\int_V\left(\frac{\varepsilon(\mathbf{r}')}{\varepsilon_0}-1\right)\begin{pmatrix} \hat{\mathbf{e}}_\alpha\cdot\mathbf{E}(\mathbf{r}') \\ \hat{\mathbf{e}}_\beta\cdot\mathbf{E}(\mathbf{r}') \end{pmatrix}e^{i\mathbf{k_s}\cdot\mathbf{r}'}d^3r'. \tag{2.11}$$

.

Although the scattering amplitude matrix gives the desired relation for an arbitrary polarization, it is more practical to use the Mueller matrix, $\mathbf{M}$, to relate the scattered and incident fields by their Stokes vectors. This relation is expressed as

$$\begin{pmatrix} I_s \\ Q_s \\ U_s \\ V_s \end{pmatrix} = \begin{pmatrix} S_{11} & S_{12} & S_{13} & S_{14} \\ S_{21} & S_{22} & S_{23} & S_{24} \\ S_{31} & S_{32} & S_{33} & S_{34} \\ S_{41} & S_{42} & S_{43} & S_{44} \end{pmatrix}\begin{pmatrix} I_i \\ Q_i \\ U_i \\ V_i \end{pmatrix}, \tag{2.12}$$

where the 4×4 matrix is $\mathbf{M}$; and $I, Q, U,$ and V form the Stokes vector. One reason this is more practical is that the Stokes vector components can be calculated directly from intensity measurements obtained experimentally. This allows for a direct comparison with experimental results. Another reason is that several of the Mueller matrix elements can be given a clear physical meaning. For example, S_{11} gives the intensity of the scattered light. The components of $\mathbf{M}$ are related to the components of $\mathbf{S}$ by

$$\begin{aligned}
S_{11} &= \frac{1}{2}\left(|S_1|^2 + |S_2|^2 + |S_3|^2 + |S_4|^2\right) \\
S_{12} &= \frac{1}{2}\left(|S_1|^2 - |S_2|^2 + |S_3|^2 - |S_4|^2\right) \\
S_{13} &= \mathrm{Re}\left(S_2 S_3^* + S_1 S_4^*\right) \\
S_{14} &= \mathrm{Im}\left(S_2 S_3^* + S_1 S_4^*\right) \\
S_{21} &= \frac{1}{2}\left(|S_2|^2 - |S_1|^2 - |S_4|^2 + |S_3|^2\right) \\
S_{22} &= \frac{1}{2}\left(|S_2|^2 + |S_1|^2 - |S_4|^2 - |S_3|^2\right) \\
S_{23} &= \mathrm{Re}\left(S_2 S_3^* - S_1 S_4^*\right) \\
S_{24} &= \mathrm{Im}\left(S_2 S_3^* - S_1 S_4^*\right) \\
S_{31} &= \mathrm{Re}\left(S_2 S_4^* + S_1 S_3^*\right) \\
S_{32} &= \mathrm{Re}\left(S_2 S_4^* - S_1 S_3^*\right) \\
S_{33} &= \mathrm{Re}\left(S_1 S_2^* + S_3 S_4^*\right) \\
S_{34} &= \mathrm{Im}\left(S_2 S_1^* + S_4 S_3^*\right) \\
S_{41} &= \mathrm{Im}\left(S_4 S_2^* + S_1 S_3^*\right) \\
S_{42} &= \mathrm{Im}\left(S_4 S_2^* - S_1 S_3^*\right) \\
S_{43} &= \mathrm{Im}\left(S_1 S_2^* - S_3 S_4^*\right) \\
S_{44} &= \mathrm{Re}\left(S_1 S_2^* - S_3 S_4^*\right)
\end{aligned} \quad . \tag{2.13}$$

Thus, once **S** is calculated, **M** is easily determined. As mentioned previously, the Mueller matrix is the only angle dependent property used for comparing scattered fields.

The anisotropy factor, g, is among the scalar properties that will be used for comparisons. It is calculated from the S_{11} element of the Mueller matrix by

$$g = \frac{\int_0^{\frac{\pi}{2}} \int_0^{2\pi} \mathbf{S}_{11}(\theta, \phi) \cos(\theta) d\phi d\theta}{\int_0^{\frac{\pi}{2}} \int_0^{2\pi} \mathbf{S}_{11}(\theta, \phi) d\phi d\theta} \,. \tag{2.14}$$

Since S_{11} represents intensity, g indicates where the energy is scattered on average. For example, $g = 1$ indicates complete forward scattering; and $g = -1$ indicates complete backward scattering. The anisotropy factor is useful not only for comparisons; it can also be used in random walk simulations of photons as a parameter to select a particular function from a family of phase functions, e.g., the Henyey-Greenstein function.

The other scaler properties that will be used for comparison are the absorption, extinction, and scattering cross sections; σ_a, σ_e, and σ_s, respectively. The first of these, σ_a, can be derived from the Poynting theorem,

$$-\nabla \cdot \mathbf{s} = \frac{\partial u}{\partial t} + \mathbf{J} \cdot \mathbf{E} \,, \tag{2.15}$$

where u is the energy density, t is time, **S** is the Poynting vector, and **J** is the current density. When applied to the system model in the frequency domain, this becomes

$$-\nabla \cdot \mathbf{s} = \frac{i\omega}{4\pi\varepsilon_0} \left(\mathrm{Re}\left(\varepsilon\right) \mathbf{E} \cdot \mathbf{E}^* + \mathbf{H} \cdot \mathbf{H}^* \right) + \frac{\mathrm{Im}\left(\varepsilon\right) \omega}{4\pi} \mathbf{E} \cdot \mathbf{E}^* \,. \tag{2.16}$$

According to the physical interpretation of the Poynting vector, taking the real part of the left hand side of Eq. (2.16) and integrating over the volume gives the amount of electromagnetic energy absorbed by the particle[46]. Carrying out this operation and normalizing by the incident electromagnetic flux yields the absorption cross-section,

$$\sigma_a = \frac{k}{\varepsilon_0 |\mathbf{E}_i|^2} \int_V \mathrm{Im}\left(\varepsilon\left(\mathbf{r}\right)\right) |\mathbf{E}\left(\mathbf{r}\right)|^2 d^3 r\,. \tag{2.17}$$

Thus, the absorption cross-section is related to the energy that is absorbed by the scattering particle.

The extinction cross-section can be obtained from the optical theorem,

$$\sigma_e = \frac{4\pi}{k}\,\mathrm{Im}\left(f\right)\,, \tag{2.18}$$

where f is the normalized scattering amplitude in the forward direction, which for the model system is

$$f = \frac{1}{|\mathbf{E}_i|^2}\mathbf{F}\left(\theta = \mathbf{0}\right). \tag{2.19}$$

Applying Eq. (2.18) and (2.19) to the model system gives

$$\sigma_e = \frac{k}{|\mathbf{E}_i|^2} \int_V \mathrm{Im}\left(\left[\frac{\varepsilon\left(\mathbf{r}\right)}{\varepsilon_0} - 1\right] \mathbf{E}\left(\mathbf{r}\right) \cdot \mathbf{E}_i^*\left(\mathbf{r}\right)\right) d^3\mathbf{r}\,. \tag{2.20}$$

The derivation of the optical theorem gives a clear meaning to σ_e; it is a measure of the total energy scattered or absorbed by the particle[23].

Since, the extinction cross-section accounts for both scattering and absorption and the absorption cross-section accounts for absorption, the scattering cross-section is easily obtained by taking the difference in these quantities,

$$\sigma_s = \sigma_e - \sigma_a\,. \tag{2.21}$$

It is related to how much energy is scattered by the particle.

The Mueller matrix along with the cross-sections and the anisotropy factor are the collection of scattered field parameters that will be used to make comparisons between different scattering particles.

Chapter 3: Near field methods

The previous chapter has described the theoretical framework for the investigation of light scattering. To make use of this framework, numerical tools are used to simulate the system described in §2.1. The simulation will take the parameters used to describe the system and calculate the scattered field in the time domain. The first four sections of this chapter describe the various methods used in the simulation. The final section describes some of the numerical difficulties that arise through the use of these methods.

3.1 Finite-Difference Time Domain method

The basis of the FDTD method is the replacement of continuous operators in the Maxwell Equations by finite difference operators. This results in a set of six algebraic equations which relate field components at finite points in space to neighboring field components. Thus, a continuous wave propagating through space is simulated by a numerical wave propagating through the grid of points.

The Maxwell equations for the model system of §2.1 are

$$\begin{array}{ll} \nabla \cdot \mathbf{E} = 0 & \nabla \times \mathbf{E} = -\frac{1}{\mu}\frac{\partial}{\partial t}\mathbf{H} \\ \nabla \cdot \mathbf{H} = 0 & \nabla \times \mathbf{H} = \varepsilon\frac{\partial}{\partial t}\mathbf{E} \end{array} . \tag{3.1}$$

Working with complex numbers is computationally more expensive than working with real numbers, so an equivalent expression to Ampere's law without the use of the complex permittivity will save computational resources. To obtain such an expression, the method described by Yang and Liou is used[46]. This starts by casting Ampere's law to the source dependent form

$$\nabla \times \mathbf{H} = \frac{\varepsilon'}{c}\frac{\partial \mathbf{E}}{\partial t} + \frac{4\pi}{c}\sigma \mathbf{E}\,, \tag{3.2}$$

where ε' is the effective real permittivity and σ is the effective real conductivity. Assuming a harmonic time dependence and transforming both forms to the frequency domain gives

$$\begin{aligned} \nabla \times \mathbf{H} =& -ik\varepsilon\mathbf{E} \\ \nabla \times \mathbf{H} =& -ik\left(\varepsilon' + i\frac{4\pi}{kc}\sigma\right)\mathbf{E} \end{aligned}\,. \tag{3.3}$$

By comparison it is clear that the two expressions are equivalent if $\varepsilon = \varepsilon' + i\frac{4\pi}{kc}\sigma$. Letting $\varepsilon_r = \varepsilon'$, $\varepsilon_i = \frac{4\pi}{kc}\sigma$, and $\tau = kc\frac{\varepsilon_i}{\varepsilon_r}$, Eq. (3.2) becomes

$$\nabla \times \mathbf{H} = \frac{\varepsilon_r}{c}\left(\frac{\partial \mathbf{E}}{\partial t} + \tau\mathbf{E}\right)\,, \tag{3.4}$$

an expression using all real numbers.

To obtain the finite difference expressions, the operator $\frac{\partial}{\partial t}$ must be replaced with a finite difference operator. Again, methods previously reported are used[46]. First, Eq. (3.4) is written in the equivalent form

$$\frac{\partial\left\{e^{\tau t}\mathbf{E}\right\}}{\partial t} = e^{\tau t}\frac{c}{\varepsilon_r}\nabla \times \mathbf{H}\,, \tag{3.5}$$

Then, the finite difference operator for $\frac{\partial}{\partial t}$ in Eq. (3.4) is found by integrating over the time interval $[n\Delta_t, (n+1)\Delta_t]$ which yields

$$\begin{aligned} e^{\tau(n+1)\Delta_t}\mathbf{E}\big|_{n+1} - e^{\tau n\Delta_t}\mathbf{E}\big|_{n} =& \int_{n\Delta_t}^{(n+1)\Delta_t} e^{\tau t}\frac{c}{\varepsilon_r}\nabla \times \mathbf{H} dt \\ \approx& e^{\tau\left(n+\frac{1}{2}\right)\Delta_t}\frac{c\Delta_t}{\varepsilon_r}\nabla \times \mathbf{H}\big|_{n+\frac{1}{2}} \end{aligned}\,, \tag{3.6}$$

where the subscript denotes the time step at which the field is evaluated, i.e., $\mathbf{E}\big|_n = \mathbf{E}\left(t = n\Delta_t\right)$. Thus $\mathbf{E}\big|_{n+1}$ is described using only values known from previous times steps by

$$\mathbf{E}\big|_{n+1} \approx e^{-\tau n\Delta_t}\mathbf{E}\big|_n + e^{-\tau\frac{\Delta_t}{2}}\frac{c\Delta_t}{\varepsilon_r}\nabla\times\mathbf{H}\big|_{n+\frac{1}{2}}\,. \tag{3.7}$$

To obtain the finite difference operator corresponding to ∇, consider the operator $\frac{\partial}{\partial r_i}$ acting on a vector $\mathbf{A}$. This is approximated using a central difference as

$$\frac{\partial}{\partial r_i}\mathbf{A} \approx \frac{\mathbf{A}\big|_{n+1} - \mathbf{A}\big|_n}{\Delta_{r_i}}\,, \tag{3.8}$$

where $\Delta_{r_i} = r_i\big|_{n+1} - r_i\big|_n$. Using this central difference operator for the components of ∇ gives a new vector finite difference operator, which applied to Eq. (3.7) gives three algebraic equations. Assuming equal length intervals, Δ, for each operator, the equation corresponding to the x-component of the electric field is

$$\begin{aligned}\mathbf{E_x}\big|_{i,j,k,n} = e^{-\tau\Delta_t}\big|_{i,j,k}E_x\big|_{i,j,k,n-1} + \left(e^{-\tau\frac{\Delta_t}{2}}\frac{\Delta_t}{\varepsilon_r\Delta}\right)\Big|_{i,j,k} \\ \times\left(H_z\big|_{i,j+\frac{1}{2},k,n-\frac{1}{2}} - H_z\big|_{i,j-\frac{1}{2},k,n-\frac{1}{2}} - H_y\big|_{i,j,k+\frac{1}{2},n-\frac{1}{2}} + H_y\big|_{i,j,k-\frac{1}{2},n-\frac{1}{2}}\right)\end{aligned}\,, \tag{3.9}$$

where the subscripts i, j, and k indicate the position at which the field is evaluated, i.e., $\mathbf{H}\big|_{i,j,k,n} = \mathbf{H}\left(x = i\Delta, y = j\Delta, z = k\Delta, t = n\Delta_t\right)$.

Substituting the continuous operators ∇ and $\frac{\partial}{\partial t}$ with the finite difference operators for the curl equations of Eq. (3.1) results in the six algebraic equations

$$\begin{aligned}
\mathbf{E_x}\big|_{i,j,k,n} &= e^{-\tau\Delta_t}\big|_{i,j,k} E_x\big|_{i,j,k,n-1} + \left(e^{-\tau\frac{\Delta_t}{2}}\frac{\Delta_t}{\varepsilon_r\Delta}\right)\Big|_{i,j,k} \\
&\quad \times \left(H_z\big|_{i,j+\frac{1}{2},k,n-\frac{1}{2}} - H_z\big|_{i,j-\frac{1}{2},k,n-\frac{1}{2}} - H_y\big|_{i,j,k+\frac{1}{2},n-\frac{1}{2}} + H_y\big|_{i,j,k-\frac{1}{2},n-\frac{1}{2}}\right) \\
\mathbf{E_y}\big|_{i,j,k,n} &= e^{-\tau\Delta_t}\big|_{i,j,k} E_y\big|_{i,j,k,n-1} + \left(e^{-\tau\frac{\Delta_t}{2}}\frac{\Delta_t}{\varepsilon_r\Delta}\right)\Big|_{i,j,k} \\
&\quad \times \left(H_x\big|_{i,j,k+\frac{1}{2},n-\frac{1}{2}} - H_x\big|_{i,j,k-\frac{1}{2},n-\frac{1}{2}} - H_z\big|_{i+\frac{1}{2},j,k,n-\frac{1}{2}} + H_z\big|_{i-\frac{1}{2},j,k,n-\frac{1}{2}}\right) \\
\mathbf{E_z}\big|_{i,j,k,n} &= e^{-\tau\Delta_t}\big|_{i,j,k} E_z\big|_{i,j,k,n-1} + \left(e^{-\tau\frac{\Delta_t}{2}}\frac{\Delta_t}{\varepsilon_r\Delta}\right)\Big|_{i,j,k} \\
&\quad \times \left(H_y\big|_{i+\frac{1}{2},j,k,n-\frac{1}{2}} - H_y\big|_{i-\frac{1}{2},j,k,n-\frac{1}{2}} - H_x\big|_{i,j+\frac{1}{2},k,n-\frac{1}{2}} + H_x\big|_{i,j-\frac{1}{2},k,n-\frac{1}{2}}\right) \\
\mathbf{H_x}\big|_{i,j,k,n} &= e^{-\tau\Delta_t}\big|_{i,j,k} H_x\big|_{i,j,k,n-1} + \left(e^{-\tau\frac{\Delta_t}{2}}\frac{\Delta_t}{\varepsilon_r\Delta}\right)\Big|_{i,j,k} \\
&\quad \times \left(E_y\big|_{i,j,k+\frac{1}{2},n-\frac{1}{2}} - E_y\big|_{i,j,k-\frac{1}{2},n-\frac{1}{2}} - E_z\big|_{i,j+\frac{1}{2},k,n-\frac{1}{2}} + E_z\big|_{i,j-\frac{1}{2},k,n-\frac{1}{2}}\right) \\
\mathbf{H_y}\big|_{i,j,k,n} &= e^{-\tau\Delta_t}\big|_{i,j,k} H_y\big|_{i,j,k,n-1} + \left(e^{-\tau\frac{\Delta_t}{2}}\frac{\Delta_t}{\varepsilon_r\Delta}\right)\Big|_{i,j,k} \\
&\quad \times \left(E_z\big|_{i+\frac{1}{2},j,k,n-\frac{1}{2}} - E_z\big|_{i-\frac{1}{2},j,k,n-\frac{1}{2}} - E_x\big|_{i,j,k+\frac{1}{2},n-\frac{1}{2}} + E_x\big|_{i,j,k-\frac{1}{2},n-\frac{1}{2}}\right) \\
\mathbf{H_z}\big|_{i,j,k,n} &= e^{-\tau\Delta_t}\big|_{i,j,k} H_z\big|_{i,j,k,n-1} + \left(e^{-\tau\frac{\Delta_t}{2}}\frac{\Delta_t}{\varepsilon_r\Delta}\right)\Big|_{i,j,k} \\
&\quad \times \left(E_x\big|_{i,j+\frac{1}{2},k,n-\frac{1}{2}} - E_x\big|_{i,j-\frac{1}{2},k,n-\frac{1}{2}} - E_y\big|_{i+\frac{1}{2},j,k,n-\frac{1}{2}} + E_y\big|_{i-\frac{1}{2},j,k,n-\frac{1}{2}}\right)
\end{aligned} \quad . \tag{3.10}$$

Note, that the electric field components at some time step, $(n+1)\,\Delta_t$, depend on the values of the magnetic field components at one-half time step earlier, $\left(n-\frac{1}{2}\right)\Delta_t$, and *vice versa*. This choice of differencing operators allows all of the electric field components at time t to be calculated, followed by the calculation of all of the magnetic field components at time $t+\frac{1}{2}\Delta_t$, and so on. Along with the appropriate field component placement, discussed in the next paragraph, this avoids the need to solve simultaneous equations at each time step, which is computationally expensive.

The grid on which Eq. (3.10) are applied is composed of Yee cells[47]. As shown

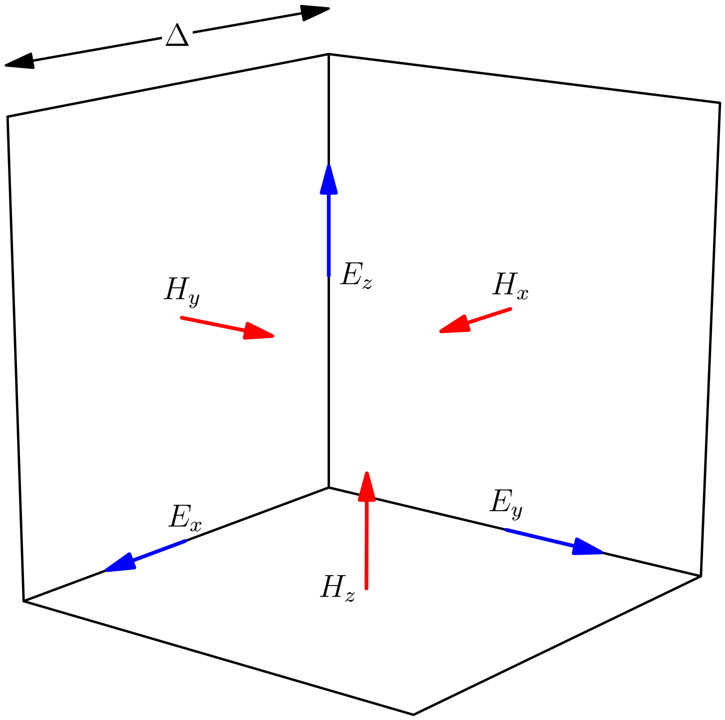

Figure 3: The grid cell used is known as the Yee cell[47]. Each electric field component is offset from two magnetic field comonents by one half the distance across the cell ($\Delta/2$), and *vice versa*. This configuration avoids the necessity of solving simultaneous equations at each time step.

in Fig. 3, each grid cell contains one of each of the field components. Each electric field component is offset from two magnetic field components by one half the cell dimension and *vice versa*. This grid arrangement implicitly enforces the divergence equations of Eq. (3.1)[40], and allows the calculations at each time step to be carried out without the need to solve a set of simultaneous equations.

Using finite difference operators and the Maxwell equations, the basic FDTD method has been derived. This allows the simulation of electromagnetic waves as numerical waves on a grid. Using the method described, the electric field updates are calculated followed by the magnetic field update, which is in turn followed by the next electric field update, and so on. This process is referred to as time marching. In the following sections, the problems of introducing the source field and terminating the grid will be addressed.

3.2 Incident field

The incident field is introduced into the grid using the total field/scattered field formulation (TF/SF). It is so named because using this formulation, the grid has two regions; one containing the total field, and one containing the scattered field only, as shown in Fig. 4. The superposition principle is the key to using the TF/SF formulation. By the superposition principle, the incident electric field can be calculated independently of the electric field time marching update, and the same applies to

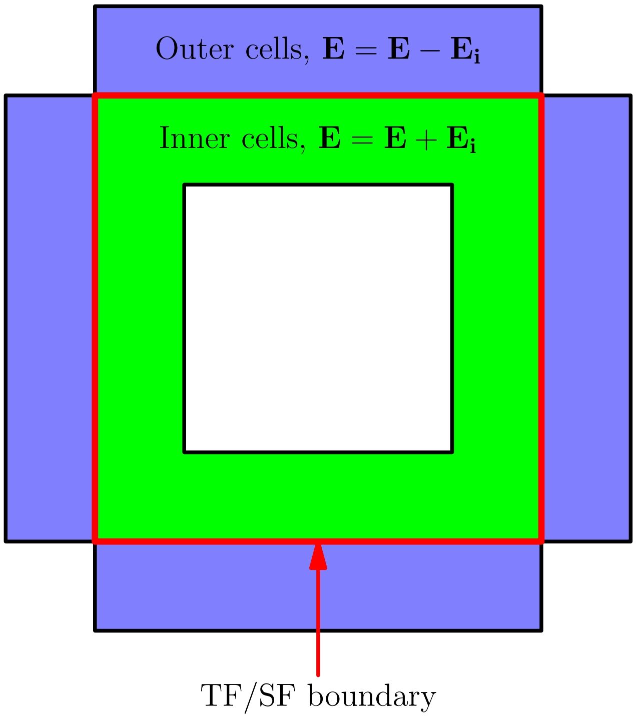

Figure 4: The total field/scattered field boundary divides the grid into the total field and scattered field regions. The incident field is introduced into the grid by adding to or subtracting from the field values at cells adjacent to the boundary in such a way that the total field propagates within the boundary and only the scattered field propagates without.

the magnetic field. The sequence of field updates including the incident fields is (1) update the electric field by time marching, (2) update the electric field using TF/SF calculations, (3) update the magnetic field, and (4) update the magnetic field using TF/SF calculations. This process is repeated until the simulation is complete.

To use the TF/SF method a boundary which surrounds the scattering particle is chosen such that it lies on the surfaces shared by adjacent grid cells, as shown in Fig. 4. At cells adjacent to this boundary, the known values of the incident field are either added to or subtracted from the field components. The incident field is added if the cell is within the boundary, and subtracted if it is not. This allows the normal time stepping operations to propagate the incident field into the region of the particle, while at the same time keeping the incident field confined to this region. Thus, two regions can be identified, the one containing the scattering particle is the total field region, and the other is the scattered field region.

Because the total field is being propagated numerically, numerical errors should be included when calculating the incident field. For this reason, the incident field values are also calculated numerically. This is accomplished by propagating the incident field through an auxiliary one-dimensional grid, using a method similar to that of §3.1, and projecting the field onto the three-dimensional grid at the TF/SF boundary. This method is depicted in Fig. 5, where $\mathbf{k_i}$ is the incident field direction, the cube is the TF/SF boundary, the plane is the wavefront, and the red point and lines show where the point is projected onto the boundary. This auxiliary grid method allows numerical errors to be duplicated as the incident field propagates, thereby reducing the overall error when adding the incident field values to the grid. Failure to duplicate the errors would result in an unintended "error" wave propagating through the FDTD grid due to the mismatch in values between the incident field in the auxiliary grid and the FDTD grid. Because the incident field is a plane wave, known values can be added

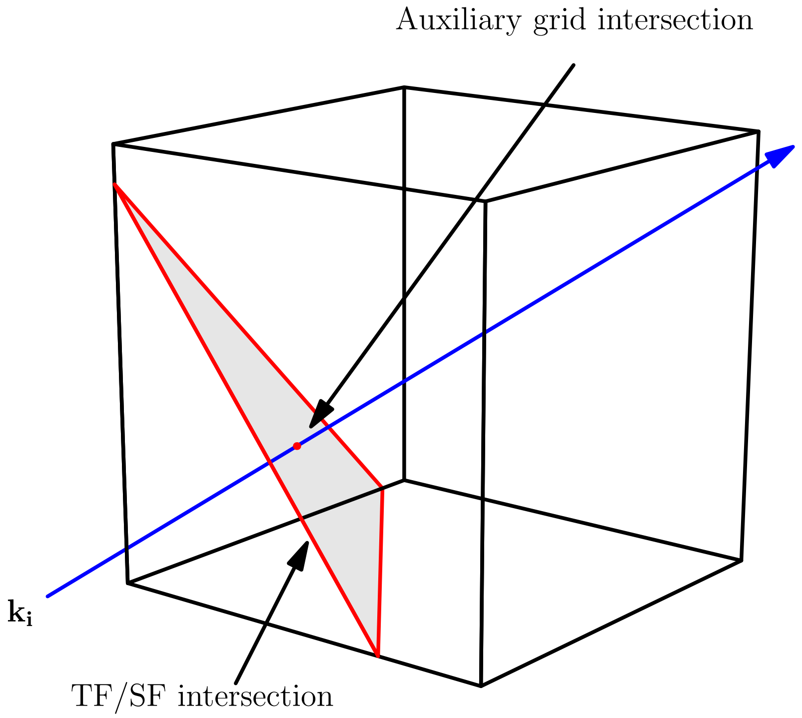

Figure 5: The incident field is calculated in an auxiliary grid and projected onto the TF/SF boundary. The incident field is a plane wave with wavenumber vector $\mathbf{k}_i$. The point at which the wavefront intersects the auxiliary grid and the points at which the wavefront intersects the TF/SF boundary all have the same field values.

to the cells at both ends of the auxiliary grid to stop the field propagation, just as the TF/SF boundary does in the FDTD grid.

Using the methods of §3.1 and this section, an electromagnetic wave can be introduced into a numerical grid which will simulate the interaction between the wave and the scattering particle.

3.3 Boundary condition

In order to simulate the open space system on a finite grid, a technique called the perfectly matching layer absorbing boundary condition, or PML, is used. The particular PML used in the simulation is called Berrenger's PML, named after its developer[40].

The technique involves introducing a new (unphysical) medium which surrounds the region of interest. This new medium is designed such that electromagnetic waves encountering the surface will be attenuated with minimal reflection. The new medium is in turn, surrounded by a perfect electrical conductor, which will reflect the attenuated waves back through the PML layer resulting in further attenuation before the wave propagates back into the region of interest. This reduces the magnitude of the wave by several orders of magnitude[40], making its contribution to the region of interest negligible. To use this method, the FDTD Maxwell equations must be generalized by separating each field component into two parts. For example, the E_x component is split into the E_x^y and E_x^z components according to whether the corresponding magnetic component differencing is in the x or y direction, respectively. This results in a set of twelve equations to be used in the PML. Eq. (3.11) shows the FDTD equation for E_x and the PML equations for E_x^y and E_x^z for comparison.

$$\begin{array}{l}
E_x\big|_{i,j,k,n} = e^{-\tau\Delta_t}\big|_{i,j,k} E_x\big|_{i,j,k,n-1} + \left(e^{-\tau\frac{\Delta_t}{2}}\dfrac{\Delta_t}{\varepsilon_r\Delta}\right)\big|_{i,j,k} \\
\quad \times \left(H_z\big|_{i,j+\frac{1}{2},k,n-\frac{1}{2}} - H_z\big|_{i,j-\frac{1}{2},k,n-\frac{1}{2}} - H_y\big|_{i,j,k+\frac{1}{2},n-\frac{1}{2}} + H_y\big|_{i,j,k-\frac{1}{2},n-\frac{1}{2}}\right) \\
E_x^y\big|_{i,j,k,n} = e^{-\tau^y\Delta_t}\big|_{i,j,k} E_x^y\big|_{i,j,k,n-1} + \left(e^{-\tau^y\frac{\Delta_t}{2}}\dfrac{\Delta_t}{\varepsilon_r^y\Delta}\right)\big|_{i,j,k} \\
\quad \times \left(H_z\big|_{i,j+\frac{1}{2},k,n-\frac{1}{2}} - H_z\big|_{i,j-\frac{1}{2},k,n-\frac{1}{2}}\right) \\
E_x^z\big|_{i,j,k,n} = e^{-\tau^z\Delta_t}\big|_{i,j,k} E_x^z\big|_{i,j,k,n-1} + \left(e^{-\tau^z\frac{\Delta_t}{2}}\dfrac{\Delta_t}{\varepsilon_r^z\Delta}\right)\big|_{i,j,k} \\
\quad \times \left(H_y\big|_{i,j,k-\frac{1}{2},n-\frac{1}{2}} - H_y\big|_{i,j,k+\frac{1}{2},n-\frac{1}{2}}\right)
\end{array} . \tag{3.11}$$

Notice that the permittivity, and the related τ, is not necessarily the same in all of the equations. Similarly, the permeability of the PML is not necessarily that of the host medium. This allows the contributions from finite differences over a direction tangent to the PML surface to be attenuated, while those normal to the surface are not, thereby reducing the reflection. Further, the permittivity and permeability for the new medium are chosen so that the impedance is matched between the new medium and the host medium, $\sqrt{\frac{\mu}{\varepsilon}} = \sqrt{\frac{\mu_0}{\varepsilon_0}}$, which means there will be no reflection for waves traveling in the direction normal to the surface of the PML[40]. Fig. 6 depicts the various types of PML regions used to terminate the grid. In the face regions, colored green, only the contributions from differences over a direction tangent to the face are attenuated. For example, in the face regions parallel to the yz-plane, $\varepsilon^x = \varepsilon_0$ and $\varepsilon^y, \varepsilon^z \neq \varepsilon_0$, which results in attenuation of both parts of E_x and one part in each of E_y and E_z. Where two face regions intersect, called the dihedral region and colored yellow, those contributions attenuated on either face are attenuated.

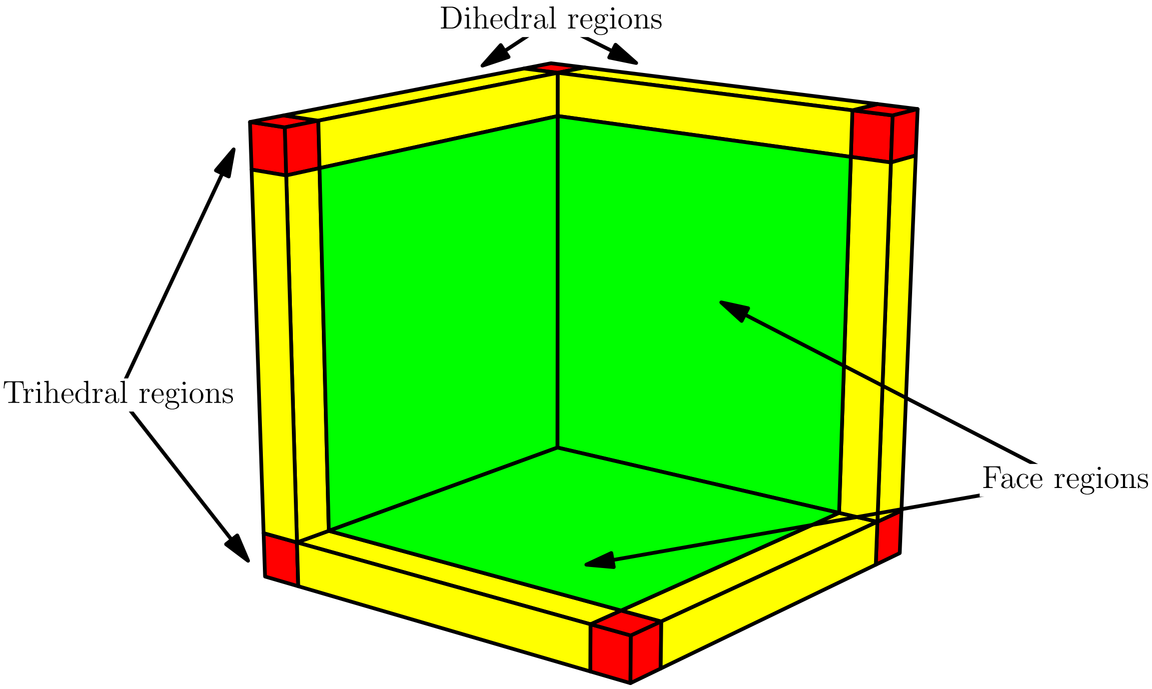

Figure 6: The PML is composed of three classes of attenuating regions. Each region has different optical properties to attenuate the fields in the region. In the face regions, two PML components are attenuated. In the dihedral regions, four components are attenuated. In the trihedral regions, all twelve PML components are attenuated. The PML method allows attenuation of the waves with minimal reflection by matching the impedence of the PML regions to that of the host medium.

Similarly, in the trihedral region, where three dihedral regions intersect and colored red, all contributions are attenuated. Note that in Eq. (3.10), the permeability is not present; however, using methods analogous to those of §3.1, the appropriate equations can be derived with $\mu \neq \mu_0$, which can be used to determine the PML equations for the magnetic field components.

Through the use of the PML, outgoing waves can be attenuated twice (once after reflection) resulting in a negligible error wave propagating through the region of interest. Thus, the physical open space model can be simulated numerically using a grid of finite size. Combining this with the methods previously discussed, allows the complete simulation of an incident electromagnetic field interacting with a scattering particle in a homogeneous region of open space. During the simulation, the values of the field components located within the scattering particle are calculated at each time step. However, these field values are time domain values, and the needed values for Eq. (2.6) are frequency domain values. The next section discusses the transformation to the frequency domain.

3.4 The discrete Fourier transform

Using the procedures described so far, the near field in the time domain can be determined over a discrete set of time steps; however, in order to calculate the desired scattered field properties, the near field in the frequency domain is needed. This is obtained by carrying out a discrete Fourier transform on all electric field components located within the scattering particle according to

$$\mathbf{E}\left(\mathbf{r},\omega\right) \approx \sum_{n} \mathbf{E}\left(\mathbf{r},t_n\right) e^{i\omega n \Delta_t} \,. \tag{3.12}$$

According to Eq. (3.12), at each step of time marching a term for each component is added, which results in the desired near field at the end of time marching. The transform is also carried out on the incident wave at the center of the grid. At the end of time marching, the total field is normalized by the incident field,

$$\mathbf{E} = \frac{\mathbf{E}'}{|\mathbf{E_i}|} \, . \tag{3.13}$$

where $\mathbf{E}'$ denotes the field in the frequency domain. This allows for comparisons which are independent of the magnitude of the incident field. All further references to $\mathbf{E}$ refer to the normalized total field.

3.5 Numerical dispersion

The use of Eq. (3.10) causes the numerical wave to have certain numerical artifacts as it propagates through the numerical space. Collectively, these effects are called numerical dispersion. Numerical dispersion results in a phase velocity dependence on wavelength, direction of propagation, and grid discretization. The dispersion relation can be derived starting from a compact form of the Maxwell curl equations[40],

$$\nabla \times (\mathbf{H} + i\mathbf{E}) = \frac{\partial}{\partial t} (\mathbf{H} + i\mathbf{E}) \ . \tag{3.14}$$

Applying Eq. (3.14) to a monochromatic numerical plane wave,

$$(\mathbf{H}_0 + i\mathbf{E}_0) \, e^{i(k_x i\Delta + k_y j\Delta + k_z k\Delta - \omega t)} \, , \tag{3.15}$$

results in a set of three equations with three unknowns. Setting the determinant of the system to zero results in

$$\left(\frac{\Delta}{c\Delta_t}\right)^2 \sin^2\left(\frac{1}{2}\omega\Delta_t\right) = \sin^2\left(\frac{1}{2}k_x\Delta\right) + \sin^2\left(\frac{1}{2}k_y\Delta\right) + \sin^2\left(\frac{1}{2}k_z\Delta\right) , \qquad (3.16)$$

which is the dispersion relation. From Eq. (3.16), it is seen that $\omega = kc$ only in the limit as Δ goes to 0. Also, the velocity dependence on k_x, k_y, and k_z indicates that the grid, i.e., numerical space, is anisotropic.

One consequence of the numerical dispersion is that waves propagating in the one-dimensional source grid, where $k_y, k_z = 0$, and the three-dimensional FDTD grid, where generally $k_x \neq k_y \neq k_z$, will have different velocities (except in the special cases where the incident field travels parallel to a grid axis). This will cause an error in introducing the source field to the grid due to the differing dispersion factors. However, this error can be eliminated by deliberately changing the velocity of the wave in the source grid. To do this, the wavenumbers for both grids are obtained using Eq. (3.16) and the appropriate ratio of the wavenumbers is used to scale the speed in the one-dimensional grid. This results in a wave traveling through the one-dimensional grid at a velocity equal to that of the wave in the three-dimensional grid, thereby aligning the wavefronts and eliminating errors due to differing velocities in the projection operation described in §3.2.

Using the methods described in this chapter, the total electric field in the frequency domain is obtained. This allows the calculation of **F** from Eq. (2.6). With this information, all of the desired scattered field properties described in §2.3 can be obtained. The next chapter describes how to calculate these values numerically.

Chapter 4: Obtaining the scattered field properties

Using the result of the simulation described in the previous chapter, the various scattering properties described in §2.3 can be calculated. This chapter describes how the equations given in that section are treated numerically. The first section describes the calculation of the matrix properties, while the second describes the calculation of the scalar properties.

4.1 Scattering and Mueller matrices

With the total field in the frequency domain calculated, see §3, the scattering properties can be obtained. Since this is done numerically, the angular resolved quantities, **S** and **M**, must be divided into discrete parts. A set of angles, azimuthal and polar with respect to the scattering direction, is chosen with the desired resolution to quantify these properties. This results in a discrete set of scattering wavenumber vectors, $\mathbf{k}_{sm}$, where m denotes the m^{th} vector of the set.

To calculate the scattering matrix, recall that Eq. (2.10) requires **F** to be calculated for two incident field polarizations. With the chosen set of scattering vectors and using Eq. (2.10) and Eq. (2.4), the elements of S are calculated by replacing the integral operation with a sum over the discrete volume elements. This yields

$$\begin{aligned}
S_2\left(\mathbf{k}_{sm}\right) &= i\Delta^3 \frac{k^3}{4\pi} \\
&\times \sum_n \left(1-\varepsilon\left(\mathbf{r}_n\right)\right) \left(\hat{\mathbf{e}}_\beta \cdot \hat{\mathbf{e}}_x \, \alpha \cdot \mathbf{E}\left(\mathbf{r}_n\right)\Big|_{\mathbf{E}_i=\hat{\mathbf{e}}_y} - \hat{\mathbf{e}}_\beta \cdot \hat{\mathbf{e}}_y \, \alpha \cdot \mathbf{E}\left(\mathbf{r}_n\right)\Big|_{\mathbf{E}_i=\hat{\mathbf{e}}_x}\right) e^{-i\mathbf{k}_{sm}\cdot\mathbf{r}_n} \\
S_3\left(\mathbf{k}_{sm}\right) &= i\Delta^3 \frac{k^3}{4\pi} \\
&\times \sum_n \left(1-\varepsilon\left(\mathbf{r}_n\right)\right) \left(\hat{\mathbf{e}}_\beta \cdot \hat{\mathbf{e}}_y \, \alpha \cdot \mathbf{E}\left(\mathbf{r}_n\right)\Big|_{\mathbf{E}_i=\hat{\mathbf{e}}_y} + \hat{\mathbf{e}}_\beta \cdot \hat{\mathbf{e}}_x \, \alpha \cdot \mathbf{E}\left(\mathbf{r}_n\right)\Big|_{\mathbf{E}_i=\hat{\mathbf{e}}_x}\right) e^{-i\mathbf{k}_{sm}\cdot\mathbf{r}_n} \\
S_4\left(\mathbf{k}_{sm}\right) &= i\Delta^3 \frac{k^3}{4\pi} \\
&\times \sum_n \left(1-\varepsilon\left(\mathbf{r}_n\right)\right) \left(\hat{\mathbf{e}}_\beta \cdot \hat{\mathbf{e}}_x \, \beta \cdot \mathbf{E}\left(\mathbf{r}_n\right)\Big|_{\mathbf{E}_i=\hat{\mathbf{e}}_y} - \hat{\mathbf{e}}_\beta \cdot \hat{\mathbf{e}}_y \, \alpha \cdot \mathbf{E}\left(\mathbf{r}_n\right)\Big|_{\mathbf{E}_i=\hat{\mathbf{e}}_x}\right) e^{-i\mathbf{k}_{sm}\cdot\mathbf{r}_n} \\
S_1\left(\mathbf{k}_{sm}\right) &= i\Delta^3 \frac{k^3}{4\pi} \\
&\times \sum_n \left(1-\varepsilon\left(\mathbf{r}_n\right)\right) \left(\hat{\mathbf{e}}_\beta \cdot \hat{\mathbf{e}}_y \, \beta \cdot \mathbf{E}\left(\mathbf{r}_n\right)\Big|_{\mathbf{E}_i=\hat{\mathbf{e}}_y} + \hat{\mathbf{e}}_\beta \cdot \hat{\mathbf{e}}_x \, \alpha \cdot \mathbf{E}\left(\mathbf{r}_n\right)\Big|_{\mathbf{E}_i=\hat{\mathbf{e}}_x}\right) e^{-i\mathbf{k}_{sm}\cdot\mathbf{r}_n}
\end{aligned} , \tag{4.1}$$

where $\mathbf{r}_n$ denotes $\mathbf{r}$ at the center of the n^{th} cell. Once $\mathbf{S}$ is obtained, $\mathbf{M}$ is calculated taking the sum of the appropriate components of $\mathbf{S}$ according to Eq. (2.13). The final result is a discrete set of numbers corresponding to the elements of $\mathbf{M}$ for the chosen set of vectors $\mathbf{k}_{sm}$.

4.2 Cross sections and anisotropy factor

The anisotropy factor, g, is calculated by replacing the integral over the solid angle with a sum over the scattering vectors, $\mathbf{k}_{sm}$. Applying this replacement to Eq. (2.14) results in

$$g = \frac{\sum_m S_{11}\left(\mathbf{k}_{sm}\right) \mathbf{k}_{sm} \cdot \mathbf{k}_i}{\sum_m S_{11}\left(\mathbf{k}_{sm}\right)} , \tag{4.2}$$

where $\mathbf{k}_{sm} \cdot \mathbf{k}_i$ is the cosine of the polar angle.

Like $\mathbf{S}$ and g, the absorption and extinction cross sections from Eq. 2.17 and 2.20 are approximated by replacing the integral operation with a sum. For the absorption cross section, the result comparable to Eq. (2.17) is

$$\sigma_a = k\Delta^3 \sum_n \mathrm{Im}\left(\varepsilon\left(\mathbf{r}_n\right)\right)\left|E\left(\mathbf{r}_n\right)\right|^2 . \tag{4.3}$$

Recall that the extinction cross section as derived from the optical extinction theorem requires that only the scattering amplitude in the forward direction, $\mathbf{k}_{s0}$, be known. The calculation analogous to Eq. (2.20) is

$$\sigma_e = k\,\mathrm{Im}\left(\sum_n \left(1-\varepsilon\left(\mathbf{r}_n\right)\right)\hat{\mathbf{e}}_p \cdot \mathbf{E}\left(\mathbf{r}_n\right)\Big|_{\mathbf{E}_i=\hat{\mathbf{e}}_p} e^{-i\mathbf{k}_{s0}\cdot\mathbf{r}_n}\right) , \tag{4.4}$$

where the subscript p denotes the polarization. The use of $\hat{\mathbf{e}}_p$ is allowed by the electric field having been normalized to the incident field, see Eq. (3.13). The scattering cross section is calculated by taking the difference of the previously calculated cross sections according to Eq. (2.21). Note that in general, the cross sections vary with the polarization vector. When making comparisons of a particular cross section, the average of the values for each polarization is used.

With the scattering properties calculated, comparisons between various scattering systems can be compared. The Mueller matrix gives an angular resolved quantity for comparison, while the cross sections and g allow comparison of scalar values.

Chapter 5: Parallel methods

Because the FDTD method models three-dimensional objects on a grid of points, the number of spatial operations required grows with volume, and the number of temporal operations grows with the distance that the incident field must travel. Thus, the simulation time to obtain the near field is at least $O(n^3)$. The memory requirements also depend on volume and are thus $O(n^3)$. For large scattering particles, this makes it impractical or impossible to carry out simulations on single workstations. For this reason, the program uses parallel methods, which allows simulations to be carried out on a network of computers or multiple processor systems. Regardless of the computing platform, a single processor and its associated memory will be referred to as a processing element, or PE.

Many computing platforms are designed to handle calculations on values stored contiguously in memory more efficiently than if they are stored non-contiguously. In order to take advantage of these platforms, the field values are allocated in a continuous section of memory. This allows optimizations such as vectorizing algorithms to be carried out by the compiler in order to produce efficient machine code. The potential for such optimizations combined with the parallel methods, discussed in the following sections, allows the program to run efficiently on a wide range of hardware, from a single pc to a network of multi-processor supercomputers. However, to run on a variety of platforms, the code must be written in a form that is portable. The code is written in standard Fortran 90, with communications carried out by the Message Passing Interface library (MPI). A Fortran 90 compiler and the MPI library are available for most platforms.

Parallelizing the program can be divided into three stages. The first stage is to parallelize the computation of the derivative parameters. This is accomplished by communicating the initial parameters such as $\mathbf{k}_i$, λ, ε, etc., to all of the PEs, allowing each PE to calculate any derivative parameters, e.g., ω, without the need for further communications. Although this results in duplicate calculations on separate PEs, the time taken is less than that used when calculating all derivative parameters on a single PE and then communicating them. The other stages are parallelizing the near field calculation, discussed in the next section, and parallelizing the calculation of the scattered field properties, discussed in the final section.

5.1 Near field

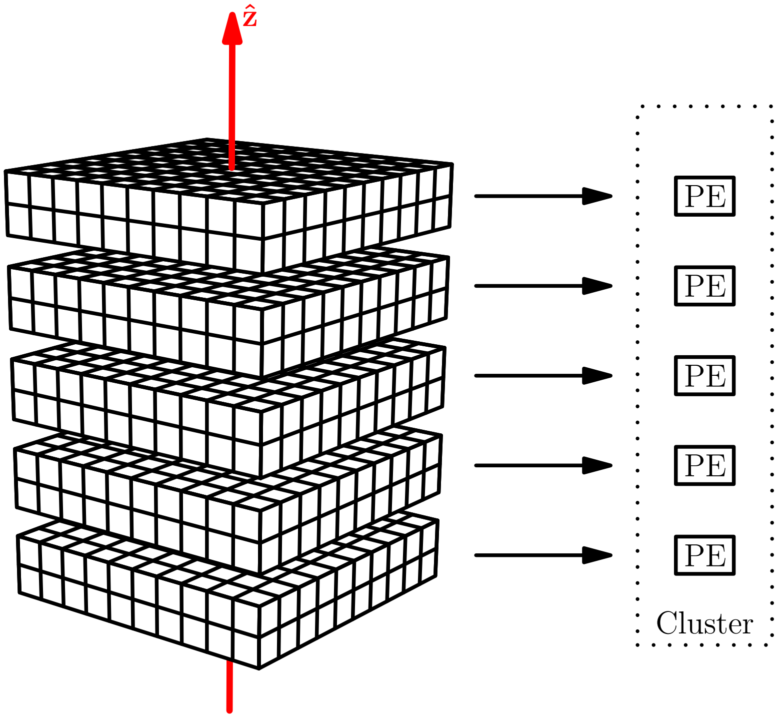

Figure 7: The FDTD grid is divided into sections along planes perpendicular to the z-axis. Each processing element in the cluster is assigned one of these sections. This allows simulataneous computations of the field values for a single timestep.

The FDTD method of §3.1 is parallelized in a straightforward manner using a simplified version of the method described by Taflove[40]. The computational space

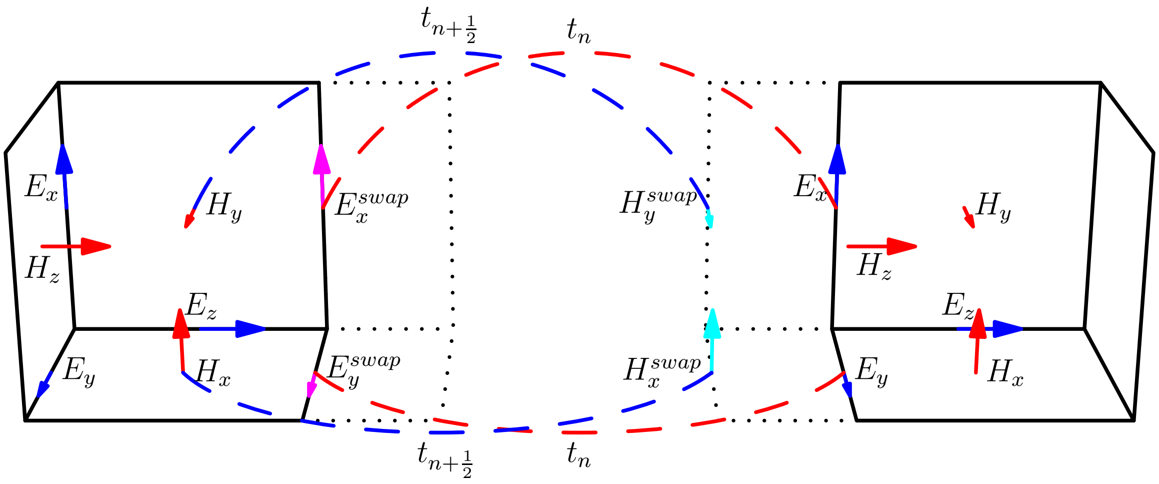

Figure 8: Parallel configuration of the time domain calculation for a cell.

is divided along planes that are normal to the z-axis, as shown in Fig. 7. Each PE can then calculate the field updates for a particular section of the grid. This division leads to the additional burden of communicating boundary values at the edge of the grid sections. For example, to calculate the x-component of the electric field at a boundary normal to the z-axis, the y-component of the magnetic field calculated by a neighboring PE is required. Conversely, the neighboring PE needs the x-component of the electric field in order to calculate the y-component of the magnetic field. This situation is illustrated in Fig. 8. Recall that the electric field updates and magnetic field updates are separated in time. This allows the values to be exchanged as needed; however, the space for the communicated values must be available in each of the PEs in order to carry out the exchange. To do this, an extra layer of cells is added to each z-normal face of a grid subsection. Because the grid is divided along a plane normal to the z-axis, only four field values need to be communicated, specifically $\mathbf{E}_x$, $\mathbf{E}_y$, $\mathbf{H}_x$, and $\mathbf{H}_y$. Since only the electric field is needed during the magnetic field update and *vice versa*, the communication of two field values takes place at intervals of one-half time step apart. The exchange illustrated in Fig. 8 depicts the grid division, the communicated values, and the times at which the communications occur.

Because all PEs have a copy of the simulation parameters, the calculation of the incident field can be done independently for each PE. As with the parameter communication, this is more efficient than first calculating the incident field on one PE and then communicating it. This also allows each PE to calculate the Fourier transform of the incident field, see §3.4. The Fourier transform and normalization of the total field is carried out by each PE only for the grid subsection on which that PE operates. Thus, at the end of time marching, the total field in the frequency domain remains distrubuted over the PEs in the same manner as the field in the time domain.

Although the using multiple PEs will reduce the overall time of the simulation and reduce the memory required for each PE, there is a limit on how many PEs can be efficiently used. This arises from the fact that the communication of boundary values requires time. Typically, communicating a value takes more time than calculating a value. So, as the number of PEs increases; the ratio of communication time to computation time also increases, thereby reducing the efficiency of the simulation. For example, assume adding PEs does not change the cpu time for computations (t), i.e., the sum of the times for all PEs, or the total communication time (T), i.e., simultaneous communication takes place. Then, the clock time (c) for a simulation is $c = t/n + T$, where n is the number of PEs. Thus, the clock time asymptotically approaches T with the number of PEs used. Thus, there is a point at which using additional PEs no longer significantly reduces the clock time. Another consideration in parallel simulations is load balancing, i.e., the distribution of operations across the PEs. Suppose the grid is divided so that one PE has to perform more operations than its neighbor, then the neighboring PE will have an idle period at each one-half time step while it is waiting for the boundary values needed to begin the next step. The FDTD program uses a load balancing method which divides the planes of grid cells evenly along the z-axis; however, this does not divide the operations required evenly since the PML and the Fourier transform calculations are not evenly distributed. Generally, this results in less efficient load balancing as the number of PEs increases.

5.2 Scattered field

Unlike the FDTD method, parallelizing the calculation of the scattered field properties requires only an initial communication followed by a few communications for some of the desired properties. The initial communication occurs at the end of the time marching process. This communication redistributes the near field values in the frequency domain evenly among all of the PEs. The other communications will be discussed in conjunction with their associated scattered field properties below.

The scattering amplitude matrix, $\mathbf{S}$, is calculated in parallel by assigning each PE to compute a portion of the sum in Eq. (4.1). Following this calculation, the results of the partial sums are then communicated to a single process which takes the sum of the communicated values. An equivalent form of Eq. (4.1) better represents this process. For example,

$$\begin{aligned} S_2\left(\mathbf{k}_{sm}\right) = i\Delta^3\frac{k^3}{4\pi} &\times \sum_m \sum_n \left(1-\varepsilon\left(\mathbf{r}_{m,n}\right)\right) \\ &\times \left(\hat{\mathbf{e}}_\beta\cdot\hat{\mathbf{e}}_x\,\alpha\cdot\mathbf{E}\left(\mathbf{r}_{m,n}\right)\Big|_{\mathbf{E}_i=\hat{\mathbf{e}}_y} - \hat{\mathbf{e}}_\beta\cdot\hat{\mathbf{e}}_y\,\alpha\cdot\mathbf{E}\left(\mathbf{r}_{m,n}\right)\Big|_{\mathbf{E}_i=\hat{\mathbf{e}}_x}\right) e^{-i\mathbf{k}_{sm}\cdot\mathbf{r}_{m,n}} \end{aligned}, \quad (5.1)$$

where m and n denote the n^{th} element of the m^{th} partial volume, is used to calculate S_2. Since the absorption and extinction cross sections each involve a similar volume integral, the calculation of these cross sections are carried out in a comparable manner.

These are better represented by equivalent forms of Eq. (4.3) and (4.4).

$$\begin{aligned} \sigma_a =& k\Delta^3 \sum_m \sum_n \operatorname{Im}\left(\varepsilon\left(\mathbf{r}_{m,n}\right)\right) \left|E\left(\mathbf{r}_{m,n}\right)\right|^2 \\ \sigma_e =& k \operatorname{Im}\left(\sum_m \sum_n \left(1-\varepsilon\left(\mathbf{r}_{m,n}\right)\right) \hat{\mathbf{e}}_p \cdot \mathbf{E}\left(\mathbf{r}_{m,n}\right)\big|_{\mathbf{E}_i=\hat{\mathbf{e}}_p} e^{-i\mathbf{k}_{s0}\cdot\mathbf{r}_{m,n}} \right) \end{aligned}, \tag{5.2}$$

where again m and n denote the n^{th} element of the m^{th} partial volume.

Since the calculations associated with $\mathbf{M}$, g, and σ_s, involve only algebraic operations over a small number of values, these are carried out by a single PE following the parallel computations.

Chapter 6: Cell model construction

To use the program developed, models containing information about the index of refraction of the scattering particle must be input into the program. To create the models, the assumption is made that there is a finite number of refractive index values which can be used to approximate the range of values found in the actual cells. For example, a cell model may have two refractive index values; one corresponding to the cytoplasm, and the other to the nucleus. Of course the model does not have to be limited to two values, so complex models containing many values may be created. The first section of this chapter describes the general method by which the models are created. The second section describes how the general method can be applied using analytic functions. The third section describes how more complicated models, that may not be described analytically, can be created from raster data. The final section describes how visualization and volume calculations can be carried on the models obtained.

6.1 General method

According to Eq. (3.10), the permittivity must be known at the location of the field components in the grid; so the model must contain at least this information. The Yee cell, Fig. 3, can be divided into eight subcells as shown in Fig. 9. These subcells will be referred to as model cells. Fig. 9 shows that each field component is at the corner of eight model cells. Thus, if the permittivity is known at all corners of all model cells, then the permittivity is known at all field component locations. The general method for constructing a model is to create a function that given a location will return the permittivity. This function will be called the model function. Using the model

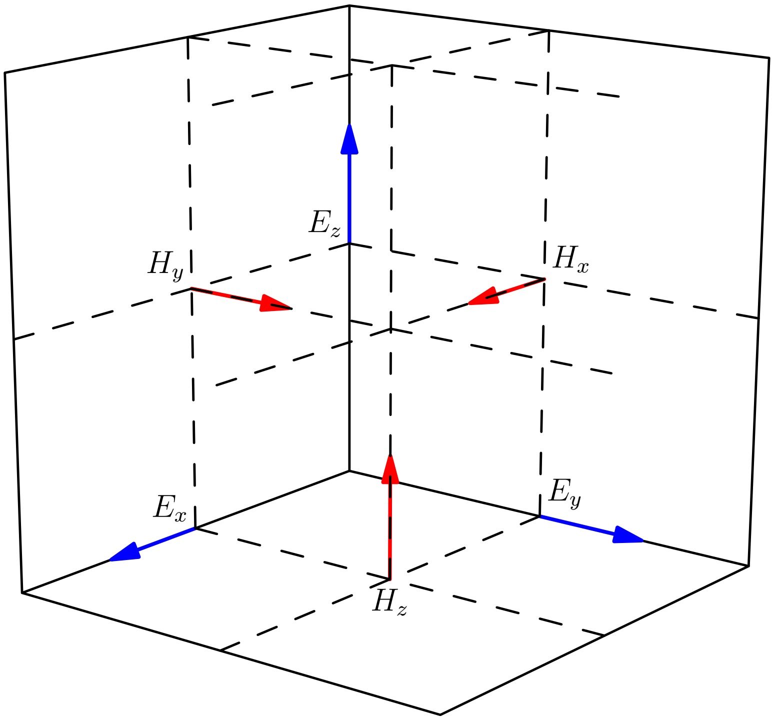

Figure 9: For model construction the Yee cell is divided into eight subcells called model cells. Each field component is located at the corner of eight model cells. By obtaining the domains in which the corners of the model cells are located; the domains in which the field components are located are also obtained. Knowing the domains of the model cells' corners allows visualization via the marching tetrahedron algorithm.

function, the permittivity is obtained for the corners of all model cells. This method allows the model generation program to be reused for various models with only the requirement that a new type of model requires a new model function. Obtaining information at the corners of all model cells, instead of just the field component locations, allows visualization of the model using the marching squares or marching tetrahedron algorithms.

6.2 From analytic functions

For analytic functions, the model function is simply a test against the implicit form of the analytic function. For example, a homogeneous sphere of radius R has the implicit function

$$x^2 + y^2 + z^2 - R^2 = 0,$$

and the model function is

$$f\left(x, y, z\right) = \left\{ \begin{array}{ll} \varepsilon & \text{, if } x^2 + y^2 + z^2 - R^2 \leq 0 \\ \varepsilon_0 & \text{, otherwise} \end{array} \right\}.$$

Thus the model function returns ε if point (x, y, z) is within or on the sphere and ε_0 otherwise. The homogeneous sphere is a simple example; however, more complex shapes follow exactly the same principle as long as they can be expressed analytically with an implicit function.

6.3 From domain images

For shapes which cannot be described analytically, a “z-stack” of domain data may be used. The z-stack of domain data is a set of images which are parallel to each other and perpendicular to the z-axis. The data consists of pixels having colors, which represent the domains. For example, Fig. 10 is an image containing data for three domains; one represented by black, another by green, and a third by yellow. In order to construct the model function, the height and width of the pixels, and the distance between images must also be known. In addition, the set relationship between the domain data must be known, e.g., in Fig. 10 the yellow is a subset of the green and the green is a subset of the black. It is assumed that a single domain is found along the edges of each image, and this domain is referred to as the background domain. With this information, a model function can be constructed.

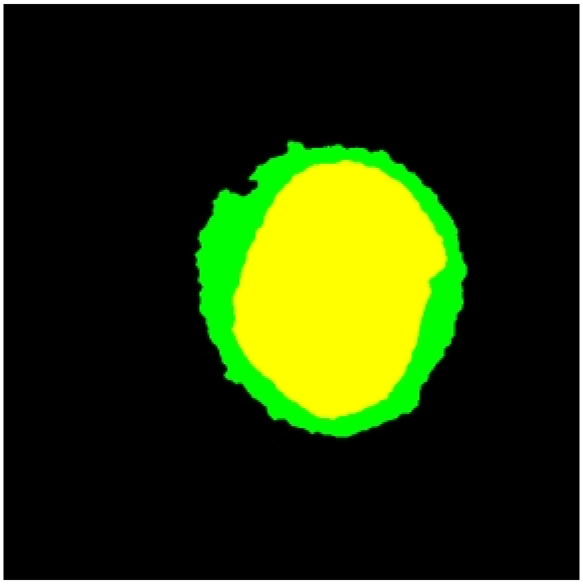

Figure 10: A typical domain images. Three domains are represented by black, green, and yellow. The black domain is the background domain.

To construct the model function, the non-background domains are considered individually. To process a domain the boundary pixels of the domains in each image are defined. This is done by removing the interior pixels of each image leaving only a series of pixels which have exactly two neighboring pixels, as shown in Fig. 11.

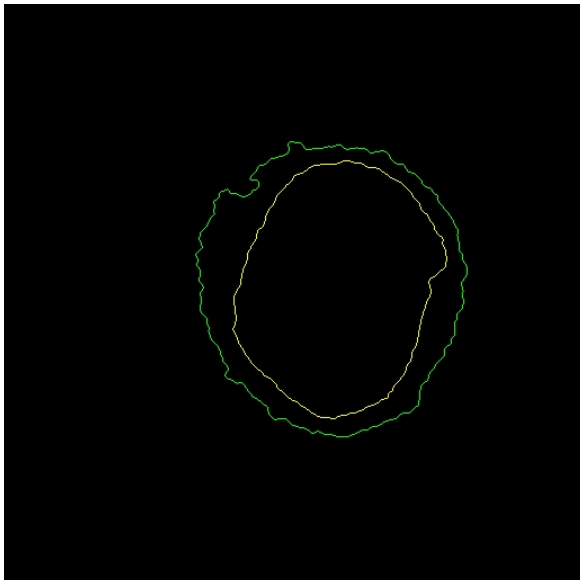

Figure 11: The boundary pixels for the yellow and green domains of Fig. 10. The contour of the background domain is the image boundary, but it is not needed for the model construction process.

Recall that the model function takes a locations, call it (x, y, z), as an argument. The z-coordinate may or may not lie on one of the image planes, so define $\{z_i\}$ as the ordered set of z-coordinates of the image planes such that $z_{i+1} > z_i$. Now define a set of piecewise linear contour functions, $\left\{C^j_{z_i}\right\}$ for each of the domains,

$$C^j_{k,z_i}(t) = (x_k, y_k) + \frac{(x_{k+1}, y_{k+1}) - (x_k, y_k)}{|(x_{k+1}, y_{k+1}) - (x_k, y_k)|} t, 0 \leq t \leq 1, 1 \leq k \leq n, \tag{6.1}$$

where C^j_{k,z_i} is the k^{th} segment of the contour associated with the j^{th} domain in the image at z_i and n is the number of boundary pixels for the same domain and image. Note that the contours are closed, so for k_{max}, $k_max + 1 = 1$ to complete the cycle.

Using Eq. (6.1) a distance function is defined,

$$d\left(x,y,z_i\right)=\begin{cases}-\inf\left\{\min\left(\left|\left(x,y\right)-C^j_{k,z_i}\left(t\right)\right|\right),1\leq k\leq n\right\} & \text{if } \left(x,y\right)\in\text{domain,}\\ \inf\left\{\min\left(\left|\left(x,y\right)-C^j_{k,z_i}\left(t\right)\right|\right),1\leq k\leq n\right\} & \text{otherwise}\end{cases}\tag{6.2}$$

where there are n boundary pixels for the j^{th} domain in the image at z_i. Thus d is equal in magnitude to the shortest distance to a contour and the sign of d indicates whether the point is within the domain. Further, define z_m and z_n such that

$$\begin{array}{c}z_m=\inf\left(\left\{z_i|z-z_i>0\right\}\right)\\ z_n=\inf\left(\left\{z_i|z_i-z>0\right\}\right)\end{array},\tag{6.3}$$

i.e., the z-coordinates of the two slides closest to z. Using Eq. (6.2) and 6.3 the model function, f is defined,

$$\begin{array}{c}f\left(x,y,z\right)=\text{Inner}\left(\left\{\varepsilon|\varepsilon=g^i\left(x,y,z\right),i=1,2,\ldots,l\right\}\right)\\ g^i\left(x,y,z\right)=\left\{\begin{array}{ll}\varepsilon^i & \text{, if } d\left(x,y,z_m\right)+\left(z-z_m\right)\frac{d(x,y,z_n)-d(x,y,z_m)}{z_n-z_m}\leq 0\\ \varepsilon_0 & \text{, otherwise}\end{array}\right\},\end{array}\tag{6.4}$$

where there are l domains, and Inner returns the element whose corresponding domain is not a superset of any other element's corresponding domain.

6.4 Visualization and volume calculation

Once the model is constructed, there is a domain value associated with each corner of the model cells. Using these values, a surface can be created for visualization and volume calculation purposes; for example, Fig. 12 depicts such a surface. Surfaces are

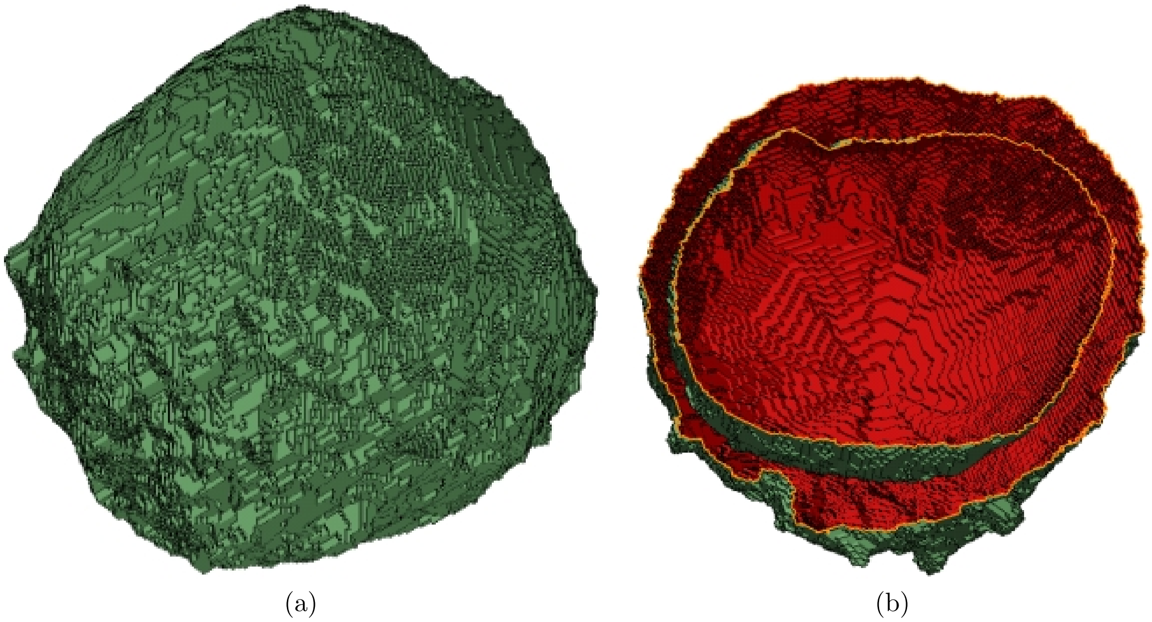

(a) (b)

Figure 12: (a)The three dimensional model of cell8, and (b)a cut away of the same model showing part of the nucleus model.

created using a "marching tetrahedra" algorithm. To use the marching tetrahedra algorithm, each model cell is divided into six tetrahedra, and the corners of the cells are ordered, as shown in Fig. 13. To create a surface, the domains are treated individually. Using the precedence rule described in the previous section, any subdomain of the domain of interest is considered part of the domain of interest. The surface facets, which are triangular, are created by adding a facet vertex at the midpoint between any two tetrahedron vertices which have one vertex within the domain and the other without. Since there are four vertices per tetrahedron and two possible states, i.e., within or without, there are $2^4 = 16$ possible surfaces. For example the sixteen possible surfaces for the light blue tetrahedron of Fig. 13 are shown in Fig. 14. In the figure, the outward facing facet surfaces are red and the inward facing surfaces are blue. To simplify processing of the surfaces, the model cells, rather than the individual tetrahedra, are treated as a unit. Since there are 8 vertices for each model cell,

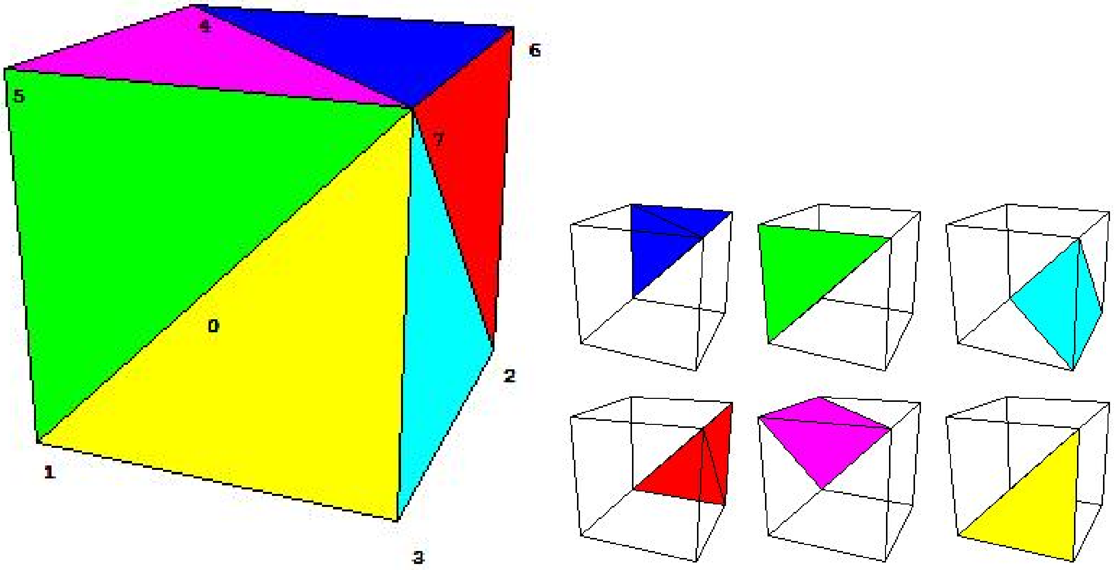

(a) (b)

Figure 13: (a)A model cell is divided into six tetrahedra. (b)The six tetrahedra shown individually. Model cells are divided this way for use in a marching tetrahedra algorithm.

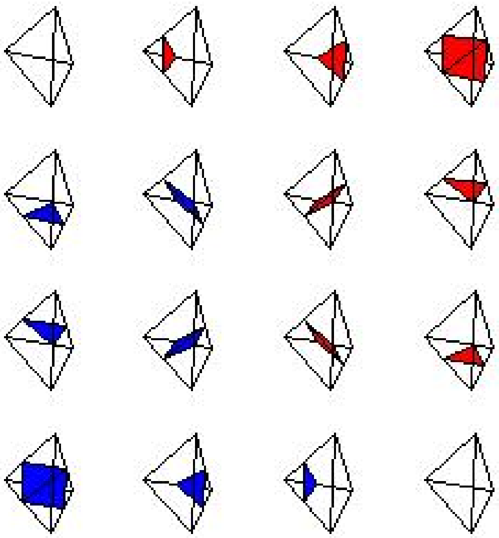

Figure 14: There are sixteen possible combinations of facets that can be associated with a tetrahedron according to which of the vertices are within the domain. Outward facing surfaces are marked red and inward facing surfaces, blue.

there are $2^8 = 256$ possible groups of facets for any given cell. For each possibility, the entire group of facets associated with the six tetrahedra of the cell are associated with a unique integer ranging from 0 to 255. This is the reason for ordering the corners of the model cells. By associating each corner with a binary bit, the integer id is determined. For example a cell having corners 0, 3, and 7 within the domain and the others without would have an id of $10001001_2 = 137_{10}$, where the subscript denotes the base of the numbering system. To further simplify the processing, any group of adjacent coplanar facets are replaced, if possible, by a group having the minimum number of facets with the same perimeter. Fig. 15 shows sixteen of the possible combinations both before (left) and after (right) facet reduction. Because any two neighboring model cells share vertices, the facets associated with the cells will necessarily share common edges, thereby creating a continuous surface, i.e., it is not possible for there to be a "hole" in the surface due to mismatched vertices. By adding facets to each model cell using this procedure, a surface which contains the domain of interest is generated.

Visualization allows for checking the model against some expectation. Although such checking is primarily subjective, it gives the opportunity to identify obvious errors or flaws in the model construction process, e.g., an irregularity in a spherical model or a large "bump" on a cell model which is not present in the confocal images. The stereolithography (STL) format is a standard used to represent surfaces occupying three-dimensional space. It is a common format and there is a variety of software allowing for visualization using this format. One of the requirements of the STL format is that no vertex lie on an edge at any point other than an endpoint of the edge, i.e., the endpoint of one edge does not lie between the endpoints of another edge. For this reason, the surface construction process uses facets which conform to this rule. This makes translating the surface to an STL format trivial.

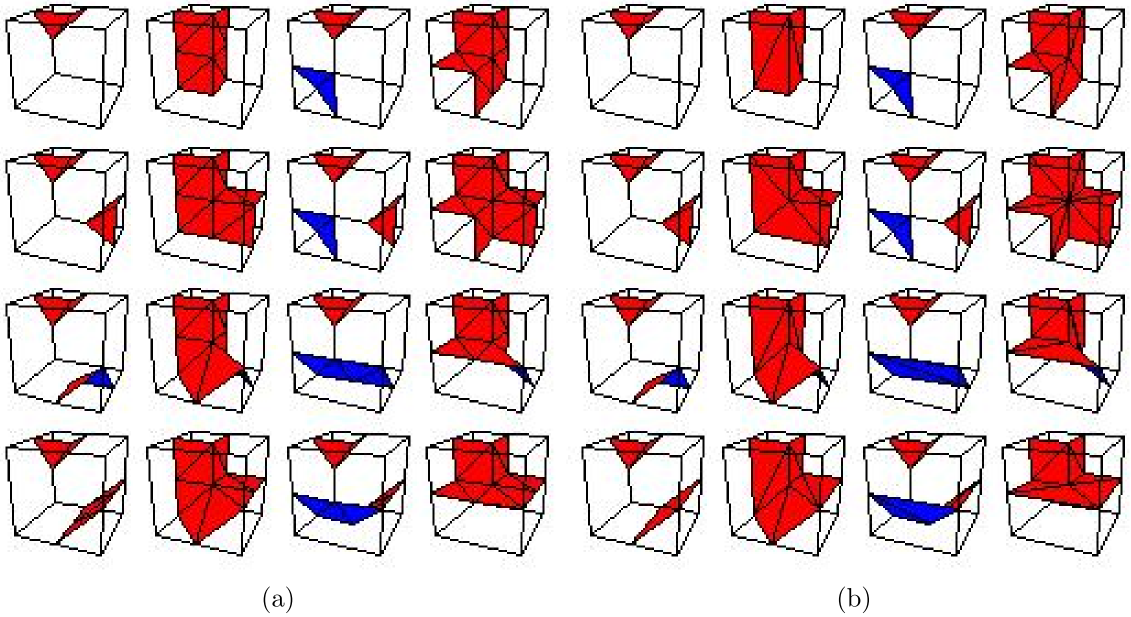
(a) (b)

Figure 15: 16 of the 256 possible facet combinations for a model cell, (a)before and (b)after facet reduction. Associating facet groups with cells rather than the individual tetrahedra simplifies processing.

Another advantage of creating the surface is for volume calculation. Given a surface made up of polygonal facets, the exact volume interior to the surface can be calculated. Thus, considering the model as an approximation of a physical object allows the volume of that object to be estimated. All cell model volumes discussed in this work are calculated using the constructed surface as a boundary.

Chapter 7: Evaluation of the FDTD program

7.1 Overview

To test the program a series of validation and evaluation simulations have been carried out. Unless specified otherwise, all of the simulations for validation and evaluation used a homogeneous sphere with a relative complex index of refraction of $1.0385 + i1.6804 \times 10^{-5}$, a Gaussian pulse with $1 \mu m$ wavelength in the host medium and pulse width of 30 time steps, an 8 cell PML, 8 cells between the heterogeneous and scattered field regions, a 5 cell scattered field region, and a grid resolution, $\frac{\lambda_h}{\Delta}$, of 30, where λ_h is the wavelength in the host medium. All simulations used a number of time steps equal to eight times the number needed for an incident pulse to travel across the total field region. The homogeneous sphere was chosen for comparison with Mie theory in the validation tests. The relative index of refraction was chosen to be equal to that of cytoplasm in an extracellular fluid.

The FDTD program has been continuously updated and improved since the original validated program was completed. Therefore, there are two sets of evaluation and validation results, those based on the original program and those based on the program at the time of this writing. Testing of the original program has been done on the Datastar cluster (DSCC) at the San Diego supercomputing center, the Lonestar Cray-Dell cluster (LSCC) at the Texas Advanced Computing Center at the University of Texas and one of the Biomedical Laser Laboratory computing clusters (BLCC) at East Carolina University. Tests on the DSCC were carried out on IBM P655 nodes which have 1.5GHz IBM Power4 processors and are connected by a 2GHz switch.

The LSCC consists of nodes having dual 3.06GHz Intel Xeon processors which are connected by a gigabit switch. The BMLL network consists of 8 nodes with Intel Xeon 3.06 GHz processors connected by a gigabyte switch. Testing of the current program has been done on the Lemieux computing cluster (PSCC) at the Pittsburgh supercomputing center. The PSCC consists of Compaq Alpha nodes containing Alpha EV6.8 1 GHz processors connected by a Quadrics interconnection network. The results are arranged so that the original validation and evaluation are presented first, followed by the latest results.

7.2 Program without the dispersion correction

To validate the code, several simulations have been carried out for spherical particles at various radii. The results of these simulations have been compared to Mie Theory, which provides an analytic solution. As shown in Table 1 and Table 2, Q_{ext} and g obtained using Mie theory are matched by the FDTD code. The maximum error for Q_{ext} is 3.44%. The errors for g are better with the magnitude of the maximum error begin 0.000998%. The FDTD results for the Mueller matrix elements S_{11}, S_{12}, S_{33}, and S_{43} have also been compared against the Mie theory results for spheres of the same radii. These results are shown if Fig. 16–19. Notice that the errors in the FDTD results are more pronounced in the larger scattering angles ($> 160°$), but overall the result is satisfactory.

With any parallel code, there can be a problem with task dependence. Task dependence is present if the results for simulations having the same parameters are different when run with a different numbers of PEs. To test for task dependence, the simulation has been run several times with a different number of PEs for each run. The Q_{ext} and g results are shown in Table 3 for a sphere of radius $1.6\mu m$ and

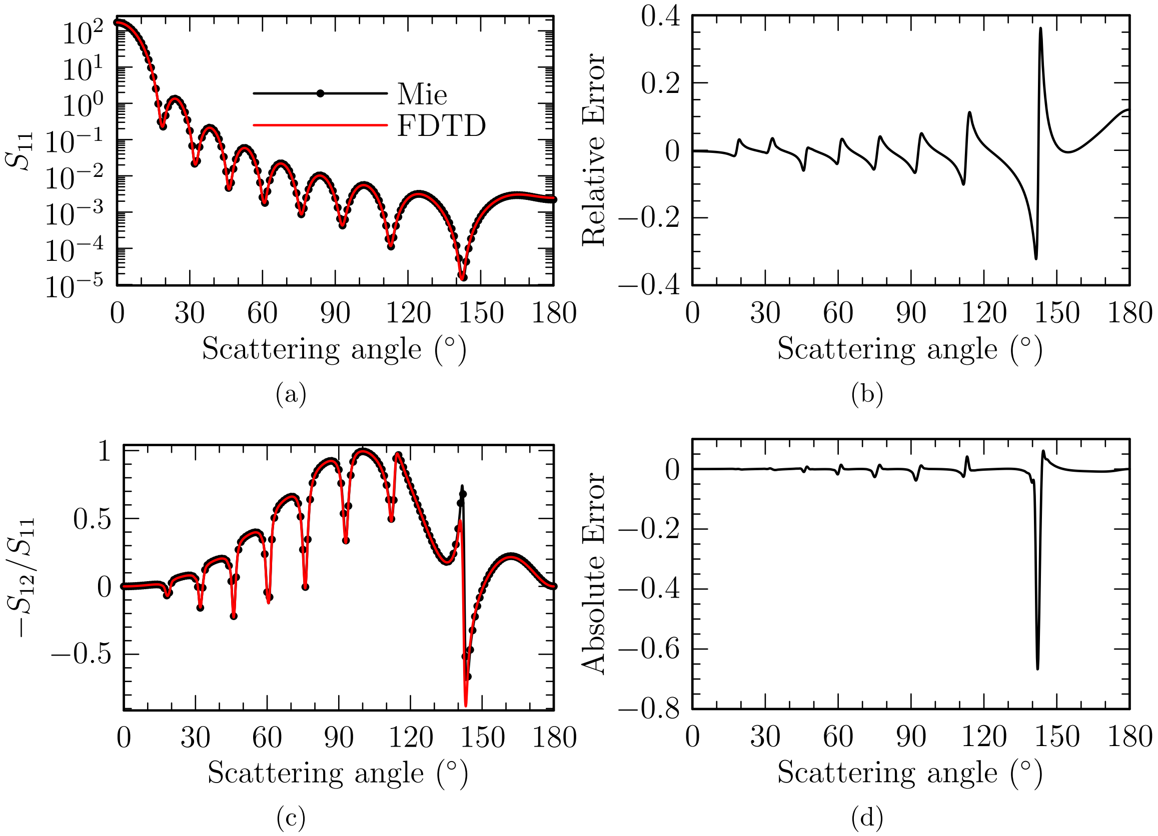

Figure 16: Comparison of (a)S_{11} and (c)S_{12}/S_{11} obtained by Mie theory and FDTD for a sphere of radius 1.6μm. (b),(d)The error between Mie theory and FDTD results for S_{11} and S_{12}/S_{11}, respectively.

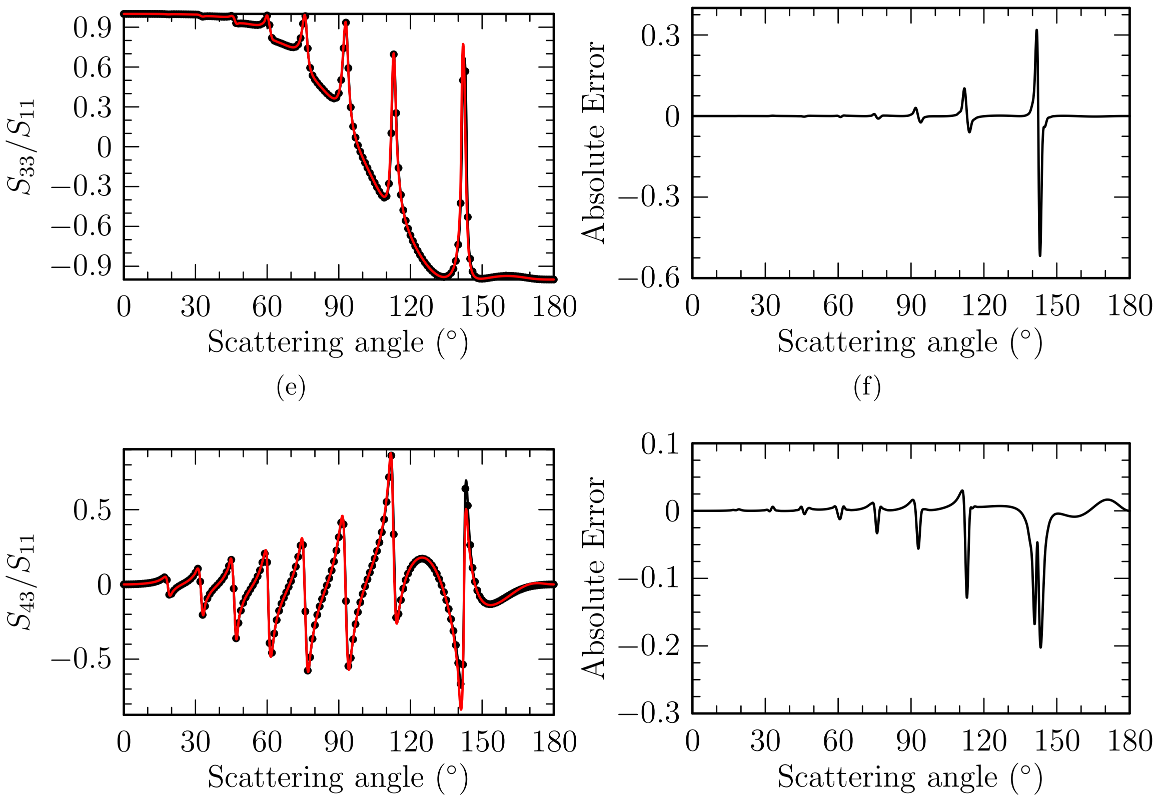

(e) (f)

(g) (h)

Figure 16: Comparison of (e)S_{33}/S_{11} and (g)S_{43}/S_{11} obtained by Mie theory and FDTD for a sphere of radius 1.6μm. (f),(h)The error between Mie theory and FDTD results for S_{33}/S_{11} and S_{43}/S_{11}, respectively.

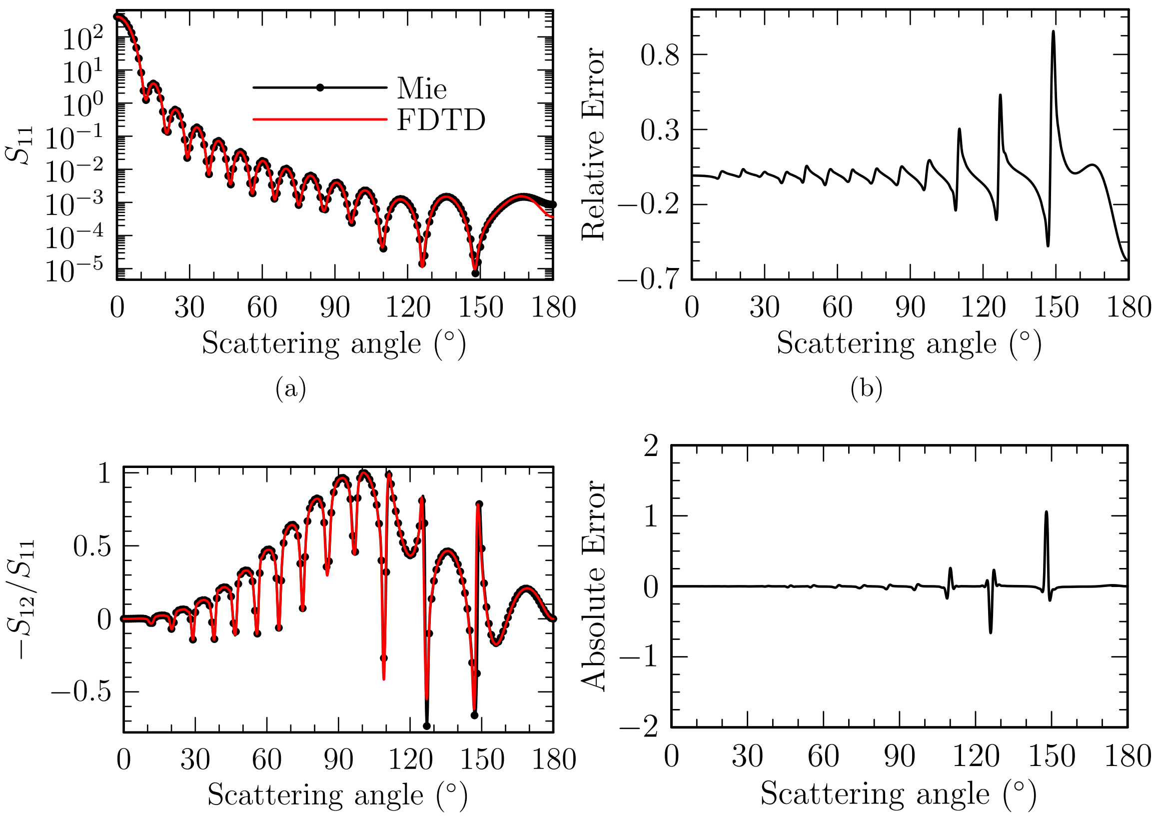

(a)

(b)

(c)

(d)

Figure 17: Comparison of (a)S_{11} and (c)S_{12}/S_{11} obtained by Mie theory and FDTD for a sphere of radius $2.5\mu m$. (b),(d)The error between Mie theory and FDTD results for S_{11} and S_{12}/S_{11}, respectively.

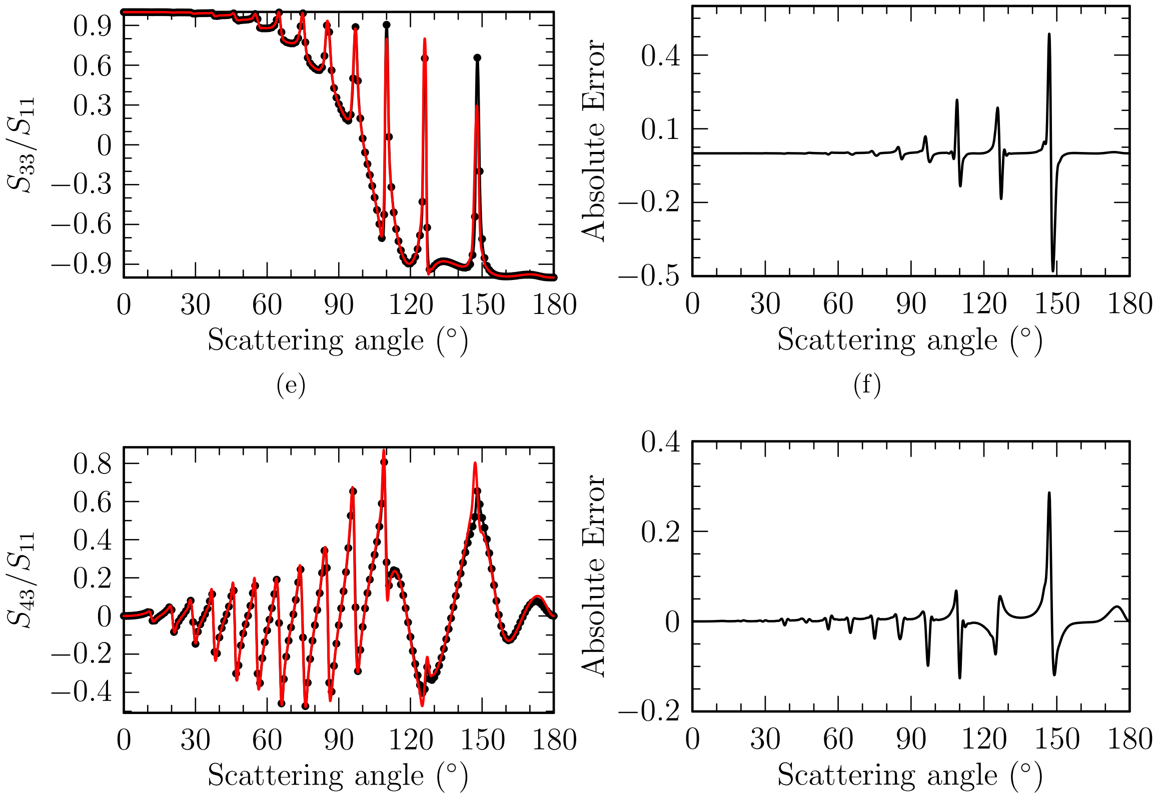

(e)

(f)

(g)

(h)

Figure 17: Comparison of (e)S_{33}/S_{11} and (g)S_{43}/S_{11} obtained by Mie theory and FDTD for a sphere of radius $2.5\mu m$. (f),(h)The error between Mie theory and FDTD results for S_{33}/S_{11} and S_{43}/S_{11}, respectively.

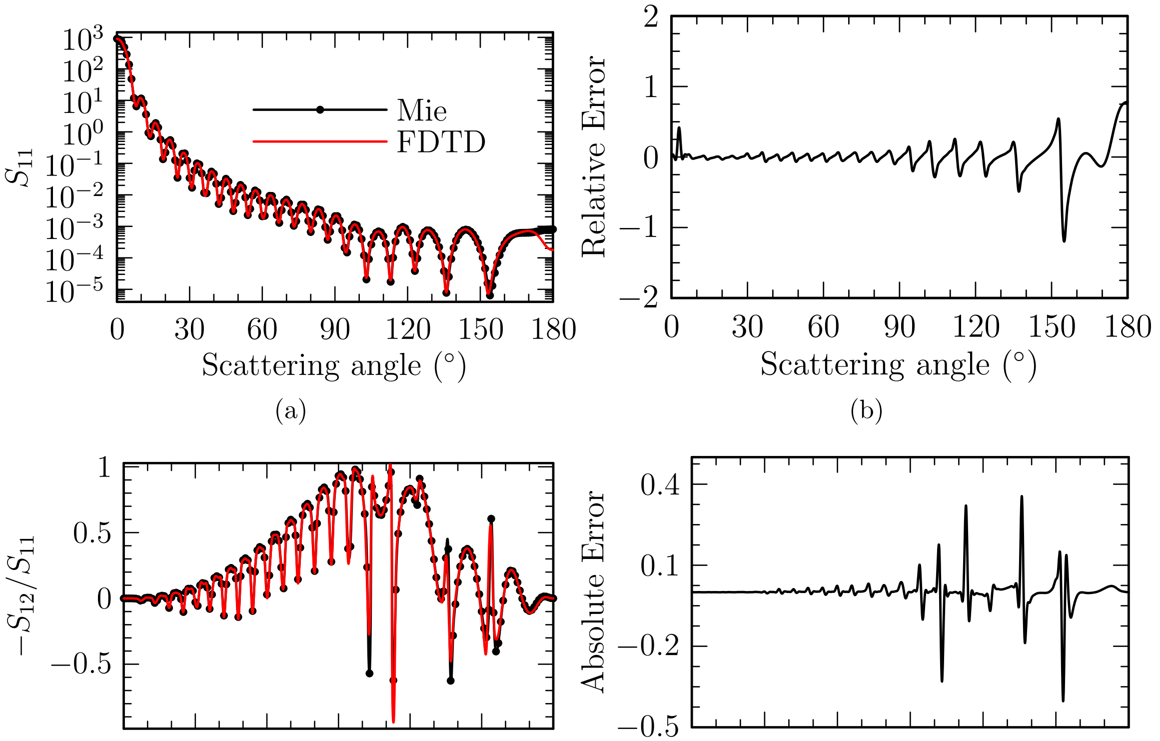

(a)

(b)

(c)

(d)

Figure 18: Comparison of (a)S_{11} and (c)S_{12}/S_{11} obtained by Mie theory and FDTD for a sphere of radius $3.75\mu m$. (b),(d)The error between Mie theory and FDTD results for S_{11} and S_{12}/S_{11}, respectively.

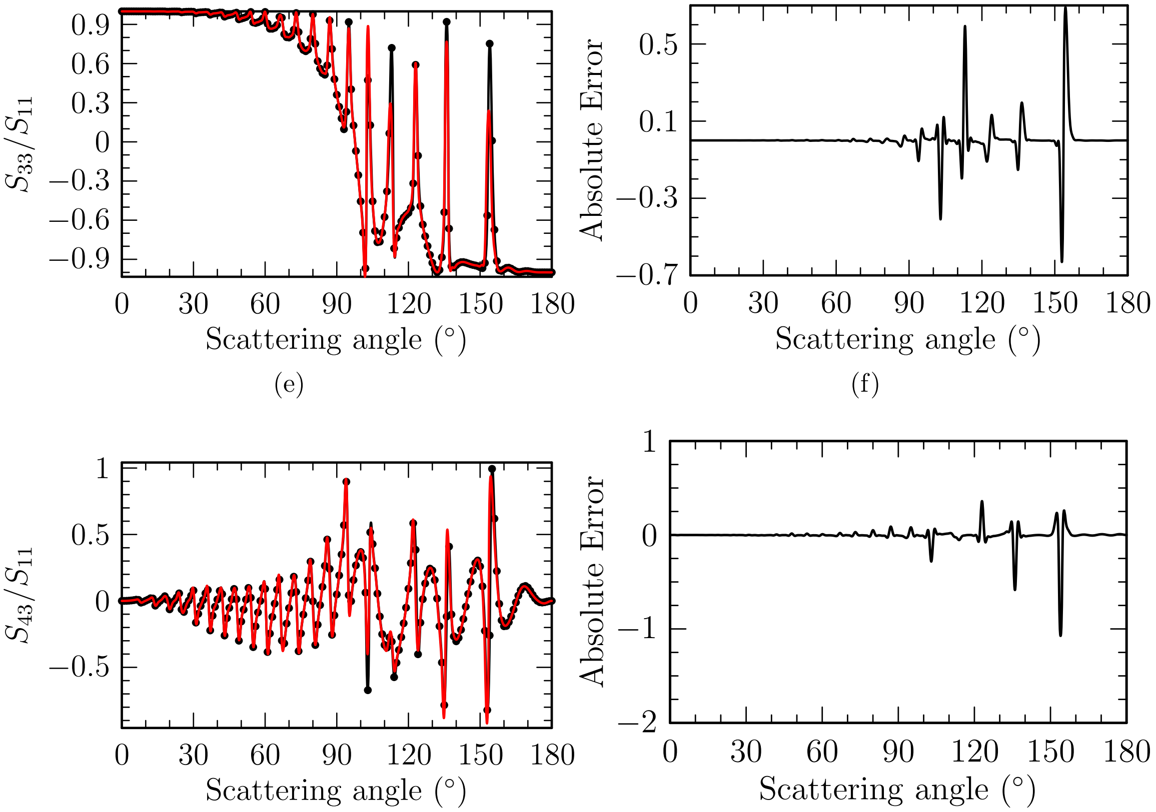

(e) (f)

(g) (h)

Figure 18: Comparison of (e)S_{33}/S_{11} and (g)S_{43}/S_{11} obtained by Mie theory and FDTD for a sphere of radius $3.75\mu m$. (f),(h)The error between Mie theory and FDTD results for S_{33}/S_{11} and S_{43}/S_{11}, respectively.

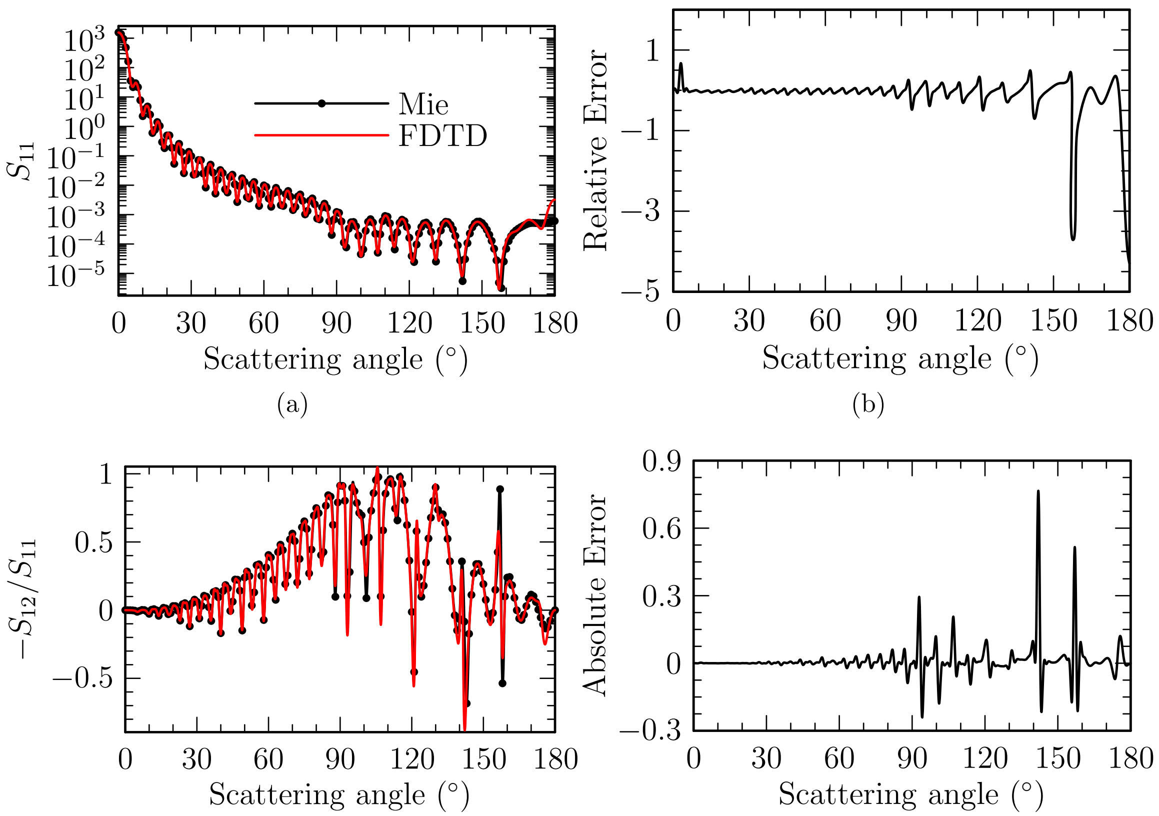

(a)

(b)

(c)

(d)

Figure 19: Comparison of (a)S_{11} and (c)S_{12}/S_{11} obtained by Mie theory and FDTD for a sphere of radius $5.0\mu m$. (b),(d)The error between Mie theory and FDTD results for S_{11} and S_{12}/S_{11}, respectively.

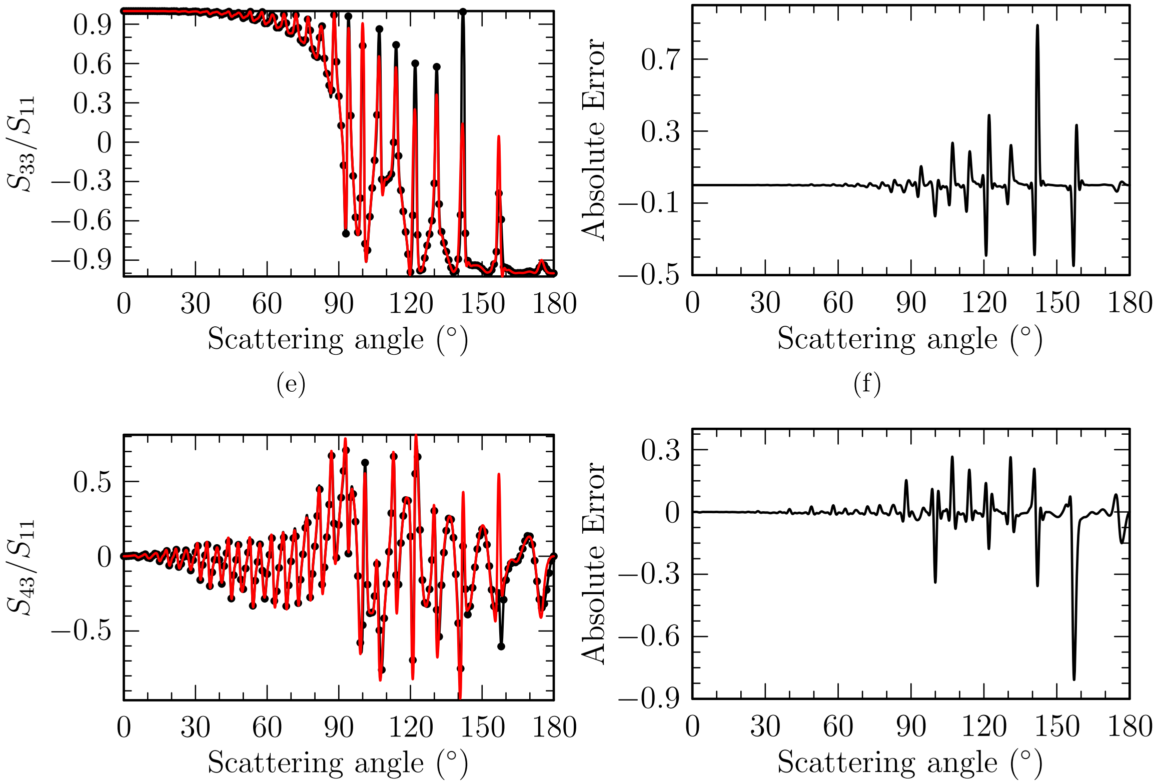

(e)

(f)

(g)

(h)

Figure 19: Comparison of (e)S_{33}/S_{11} and (g)S_{43}/S_{11} obtained by Mie theory and FDTD for a sphere of radius 5.0μm. (f),(h)The error between Mie theory and FDTD results for S_{33}/S_{11} and S_{43}/S_{11}, respectively.

Table 1: Comparison of Mie theory and FDTD extinction efficiency results for a sphere of various radii

Radius	Mie theory	FDTD	Error (%)
1.6	0.525195	0.515006	1.94
2.5	1.18466	1.16196	1.92
3.75	2.21194	2.15920	2.38
5.	2.99977	2.89645	3.44

Table 2: Comparison of Mie theory and FDTD anisotropy factor results for a sphere of various radii

Radius	Mie theory	FD-TD	Error (%)
1.6	0.981587	0.981685	-0.000998
2.5	0.990478	0.990538	-0.000606
3.75	0.994196	0.994194	0.0000201
5.	0.995327	0.995250	0.000774

are identical. In fact, all of the scalar properties and matrix elements obtained were identical except those which have an actual value of zero. For the zero values, the computed values were all less than 10^{-14}, although the computed values do not agree for simulations having a different number of PEs.

Table 3: Comparison of results with various number of PEs for a radii of $1.6\mu m$ and $2.5\mu m$

	$r = 1.6\mu m$		$r = 2.5\mu m$	
#PEs	Q_{ext}	g	Q_{ext}	g
Mie theory	0.525195	0.981587	1.18466	0.990478
1	0.515006	0.981685	1.16196	0.990538
2	0.515006	0.981685	1.16196	0.990538
4	0.515006	0.981685	1.16196	0.990538
8	0.515006	0.981685	1.16196	0.990538
16	0.515006	0.981685	1.16196	0.990538
32	0.515006	0.981685	1.16196	0.990538
64	0.515006	0.981685	1.16196	0.990538

Performance is a critical issue for the simulation. It is the primary reason that the parallel code has been developed. Table 4 shows the timing results for simulations of spheres of various radii carried out on LSCC using 32 PEs. The information includes the radius of the sphere, the heterogeneous size, i.e., the amount of space from the center of the grid to the boundary of the heterogeneous region, the homogeneous size, i.e., the amount of space between the heterogeneous region and the PML boundary. The timing information is given in terms of time domain calculation time, i.e., the amount of time used to carry out the FDTD simulation, and the frequency domain time, i.e., the amount time used in transforming the near field information into the Mueller matrix elements, and the wall time, which is the total amount of time used. Fig. 20 depicts the time vs. size information of Table 4. Ignoring communications overhead, it is expected that the problem time is nearly linear with respect to grid size. The first five data points of Fig. 20 indicate this; however, the data point corresponding to the largest size does not agree. The time dependence is complex due to the architecture of the both the nodes and the network as well as the state of the cluster during the time of the simulation. Testing on several platforms can be carried out to determine if the sixth point anomaly is due to the architecture, system state, or the code itself.

Table 4: Timing comparison for various problem sizes on the Lonestar cluster for various problem sizes

radius, μm	hetero. size, Δ	homo. size, Δ	volume, Δ^3	t time, s	ω time, s	wall time, s
0.8	33	13	1295029	253	113	398
1.0	41	13	1953125	385	235	670
1.2	49	13	2803221	579	463	1135
1.4	57	13	3869893	777	896	1812
1.6	65	13	5177717	1051	1192	2416
2.655	108	13	17373979	5591	7460	13727

Another measure of performance is how the time scales with an increasing number of PEs, a.k.a. speed-up. There are various common definitions for speed-up; the

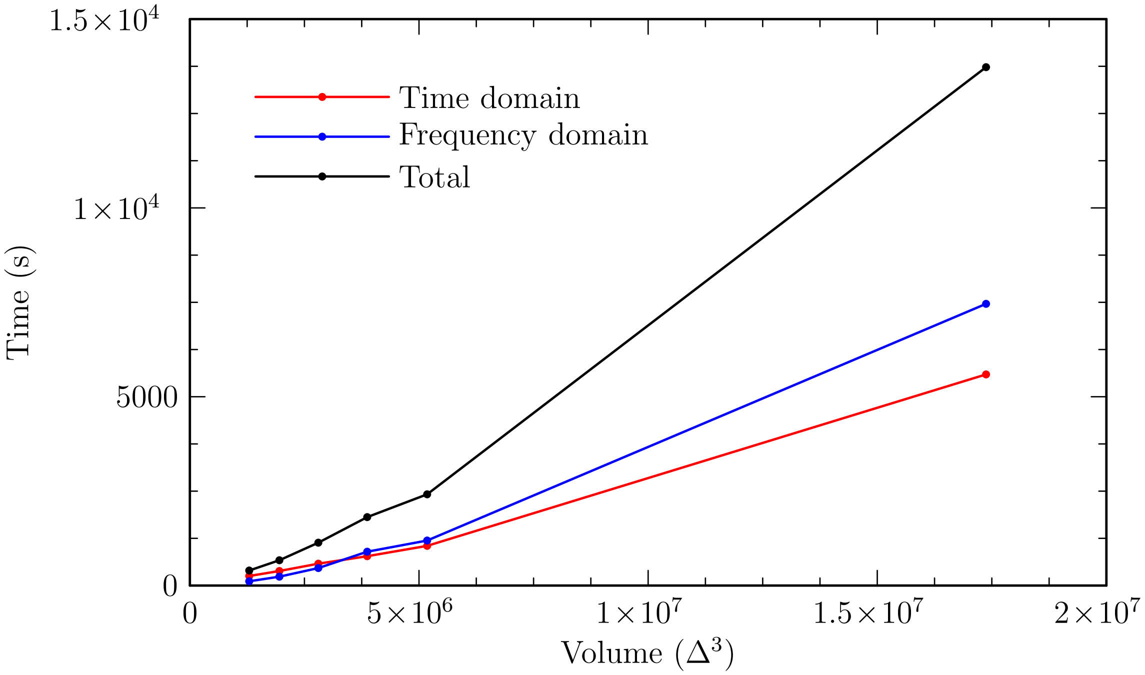

Figure 20: Timing results for spheres of various radii.

simplest of which is used here. Speed-up is defined as the ratio of the time used by 1 PE to that used by x number of PEs; thus, the ideal speed-up for x PEs is x. Simulations have been carried out on the three platforms mentioned to determine the speed-up of the code. Fig. 21 depicts the timing information and the speed-up and the ideal speed-up for simulations of two spheres, one (left) having a radius of $1.6\mu m$ and the other having a radius of $2.5\mu m$. From the figures, it can be seen that an almost ideal speed-up is achieved on DSCC, while LSCC and BLCC show a similar less than ideal speed-up. It should be noted that the ideal speed-up can not be achieved due to communications overhead, and in fact, the performance will degrade as the number of PEs is increased. This is due to the dependence communications time on the number of PEs. The speed-up obtained on each of these clusters is more than satisfactory to carry out the biological cell simulations. Tables 5–10 give the numerical data for Fig. 21 and are included for reference.

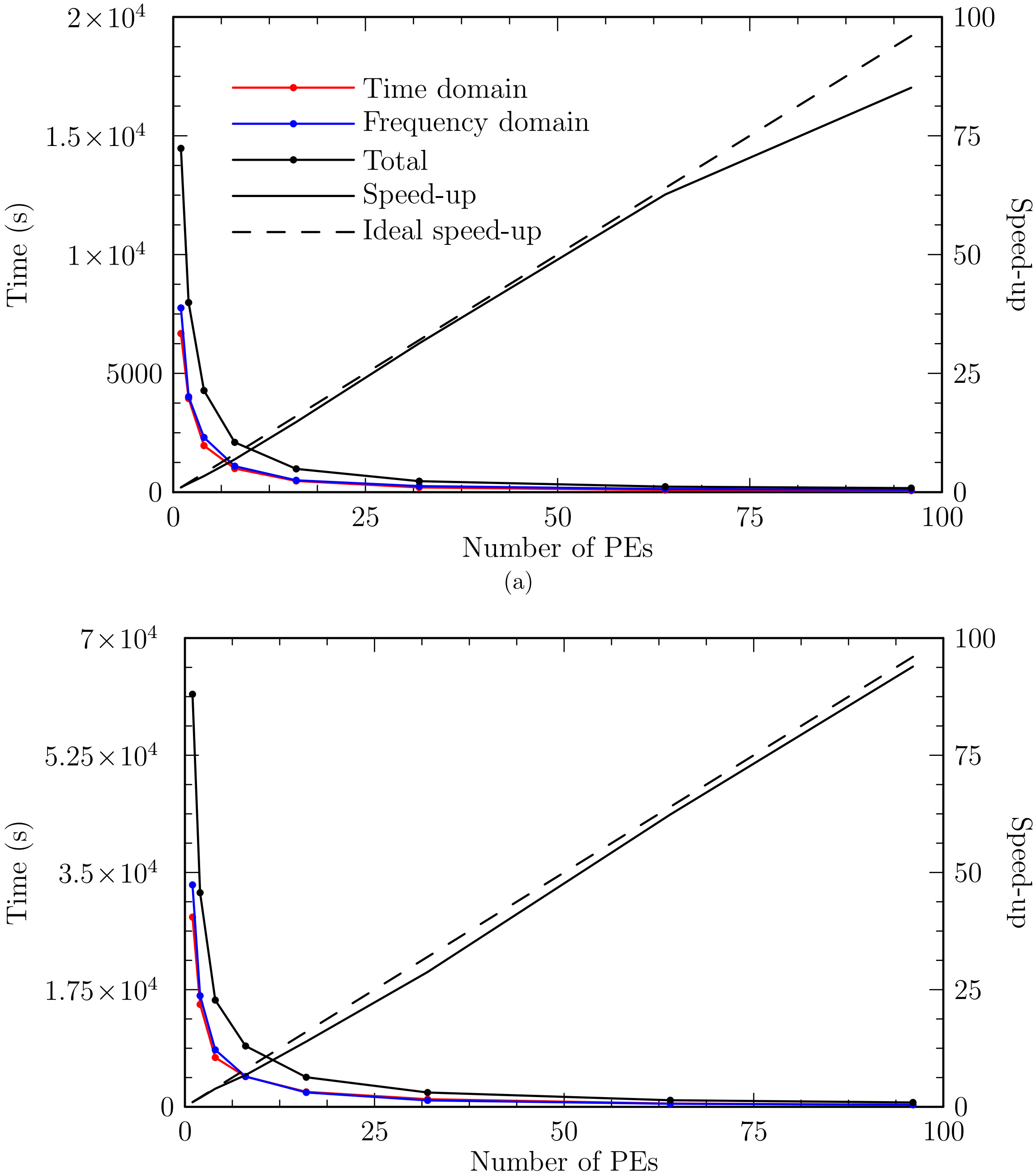

(a)

(b)

Figure 21: Speed-up on DSCC for (a)$r = 1.6\mu m$, (b)$r = 2.5\mu m$

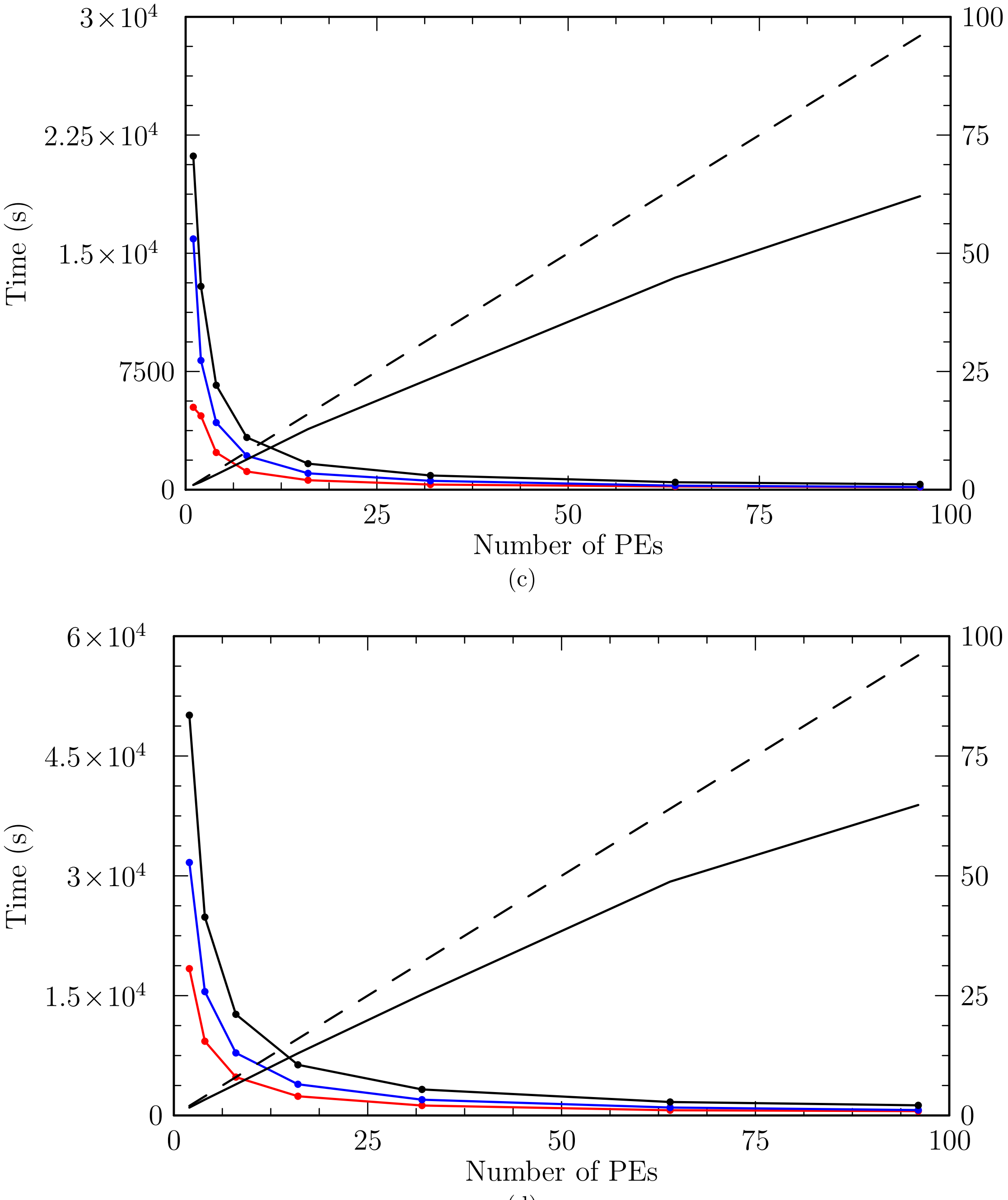

(c)

(d)

Figure 21: Speed-up on LSCC for (c)$r = 1.6\mu m$, (d)$r = 2.5\mu m$

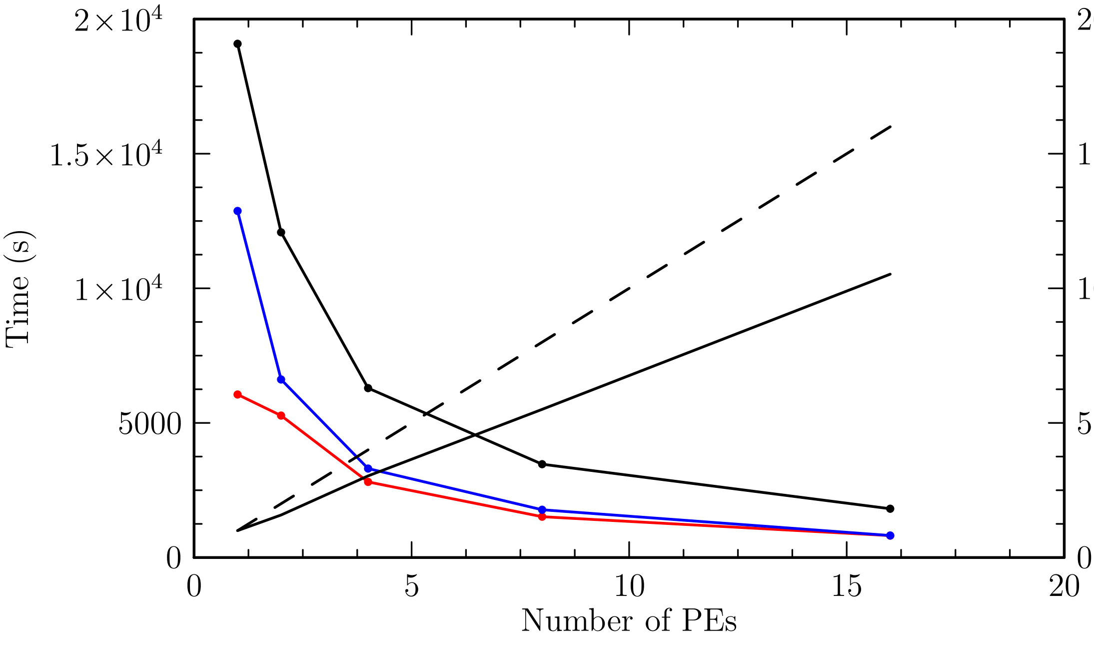

(e)

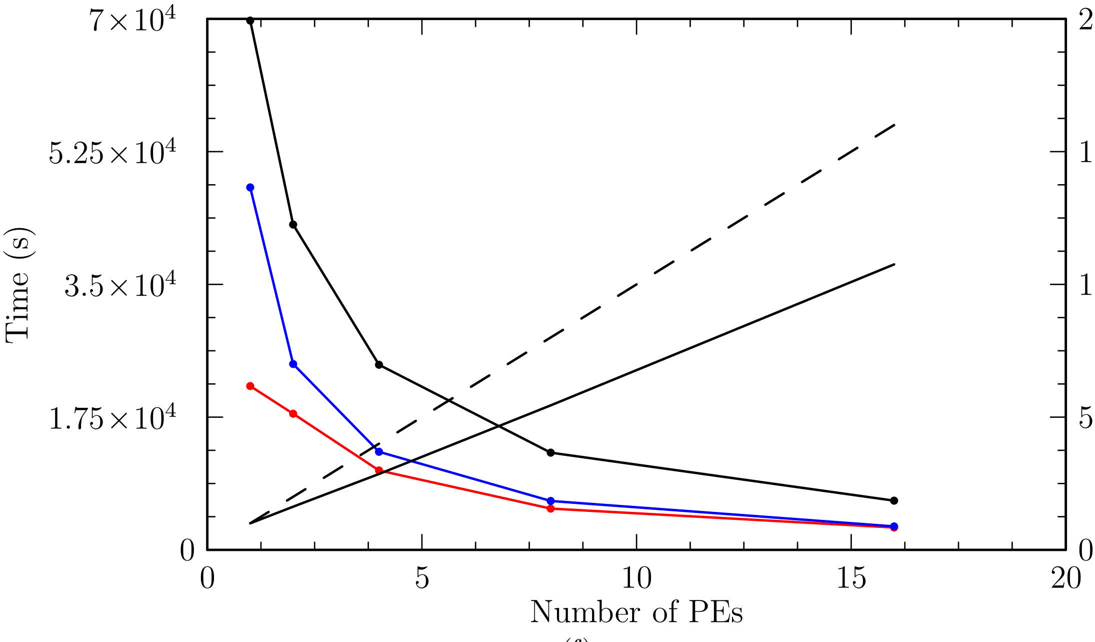

(f)

Figure 21: Speed-up on BLCC for (e)$r = 1.6\mu m$, (f)$r = 2.5\mu m$

Table 5: Timing comparison for various number of PEs on DSCC for a sphere of radius $1.6\mu m$

#PEs	t time, s	ω time, s	wall time, s	speed-up
1	6677	7754	14470	1.00
2	3940	4017	7980	1.81
4	1959	2303	4276	3.38
8	994	1093	2097	6.90
16	471	499	980	14.8
32	198	254	462	31.3
64	87	134	231	62.6
96	64	97	170	85.1

Table 6: Timing comparison for various number of PEs on DSCC for a sphere of radius $2.5\mu m$

#PEs	t time, s	ω time, s	wall time, s	speed-up
1	28334	33143	61611	1.00
2	15296	16595	31976	1.93
4	7366	8514	15935	3.87
8	4514	4531	9086	6.78
16	2238	2149	4423	13.9
32	1143	962	2142	28.8
64	490	462	988	62.4
96	319	301	656	93.9

Table 7: Timing comparison for various number of PEs on LSCC for a sphere of radius $1.6\mu m$

#PEs	t time, s	ω time, s	wall time, s	speed-up
1	5228	15912	21166	1.00
2	4686	8200	12902	1.64
4	2359	4259	6628	3.19
8	1154	2152	3313	6.39
16	601	1039	1652	12.8
32	325	562	901	23.5
64	205	254	472	44.8
96	157	172	341	62.1

Table 8: Timing comparison for various number of PEs on LSCC for a sphere of radius 2.5μm

#PEs	t time, s	ω time, s	wall time, s	speed-up
2	18379	31669	50108	1.64
4	9289	15503	24832	3.31
8	4802	7829	12661	6.49
16	2404	3904	6341	13.0
32	1245	1974	3257	25.2
64	651	992	1685	48.8
96	543	675	1269	64.8

Table 9: Timing comparison for various number of PEs on BLCC for a sphere of radius 1.6μm

#PEs	t time, s	ω time, s	wall time, s	speed-up
1	6056	12873	19082	1.00
2	5273	6614	12080	1.58
4	2809	3305	6293	3.03
8	1517	1775	3467	5.50
16	815	818	1813	10.53

Table 10: Timing comparison for various number of PEs on BLCC for a sphere of radius 2.5μm

#PEs	t time, s	ω time, s	wall time, s	speed-up
1	21598	47783	69775	1.00
2	17950	24503	42886	1.63
4	10471	12932	24405	2.86
8	5443	6450	12819	5.44
16	2949	3097	6489	10.8

7.3 Dispersion corrected program

A series of validation tests have been carried out for an updated program using the dispersion correction described in §3.5. These tests were carried out for comparison with DDA method[48]. This series of tests required that the error for the extinction cross section be less than 1% and that the root mean square relative error in S_{11} be less than 25%. This differs from the tests of the previous sections which fixed λ/Δ and the number of time steps. Thus, these new tests give the smallest λ/Δ and number of time steps which conform to the criteria. The range of the relative refractive index, m, was between 1.02 and 2 and the size parameters s range from 10 to 100 (although not all combinations were tested). Table 11 summarizes the test results. The parentheses appearing around a result indicate that the test criteria were not met for that result. Note that all but three tests were able to meet the criteria, and that the non-conforming results are still satisfactory when considering the purpose of the simulation.

Also, two tests have been carried out for comparison with the validation results of the previous section. The parameters of these tests are the same as those of the previous section for $r = 1.6, 2.5$; with the exceptions that the number of times steps is equal to three times that required for the incident wave to travel across the heterogeneous region (eight times in previous), and that the heterogeneous space is two grid cells thick (thirteen grid cells in previous). Table 12 and Table 13 show the extinction cross section and anisotropy factor for both the dispersion corrected and non-dispersion corrected programs. The errors are reduced by an order of magnitude for Q_{ext} and increase for g, but note that the error for g remains small ($\approx 0.01\%$). Fig. 22 and Fig. 23 show the Mueller matrix elements resulting from both programs. Again, the dispersion corrected result is clearly better than those without the disper-

Table 11: Errors in extinction cross section and anisotropy factor, resolution, and time step information for the dispersion corrected validation tests.

m	s	RE Q_{ext}	RMS RE S_{11}	λ/Δ	time steps
1.02	10	4.3×10^{-3}	0.17	12	275
.	20	9.3×10^{-4}	0.22	14	509
.	30	7.9×10^{-3}	0.22	13	651
.	40	3.3×10^{-3}	0.21	22	1398
.	60	5.9×10^{-3}	0.20	32	4004
.	80	4.3×10^{-3}	(0.33)	32	5239
.	100	.	.		
1.08	10	5.5×10^{-3}	0.064	18	453
.	20	1.0×10^{-2}	0.063	19	1005
.	30	9.3×10^{-3}	0.054	19	2531
.	40	9.5×10^{-3}	0.053	10	1928
.	60	8.3×10^{-3}	0.072	18	2509
.	80	3.8×10^{-3}	0.071	22	4009
1.2	10	7.6×10^{-3}	0.024	18	671
.	20	9.3×10^{-3}	0.037	20	1589
.	30	2.5×10^{-3}	0.075	24	3321
.	40	9.1×10^{-3}	0.25	18	3837
.	60	6.0×10^{-3}	0.25	25	13762
1.4	10	8.9×10^{-3}	0.14	10	1047
.	20	9.8×10^{-3}	0.17	37	10333
.	30	8.2×10^{-3}	0.19	23	11013
.	40	(1.5×10^{-2})	0.24	32	21580
1.7	10	8.0×10^{-3}	0.22	8	2323
.	20	8.0×10^{-3}	0.24	18	13101
.	30	1.1×10^{-2}	0.12	30	39751
2.	10	8.3×10^{-3}	0.16	11	7481
.	20	8.3×10^{-3}	0.14	20	30693

sion correction.

Table 12: Comparison of errors in extinction cross section with and without dispersion correction.

radius	Mie theory	Q_{ext} w/	Error w/ (%)	Q_{ext} w/o	error w/o (%)
1.6	0.525195	0.524461	0.14	0.515006	1.94
2.5	1.18466	1.18329	0.11	1.16196	1.92

Table 13: Comparison of errors in anisotropy factor with and without dispersion correction.

radius	Mie theory	g w/	Error w/ (%)	g w/o	error w/o (%)
1.6	0.981587	0.981702	-1.17×10^{-2}	0.981685	-9.98×10^{-4}
2.5	0.990478	0.990577	-9.97×10^{-3}	0.990538	-6.06×10^{-4}

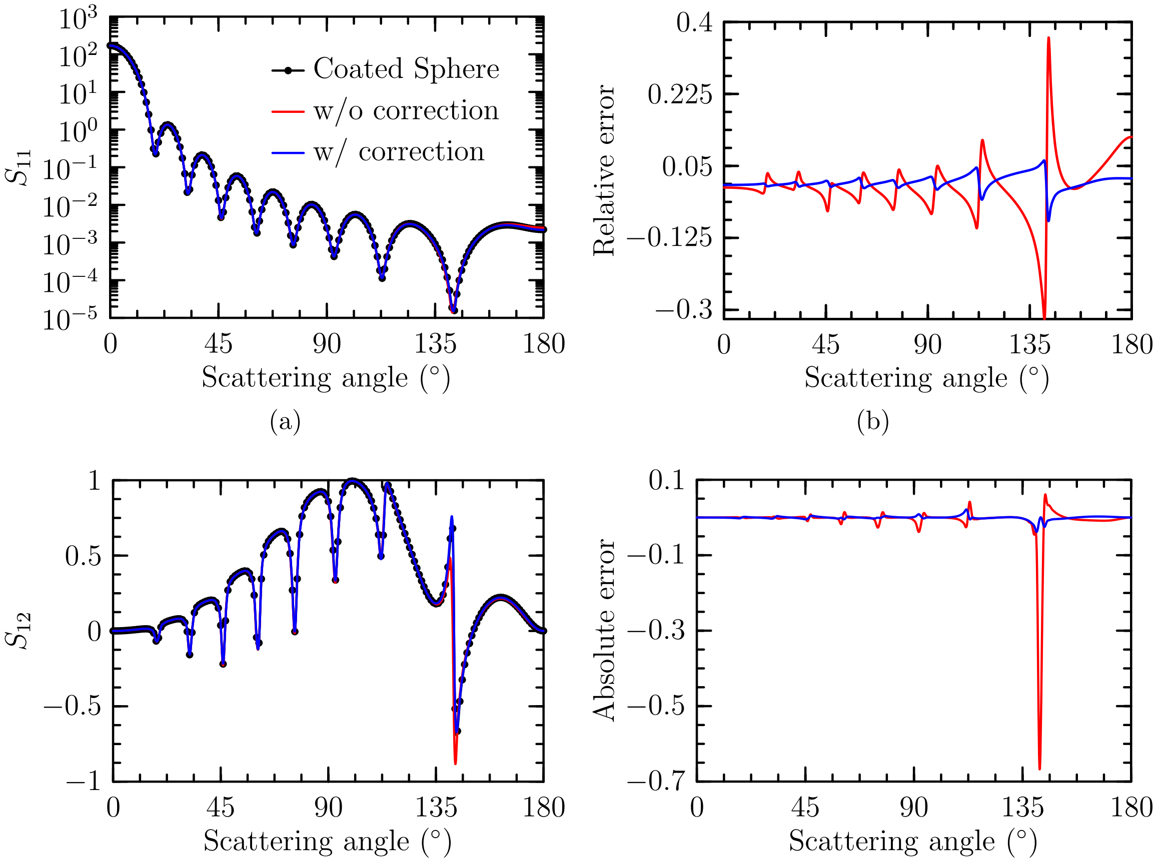

(a)

(b)

(c)

(d)

Figure 22: Comparison of (a)S_{11} and (c)S_{12}/S_{11} obtained by Mie theory and FDTD for a sphere of radius $1.6\mu m$. (b),(d)The error between Mie theory and FDTD results for S_{11} and S_{12}/S_{11}, respectively.

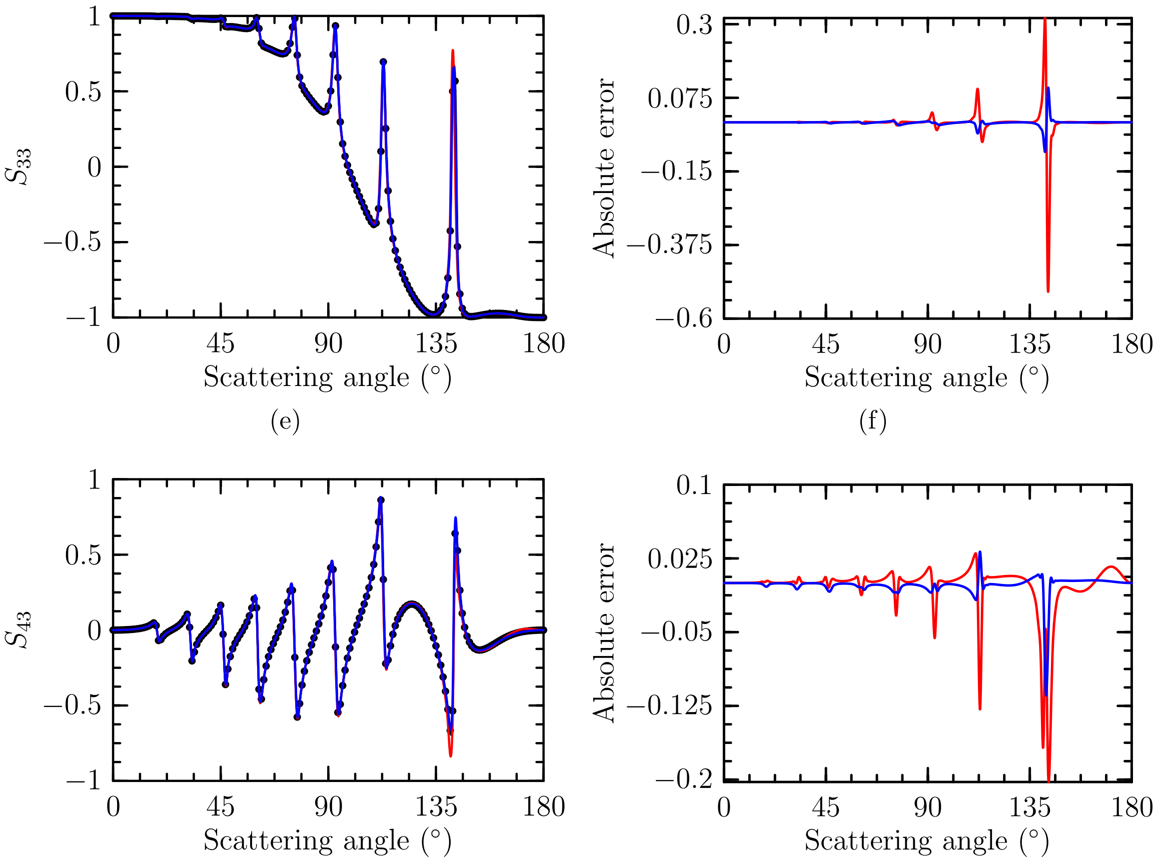

(e) (f)

(g) (h)

Figure 22: Comparison of (e)S_{33}/S_{11} and (g)S_{43}/S_{11} obtained by Mie theory and FDTD for a sphere of radius $1.6\mu m$. (f),(h)The error between Mie theory and FDTD results for S_{33}/S_{11} and S_{43}/S_{11}, respectively.

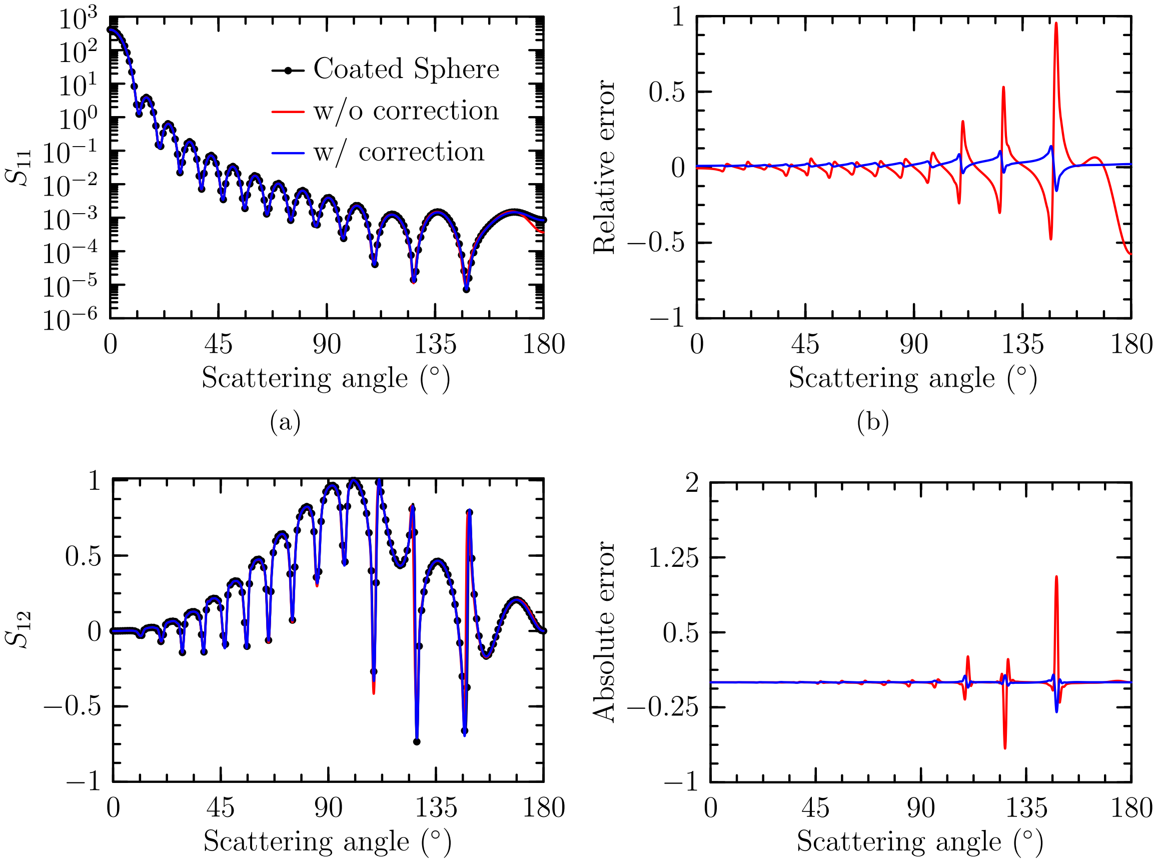

(a) (b)

(c) (d)

Figure 23: Comparison of (a)S_{11} and (c)S_{12}/S_{11} obtained by Mie theory and FDTD for a sphere of radius $2.5\mu m$. (b),(d)The error between Mie theory and FDTD results for S_{11} and S_{12}/S_{11}, respectively.

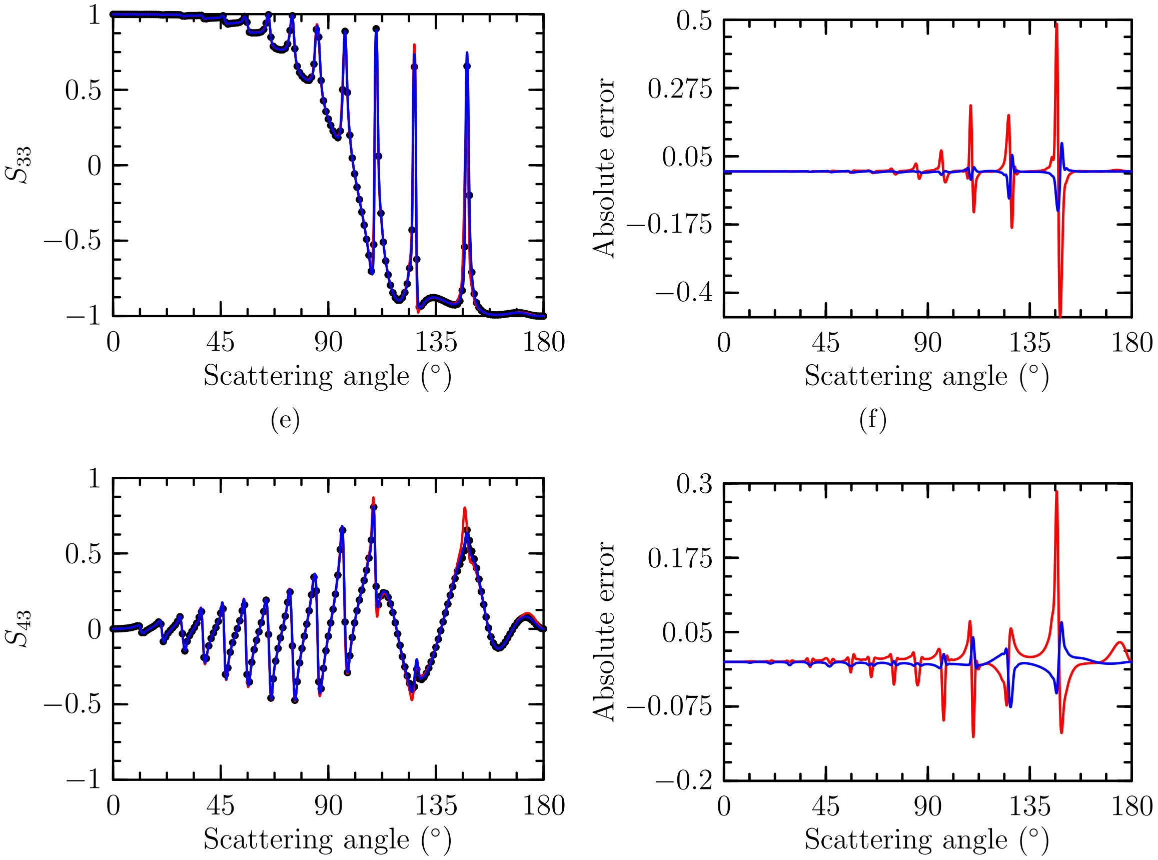

(e) (f)

(g) (h)

Figure 23: Comparison of (e)S_{33}/S_{11} and (g)S_{43}/S_{11} obtained by Mie theory and FDTD for a sphere of radius $2.5\mu m$. (f),(h)The error between Mie theory and FDTD results for S_{33}/S_{11} and S_{43}/S_{11}, respectively.

Chapter 8: Red blood cells

8.1 The red blood cell

The red blood cell (RBC) can be modeled as a fluid filled sack with an inelastic but deformable membrane. When an RBC travels through capillaries, it deforms due to the pressure gradient and drag along the capillary wall[49]. Several previous studies involving the deformation of RBCs in capillaries have been reported[36, 37, 38, 49, 50]. Zarda et al. [49] have described the deformations under these conditions in terms of a unitless pressure gradient, Δ_P. In that study, the deformations are assumed to change only the shape of the RBC, the volume and surface area are preserved. The model of that study has been chosen to study the effect of shape on light scattering distributions.

8.2 The RBC model

Simulations have been carried out for five models corresponding to five different values of Δ_P. The cross-sections of these models are shown in Fig. 24. The 3D models for four of these parameters are shown in Fig. 25. The volumes of the models vary within 2% of the target value $94.1\mu m_3$ and the surface areas of the models vary within 7%–12% of the target value of $134\mu m^2$. For the simulations, a wavelength of $1\mu m$ was used with $\Delta = n_h/25$. The host medium was given a refractive index of 1.350[3], corresponding to blood plasma, and the RBC model was given a refractive index of $1.4 + i1.6804 \cdot 10^{-5}$[3, 24], which corresponds to an RBC with an oxygen saturation of 97%. The simulation models are oriented so that the azimuthal angle for the incident field is measured from the x-axis and the polar angle from the axis of symmetry for

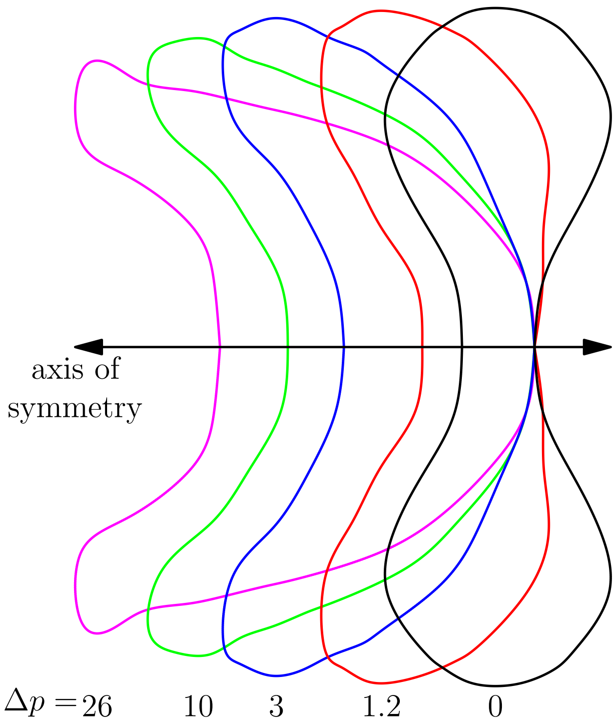

Figure 24: Red blood cell cross-sections for $\Delta_P = 0, 1.2, 3, 10, 26$

the RBC as shown in Fig. 26.

8.3 The simulation results

Fig. 27 shows S_{11} as a function of both the polar and azimuthal scattering angles for (a,b)$\Delta p = 0$, (c,d)$\Delta p = 3$, and (e,f)$\Delta p = 26$ with a field incident at (a,c,e)$\theta_i = -30°$ and $\phi_i = 0°$, and (b,d,f)$\theta_i = 30°$ and $\phi_i = 0°$. From the figure, the shape dependence can be seen by comparing (a), (c), and (e) or (b), (d), and (f). Examining the plots in quadrants, i.e., by drawing lines at $\theta = 90°$ and $\phi = 180°$, shows that the same quadrant has similar patterns in each of the plots. However, the differences indicate the possibility to distinguish the three pressure gradients, particularly the differences in the upper-left and lower-right quadrants.

Figures 28–32 show S_{11}, $-S_{12}/S_{11}$, S_{22}/S_{11}, S_{33}/S_{11}, and S_{34}/S_{11} averaged over

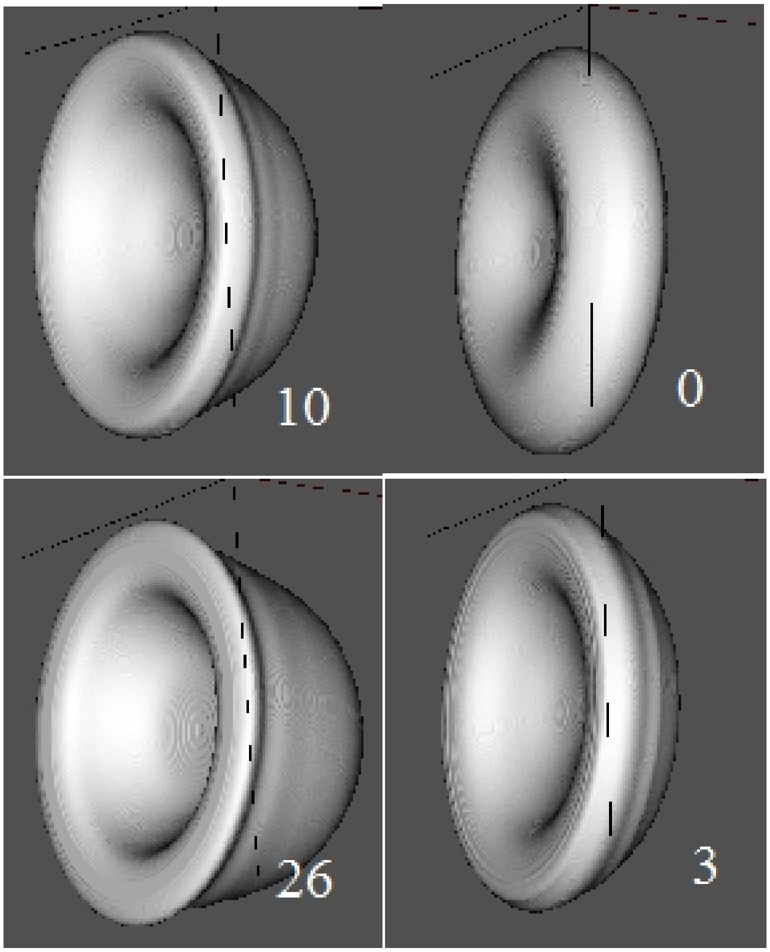

Figure 25: 3D red blood cell models for $\Delta_P = 0, 3, 10, 26$

Figure 26: For the simulations, the RBC is oriented such that the azimuthal angle is measured from the x-axis and the polar angle for the axis of symmetry of the RBC.

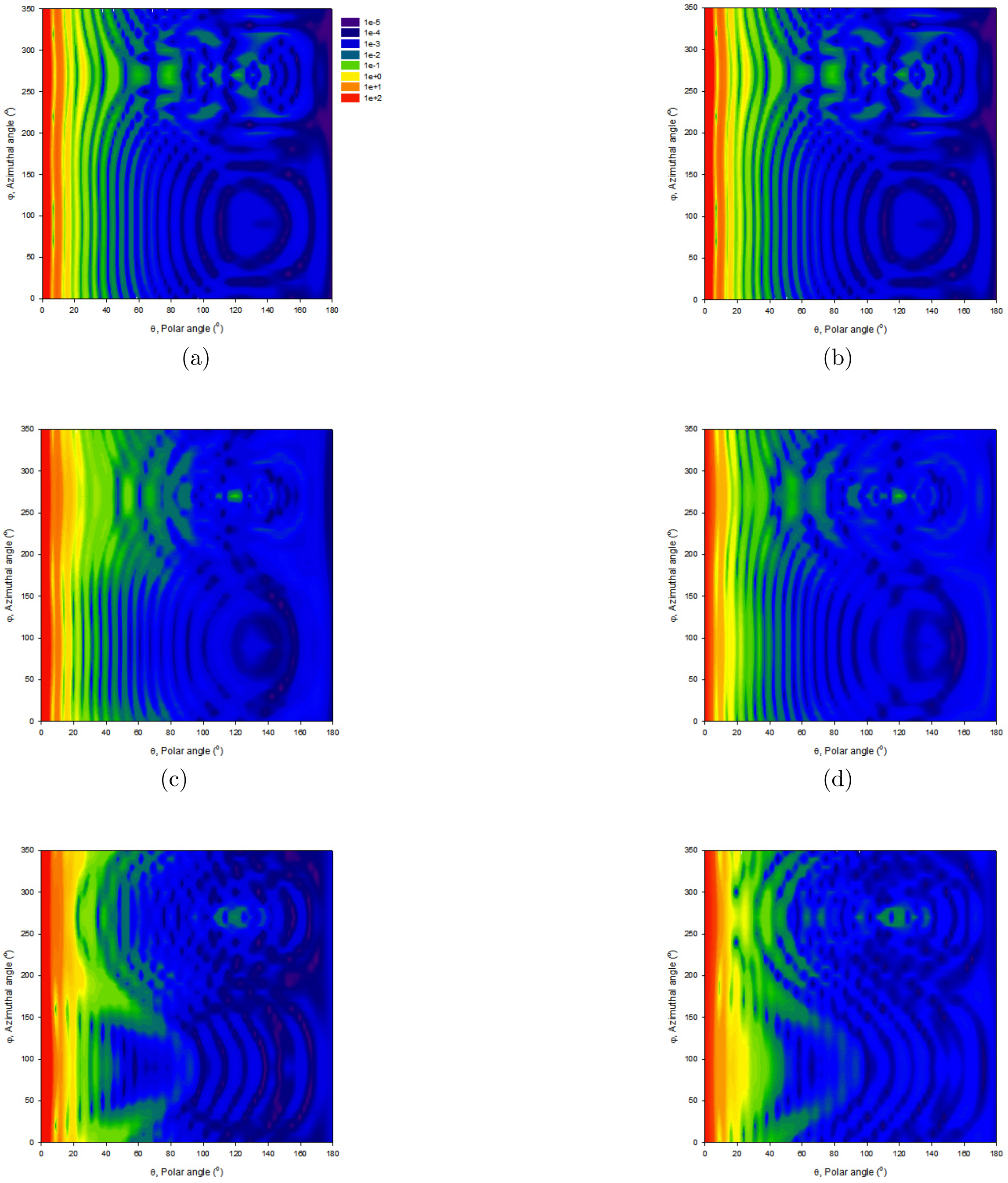

(a) (b) (c) (d) (e) (f)

Figure 27: $S_{11}(\theta, \phi)$ for (a,c,e) $\Delta p = 0, 3, 26$ with a $\theta_i = -30°, \phi_i = 0°$ incident wave and (b,d,f) $\Delta p = 0, 3, 26$ with a $\theta_i = 30°, \phi_i = 0°$ incident wave

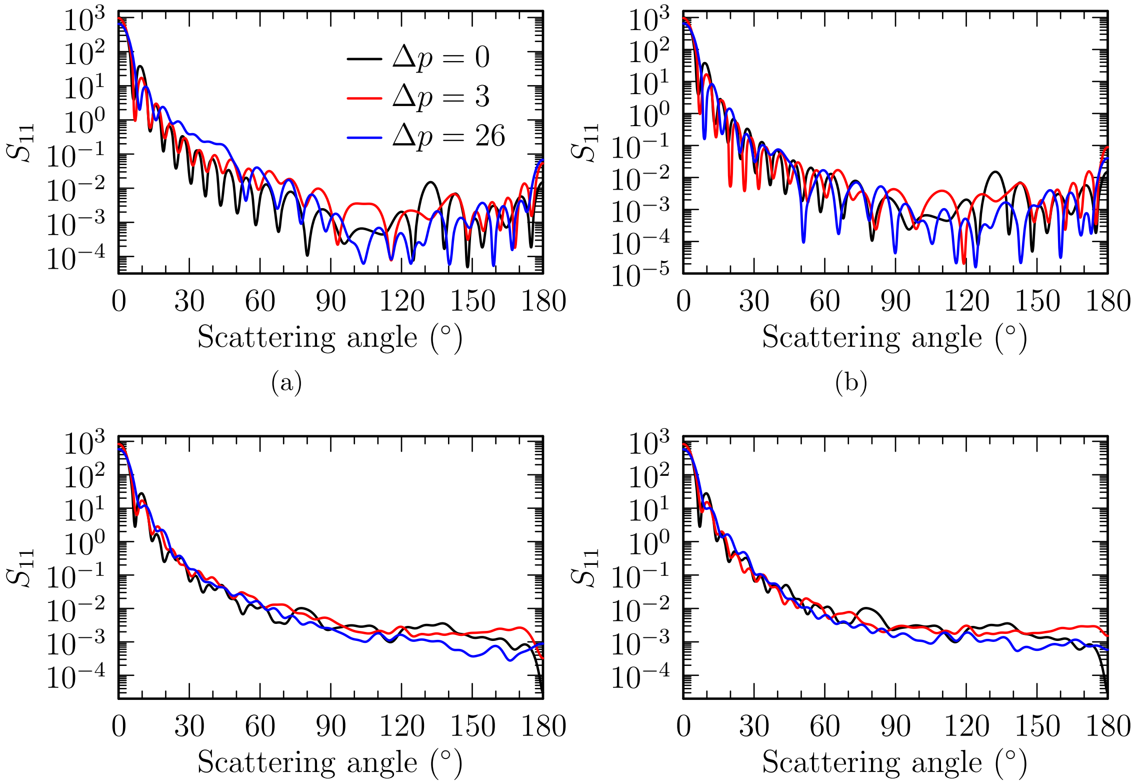

(a) (b) (c) (d)

Figure 28: S_{11} averaged over the azimuthal scattering angle for (a)$\theta_i = 0°$, (b)$\theta_i = 180°$, (c)$\theta_i = 30°$, and (d)$\theta_i = 150°$ for $\Delta p = 0, 3, 26$.

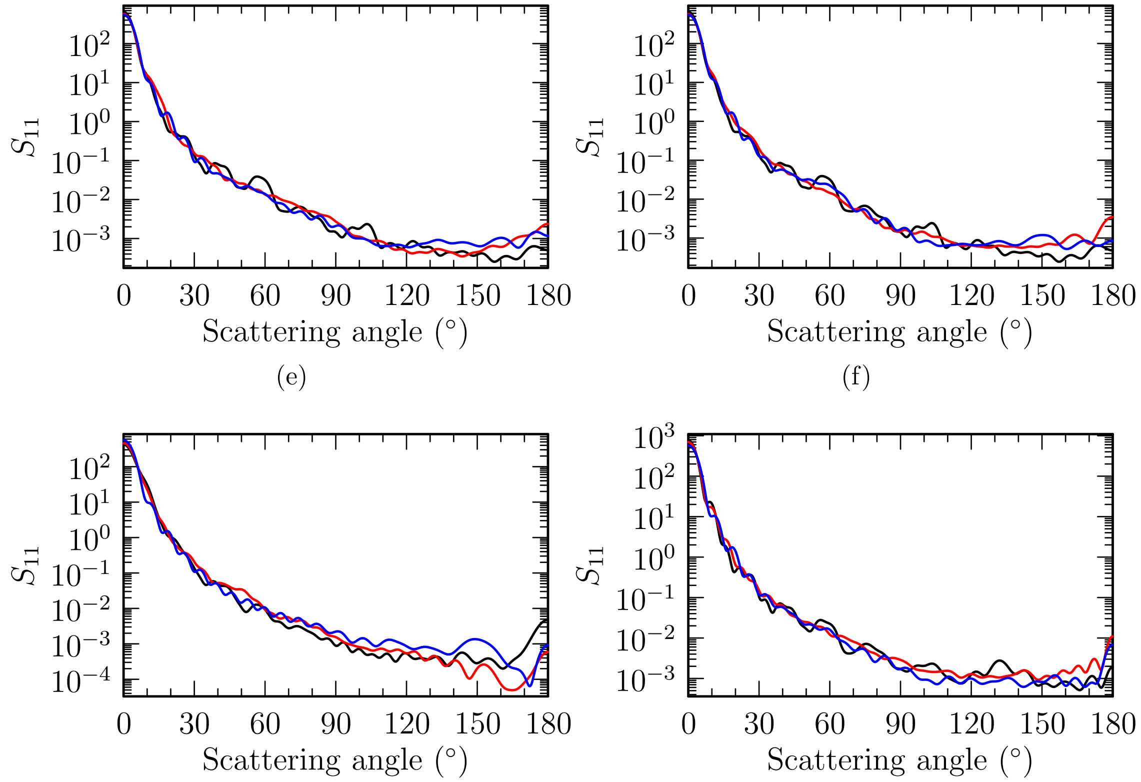

(e) (f)

(g) (h)

Figure 28: S_{11} averaged over the azimuthal scattering angle for (e)$\theta_i = 60°$, (f)$\theta_i = 120°$, (g)$\theta_i = 150°$, and (h)averaged over all θ_i for $\Delta p = 0, 3, 26$.

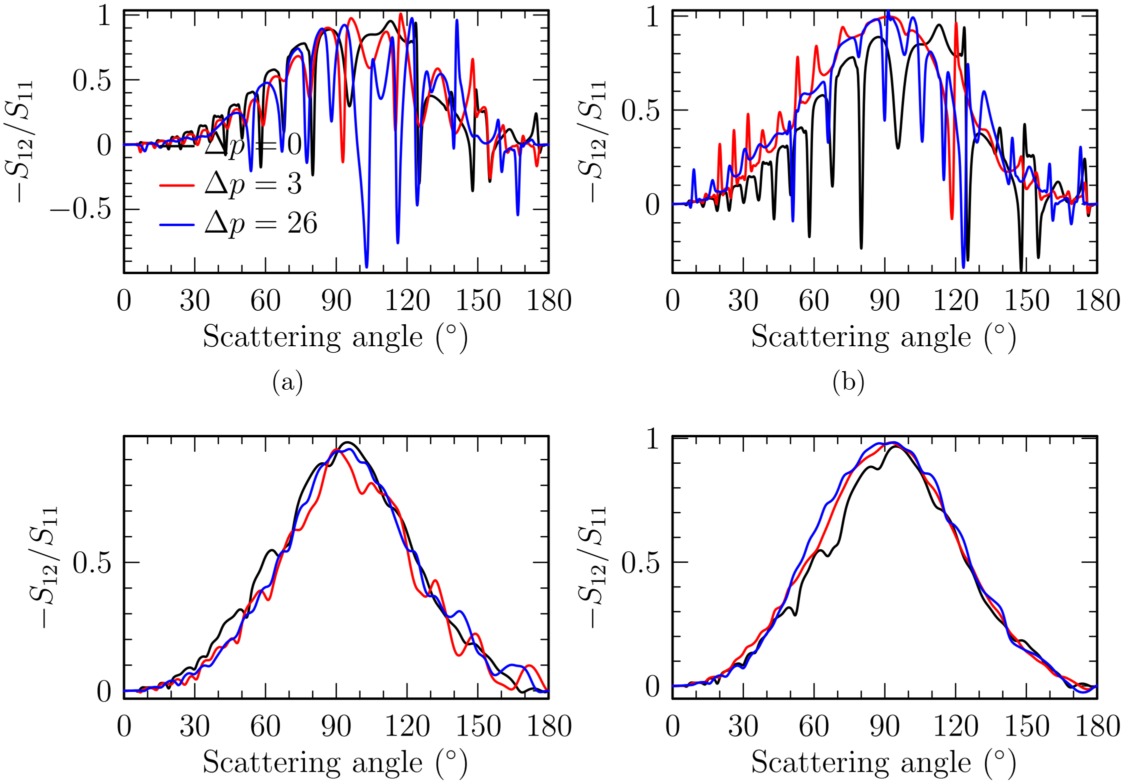

(a)

(b)

(c)

(d)

Figure 29: $-S_{12}/S_{11}$ averaged over the azimuthal scattering angle for (a)$\theta_i = 0°$, (b)$\theta_i = 180°$, (c)$\theta_i = 30°$, and (d)$\theta_i = 150°$ for $\Delta p = 0, 3, 26$.

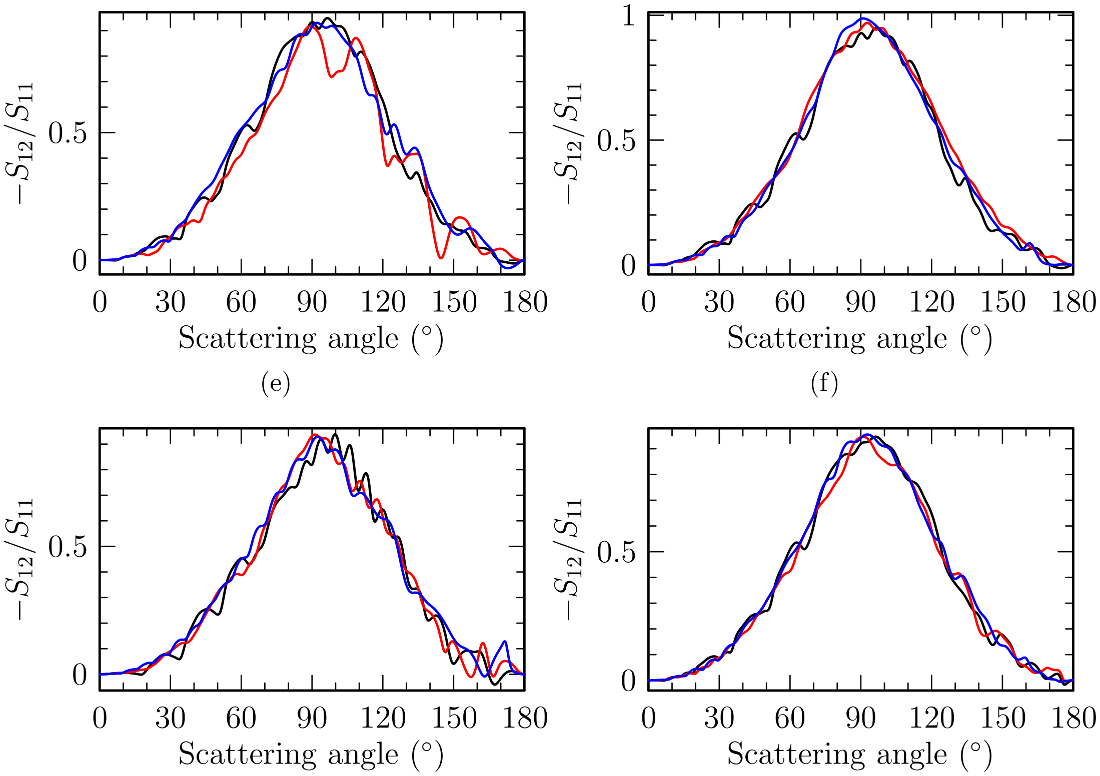

(e) (f)

(g) (h)

Figure 29: $-S_{12}/S_{11}$ averaged over the azimuthal scattering angle for (e)$\theta_i = 60°$, (f)$\theta_i = 120°$, (g)$\theta_i = 150°$, and (h)averaged over all θ_i for $\Delta p = 0, 3, 26$.

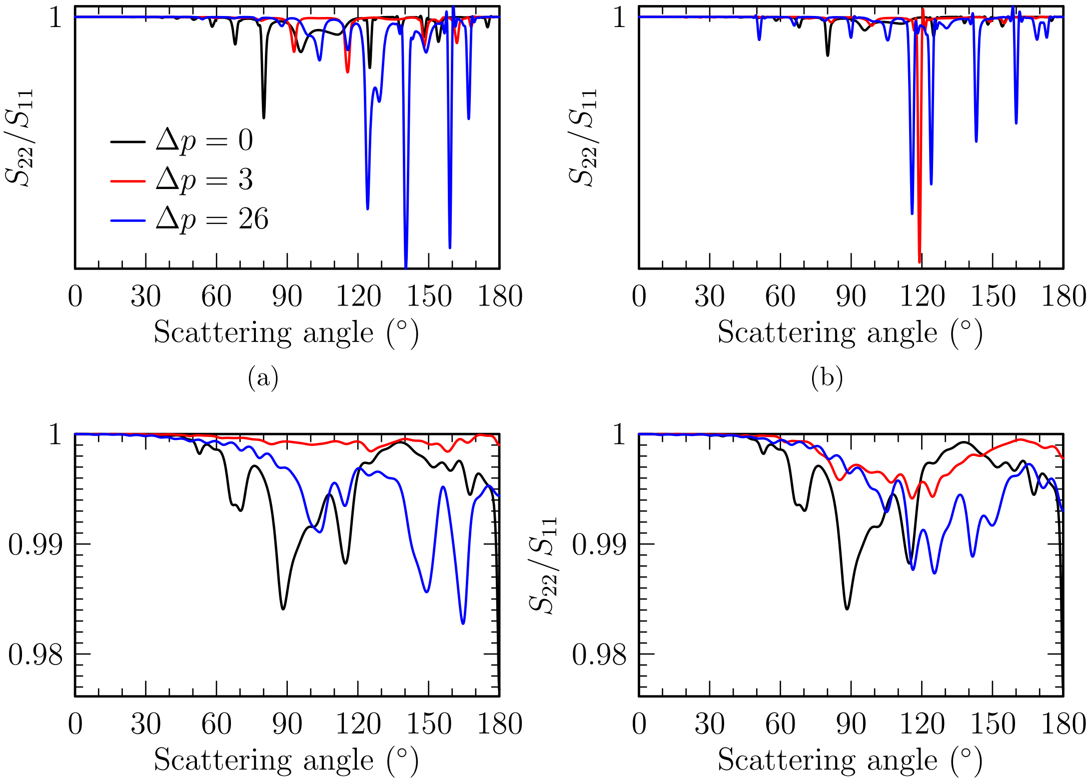

(a) (b) (c) (d)

Figure 30: S_{22}/S_{11} averaged over the azimuthal scattering angle for (a)$\theta_i = 0°$, (b)$\theta_i = 180°$, (c)$\theta_i = 30°$, and (d)$\theta_i = 150°$ for $\Delta p = 0, 3, 26$.

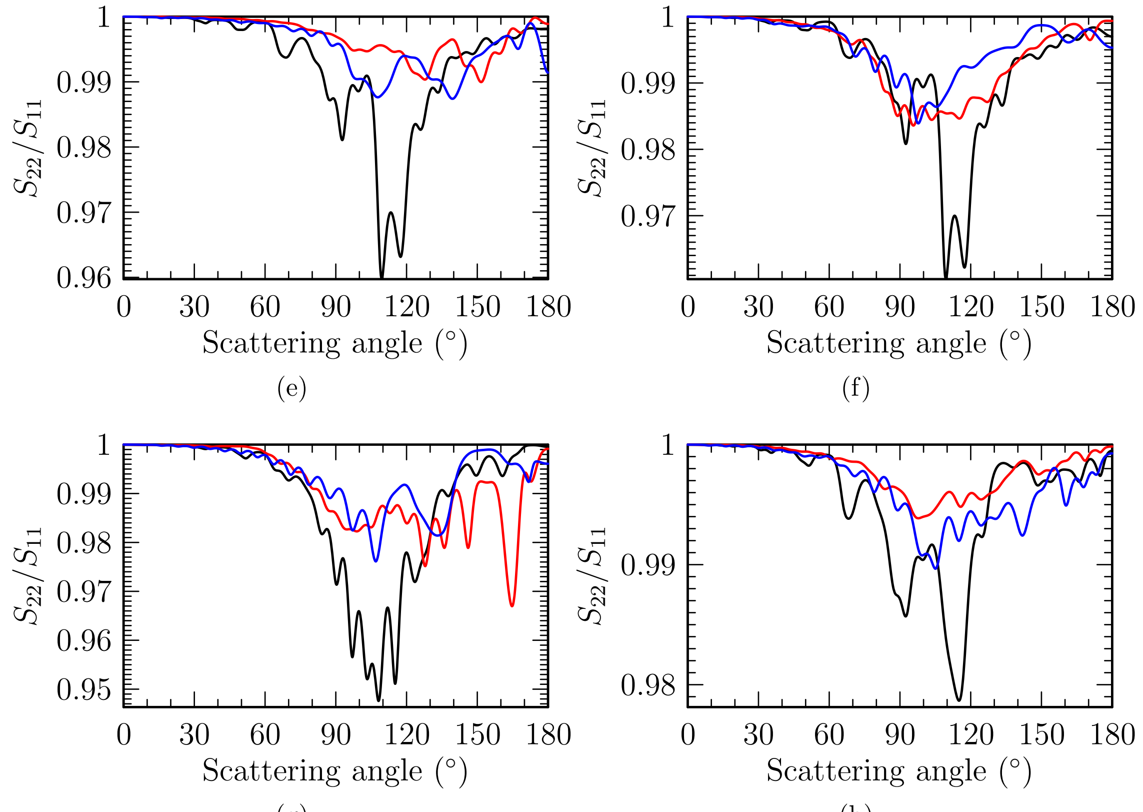

(e)

(f)

(g)

(h)

Figure 30: S_{22}/S_{11} averaged over the azimuthal scattering angle for (e)$\theta_i = 60°$, (f)$\theta_i = 120°$, (g)$\theta_i = 150°$, and (h)averaged over all θ_i for $\Delta p = 0, 3, 26$.

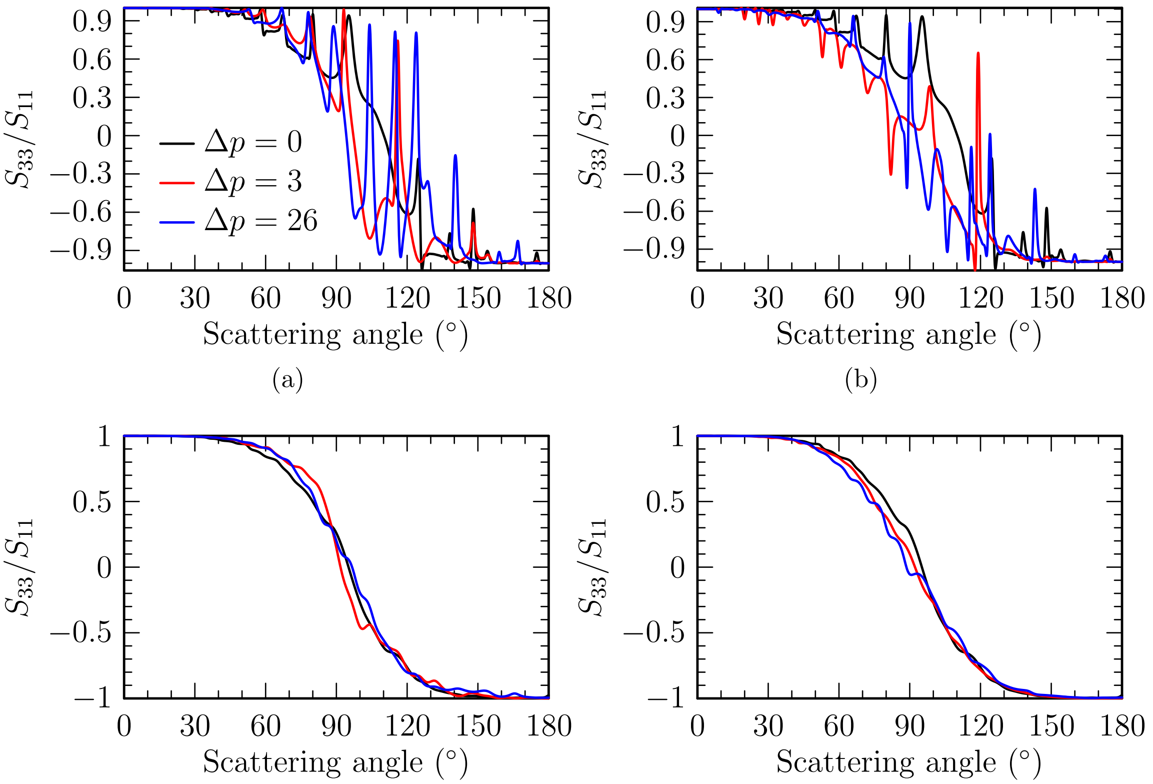

(a) (b)

(c) (d)

Figure 31: S_{33}/S_{11} averaged over the azimuthal scattering angle for (a)$\theta_i = 0°$, (b)$\theta_i = 180°$, (c)$\theta_i = 30°$, and (d)$\theta_i = 150°$ for $\Delta p = 0, 3, 26$.

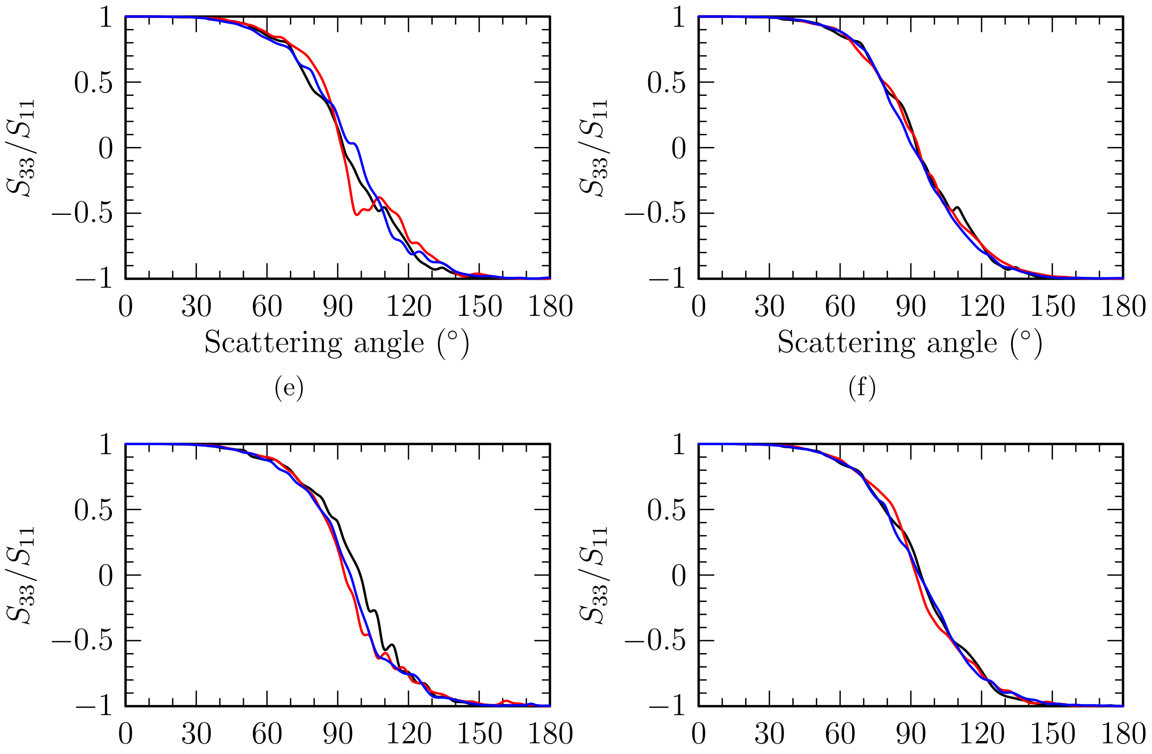

(e)

(f)

(g)

(h)

Figure 31: S_{33}/S_{11} averaged over the azimuthal scattering angle for (e)$\theta_i = 60°$, (f)$\theta_i = 120°$, (g)$\theta_i = 150°$, and (h)averaged over all θ_i for $\Delta p = 0, 3, 26$.

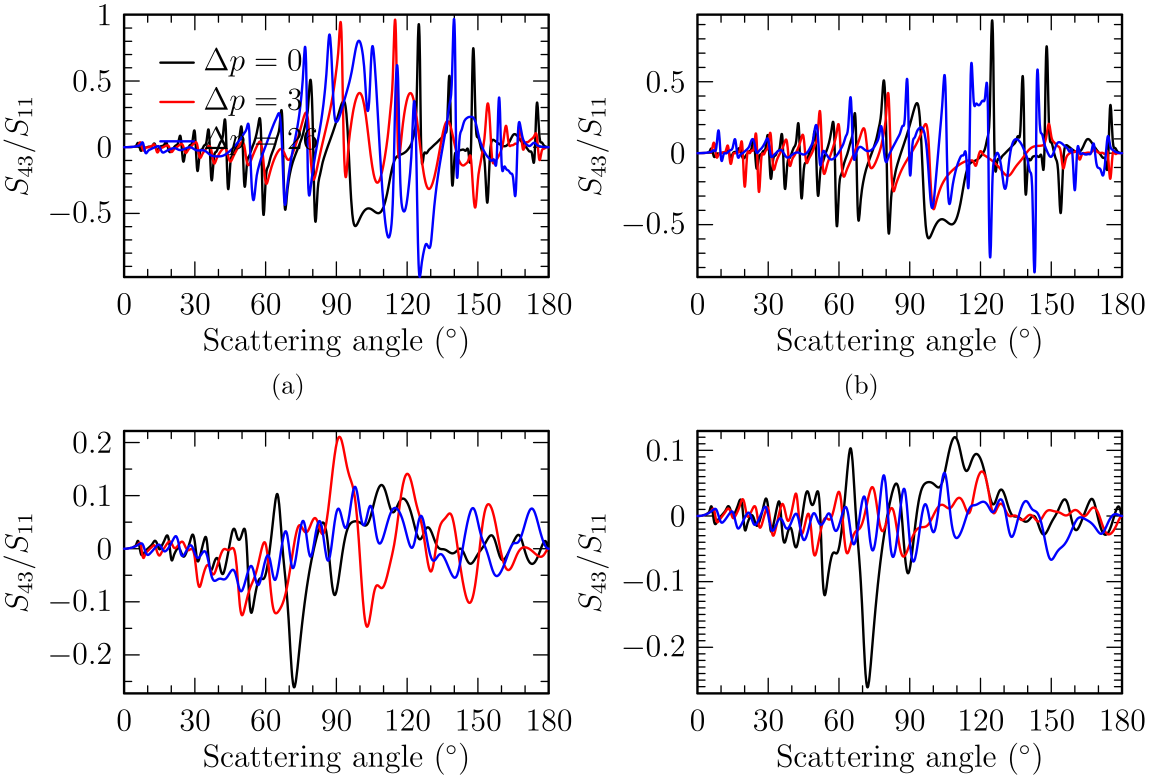

(a) (b) (c) (d)

Figure 32: S_{43}/S_{11} averaged over the azimuthal scattering angle for (a)$\theta_i = 0°$, (b)$\theta_i = 180°$, (c)$\theta_i = 30°$, and (d)$\theta_i = 150°$ for $\Delta p = 0, 3, 26$.

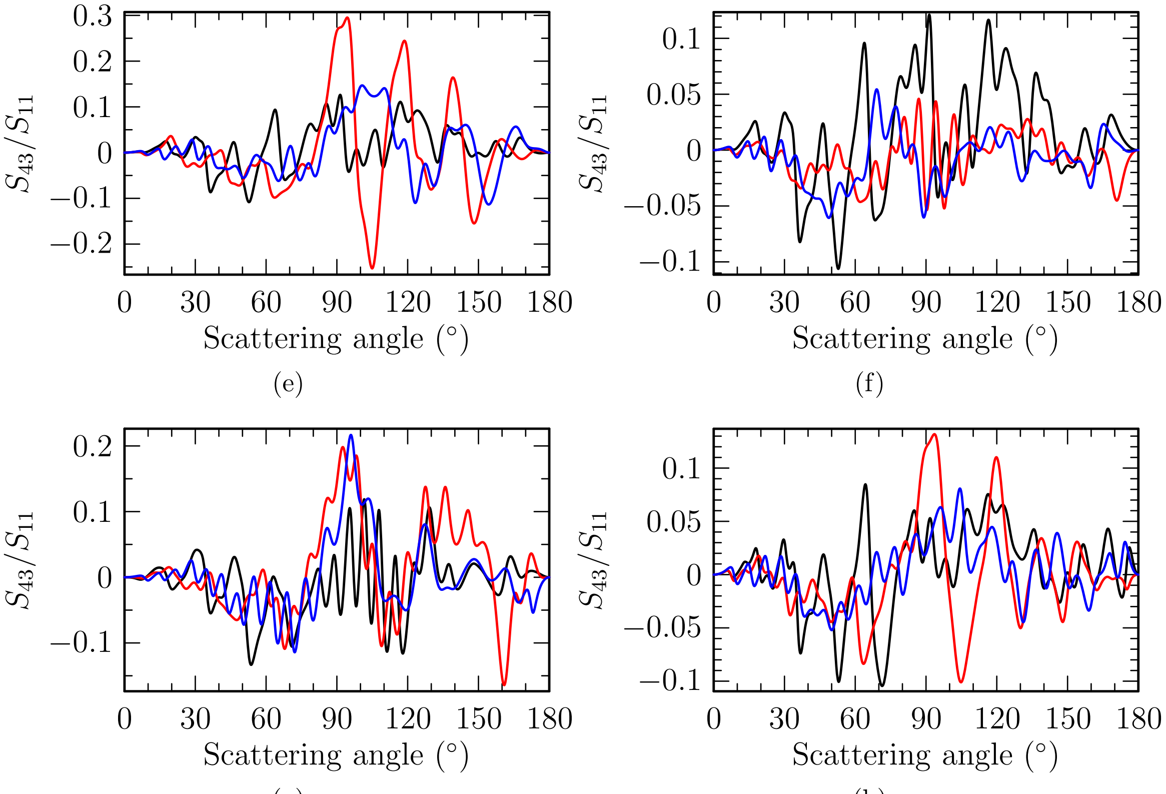

(e) (f) (g) (h)

Figure 32: S_{43}/S_{11} averaged over the azimuthal scattering angle for (e)$\theta_i = 60°$, (f)$\theta_i = 120°$, (g)$\theta_i = 150°$, and (h)averaged over all θ_i for $\Delta p = 0, 3, 26$.

the azimuthal angle with $\Delta p = 0, 3, 26$ and for incident field angles of $\theta_{=}0°$, 30°, 90°, 150°, 180° and $\phi_i = 0$ along with the result averaged over the incident angles. For $\theta_i = 0°, 180°$, the differing pressure gradients are clearly distinguishable, with the exception of S_{22}; however, for the other angles, there is no clear dependence on the pressure gradient. For S_{22}, the converse is true, i.e., the pressure gradients are distinguishable for all angles except $\theta = 0°, 180°$. These figures show that if the orientation is known, there is sufficient information to differentiate the various pressure gradients just as in the two-dimensional S_{11} figures. Unlike simulated models, it is impractical to collect scattering data over the entire range of scattering angles in laboratory testing. Also, determining the orientation of the RBC can be problematic in the laboratory. Thus, the data of figures 28–32 which is averaged over the incident field angles is the best candidate for practical use. This average behavior shows little dependence on the pressure gradient, with the exception of S_{12} and S_{34}.

Fig. 28 also gives evidence that the oscillations of S_{11} are related to the symmetry of the particle. For $\theta = 0°, 180°$, the RBC profile with respect to the incident field is symmetric, and the characteristic oscillations are pronounced in the related figures. For the other angles, where the profile is not symmetric, the oscillations are less pronounced.

Chapter 9: NALM6 cells

9.1 Introduction

NALM6 cells are human B-cell precursors derived from the peripheral blood of a patient with acute lymphoblastic leukemia[22]. B-cells are important biologically due to their role in the immune system, part of which is to secrete antibodies in response to invading microbes such as viruses or bacteria. B-cell comprise 10%–20% of the lymphocyte population. Unactivated B-cells have a spherical shape with diameters ranging from $6\mu m$–$9\mu m$ and a nuclei with diameters ranging from $5\mu m$–$8\mu m$[42]. Activated B-cells, those en route to form plasma cells, are larger, having diameters ranging from $9\mu m$–$15\mu m$. These cells are larger due primarily to a greater amount of cytoplasm.

For simulation, the NALM6 cells are modeled as two media, one corresponding to the nucleus and the other to cytoplasm. These models are created from confocal images using the process described in the next section to convert the confocal images to domain images and then using the process described in §6 to create the model. Once created, the models are assigned various refractive index values depending on the purpose of the particular simulation.

9.2 Image acquisition and processing

To prepare the cells for imaging, they are stained with two dyes. The first dye, FM 1-43 at $4\mu M$, is absorbed by the cell membrane. The second dye, SYTO 61 at $5\mu M$, is absorbed by the nucleus. FM 1-43 and SYTO 61 are excited at wavelengths of $488nm$ and $633nm$ respectively. After staining, the cells are washed to remove excess dye and placed in a depression slide. The imaging was done with a scanning confocal microscope, the Zeiss LSM 510, using both a $488nm$ and a $633nm$ laser. The fluorescence data was obtained on two independent channels corresponding to the response of the two dyes. The images obtained are $512pixels \times 512pixels$ with each pixel having an area of $0.04\mu m \times 0.04\mu m$. The separation between images is $0.51\mu m$. The images obtained for one of the cells, called cell #8, are shown in Fig. 33. In the figure, the red indicates the response from SYTO 61, while the green indicates the response of FM 1-43. The responses are scaled to an integer value between 0 and 255, with a higher integer corresponding to a higher intensity. Analysis of the data revealed that the green intensities were saturated in many of the pixels, i.e., the intensity was

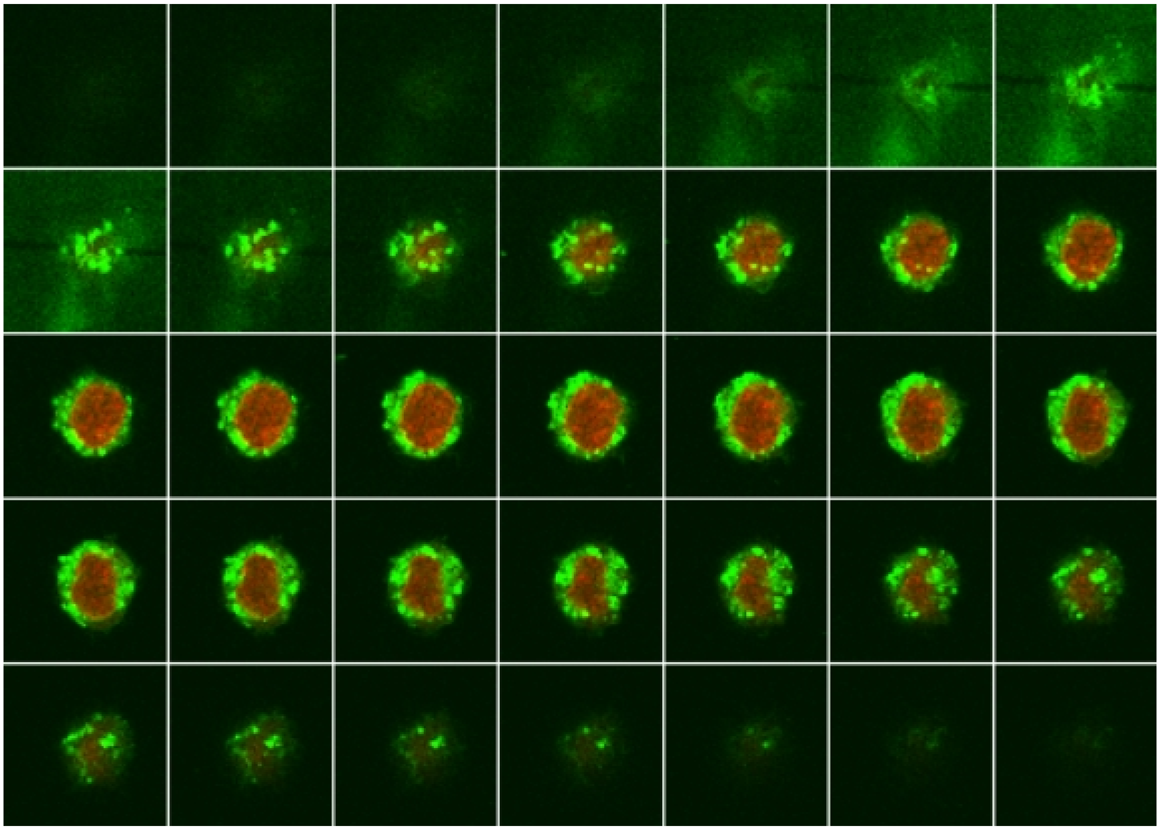

Figure 33: The set of confocal images for a cell #8. The green color indicates the response of the FM 1-43 dye and the red indicates the response of the SYTO 61 dye.

higher than that associated with 255, and 255 is used. This makes the information impractical for use in determining the domains; however, it was also determined that the red data contained sufficient information to determine the nucleus and cytoplasm domains. Fig. 34 shows only the red portion of the slide. In the image three distinct intensity groups can be identified. The lowest intensity group corresponds to the background, the medium intensity group to the cytoplasm, and the highest intensity group to the nucleus. Thus, using the red data, the domains can be identified.

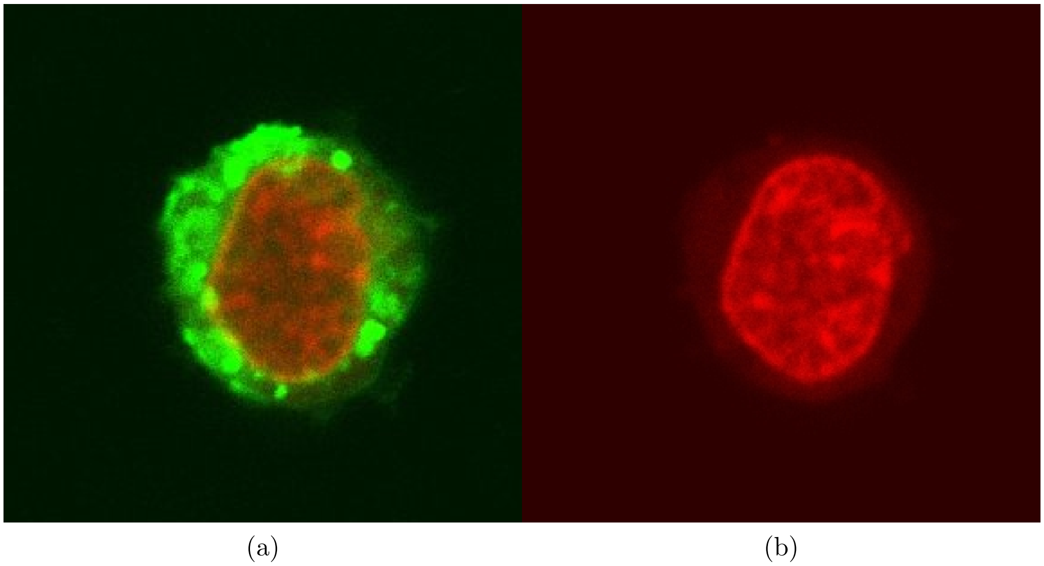

Figure 34: (a)The original confocal image and (b)the same image showing only the red data. Using on the red data, three domains can be identified; the background, the cytoplasm, and the nucleus.

The process of converting the confocal images to domain images begins by identifying the center of the cell. This is done by taking the first moment of intensity scaled by the inverse of the total of all intensity values. Next, a histogram of the intensity values for the slide closest to the center is taken. Fig. 35 shows the histogram for the image of Fig. 34. Three peaks can be identified, corresponding to the background, cytoplasm, and nucleus. Using the histogram, threshold values, intensity values which separate the groups, are chosen. Next, two new sets of raster data are created with the same size as that of the red data; these new sets will be referred to as the domain sets. For the first domain set, all pixels belonging to the cytoplasm or nucleus groups, according to the histogram, are given a value of one; and the remaining pixels are given a zero value. For the second domain set, all pixels belonging to the nucleus group are given a value of one; and the remaining pixels are given a zero value. Then for each domain set, the single pixel specks are removed. This is done by comparing the value of each pixel, to that of all of the pixel's neighboring pixel values. If all of the neighboring values are equal to each other and different from the pixel value, then the pixel value is changed to that of its neighbors. The domain sets are then "smoothed" using a window average with a two-dimensional Gaussian kernel. After the smoothing, a threshold value is used to set all pixels to a value of zero or one. The next step is to identify clusters in each of the domain sets. A cluster is a set of pixels sharing the same value for which any pixel is "connected" to every other pixel by pixels of the same value, i.e., if pixel 1 and neighboring pixel 2 have the same value; and pixel 2 and its neighboring pixel 8 have the same value, then pixel 1 and pixel 8 are in the same cluster. Each cluster is given a unique value, and all pixels of a cluster are assigned this value. The cluster containing the upper left corner of the image is given a value of zero and is assumed to be part of the background. Finally, using the domain sets with the cluster values, a new image is created with pixels which have a green intensity value of 255, if the corresponding cytoplasm domain set pixel is not part of the background cluster; and a red intensity value of 255, if the corresponding nucleus domain set pixel is not part of the background cluster. All remaining pixels are given green and red intensity values of 0. Fig. 36 shows the resultant image of this process with the red image from Fig. 34 for comparison. The green area corresponds to the cytoplasm and the yellow to the nucleus. The processed images can be used to construct the model function as described in §6.3.

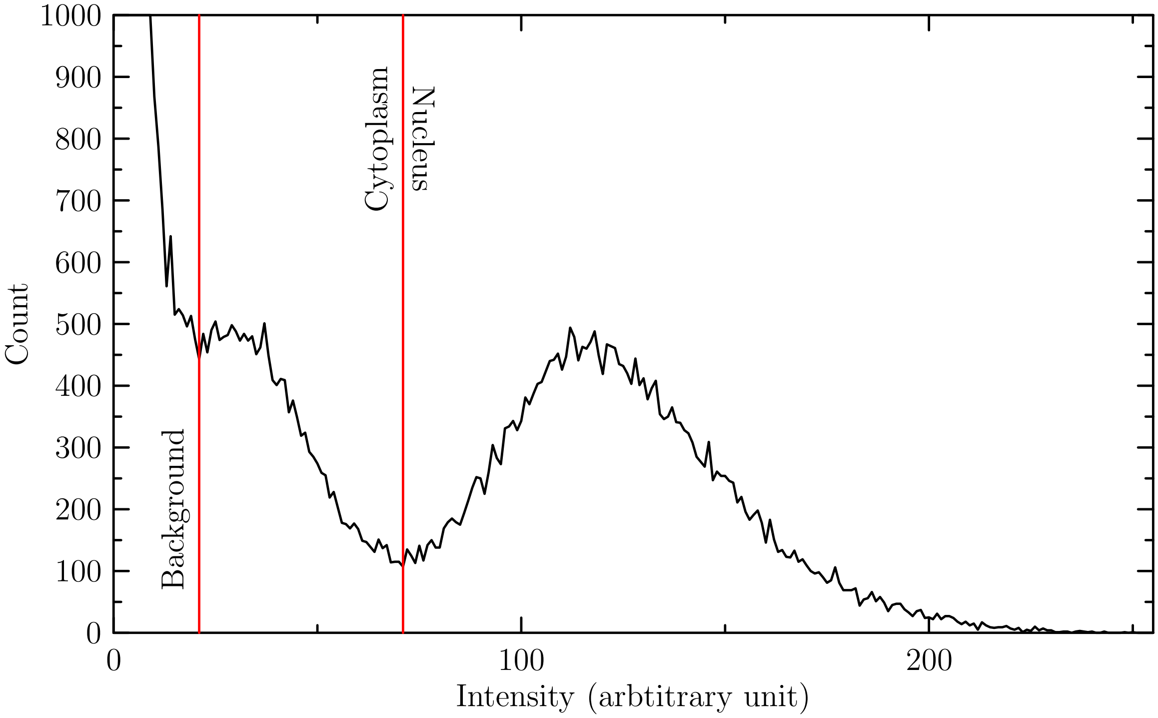

Figure 35: The histogram for the data of the image in Fig. 34(b)

Seven cell models were created by this process and are shown in Fig. 37. The surfaces are transparent, allowing the nucleus to be seen. Note that the images are not on a particular scale and that the models have different sizes. The volumes of the models range from $445.46\mu m^3$, for cell #1, to $737.33\mu m^3$, for cell #9.

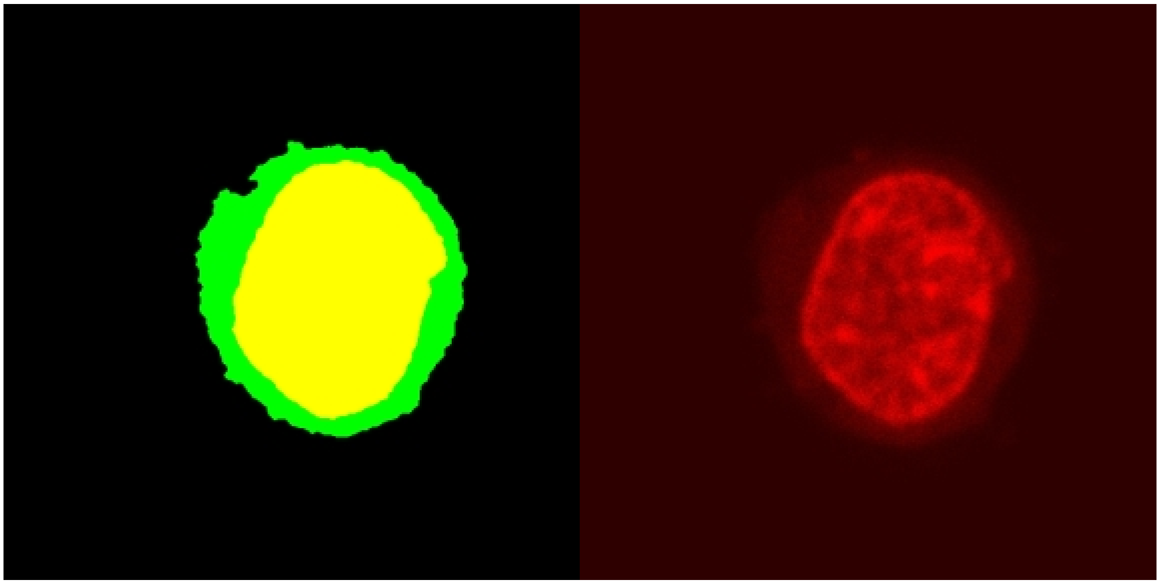
(a) (b)

Figure 36: After processing the confocal image (b), a domain image (a) is produced. The domain image contains only the domain information; the intensity data is not included.

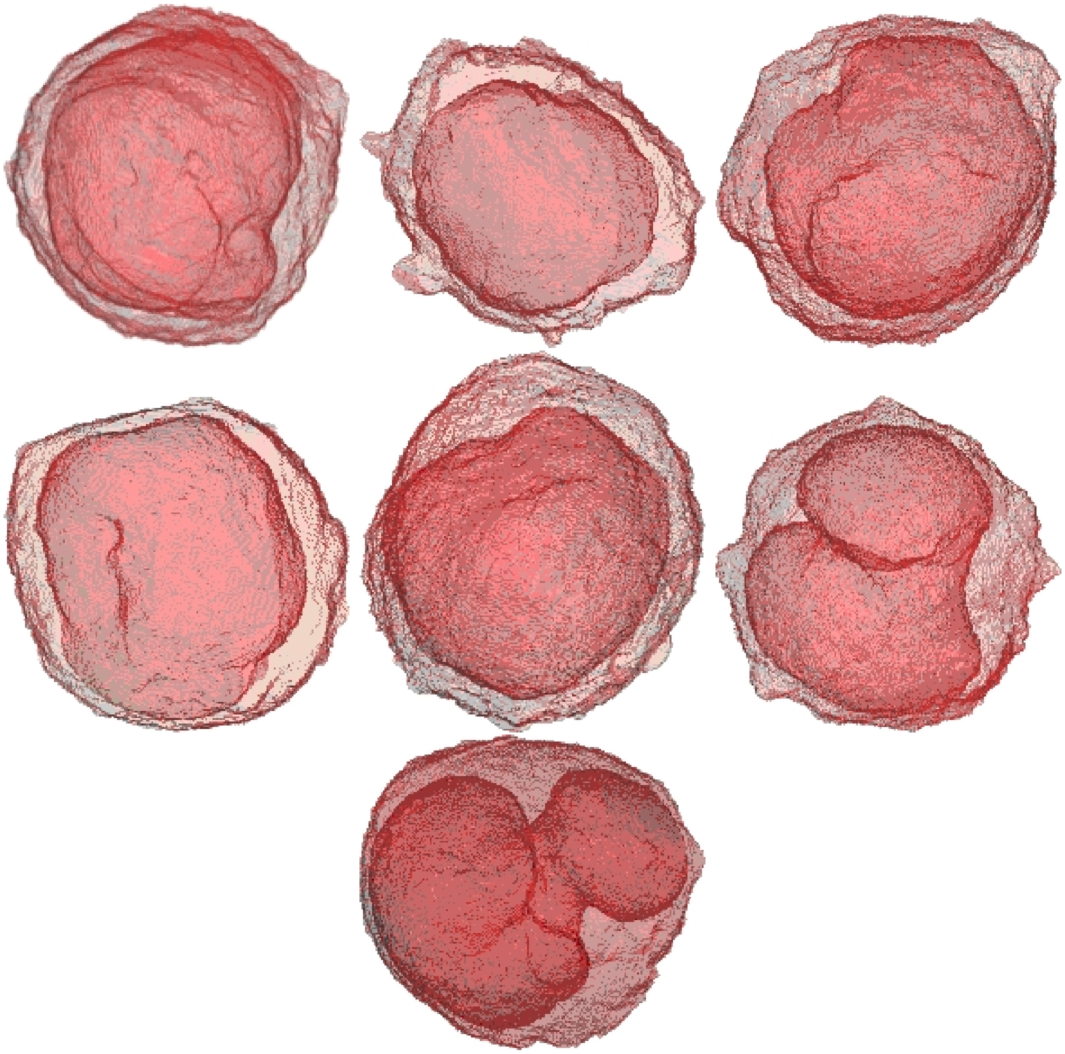

Figure 37: The confocal models for cell #s 1–10. The surfaces are transparent allowing the model nucleus to be seen. The images are not on a particular scale; the smallest model, cell #1, has a volume of $445.46\mu m^3$, while the largest, cell #9, has a volume of $737.33\mu m^3$.

9.3 Validation of models constructed from confocal images

After constructing some cell models from confocal images, it was found that the models were distorted due to optical distortions introduced in the image acquisition process. This distortion results in stretching along the z-axis, causing the models to appear elongated. In order to mitigate the deformation, model construction for polystyrene spheres of known diameter were produced according to the procedures described in §6.3 and §9.2. Commercially available spheres with a $6\mu m$ diameter that are coated with a fluorescent dye were used for this purpose. Confocal images of a sphere were acquired, shown in Fig. 38, under similar conditions to those in which the NALM6 images were obtained. The images were processed and the sphere model was constructed with the processed images. To partially offset the distortion introduced in image acquisition, the distance between the images was scaled to produce a nearly spherical shape. The sphere model as seen from three different viewpoints is shown in Fig. 39. It can be seen from Fig. 39 that the sphere model is not perfectly spherical. Two causes for this are the distortions introduced in the image acquisition and errors introduced by the interpolation procedure. The scaling factor obtained via this process is used to scale the images for biological cell as well.

To see how much the difference from a perfectly spherical shape affects the scattering pattern, the scattering phase function for the sphere model was calculated using the FDTD method. The S_{11} matrix element for three angles of incidence along with the average result is compared with that obtained from Mie theory for the scattering from an ideal sphere of the same radius, $3\mu m$, in Fig. 40. The simulations used an incident wave of wavelength $\lambda = 1\mu m$ in vacuum and a complex refractive index for the sphere of $n = 1.3675 + i1.0x10^{-5}$ in a host medium of refractive index of $n_h = 1.35$.

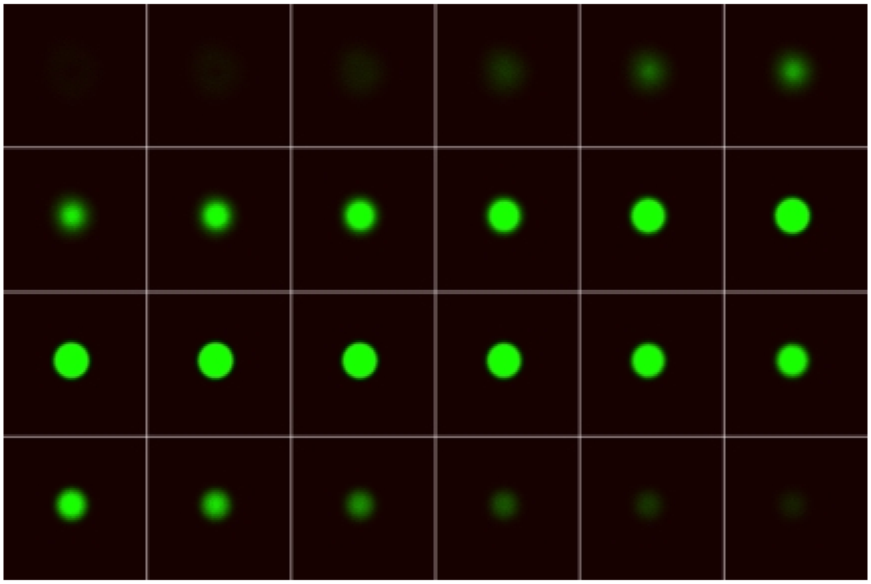

Figure 38: The confocal images for a $6\mu m$ diameter sphere.

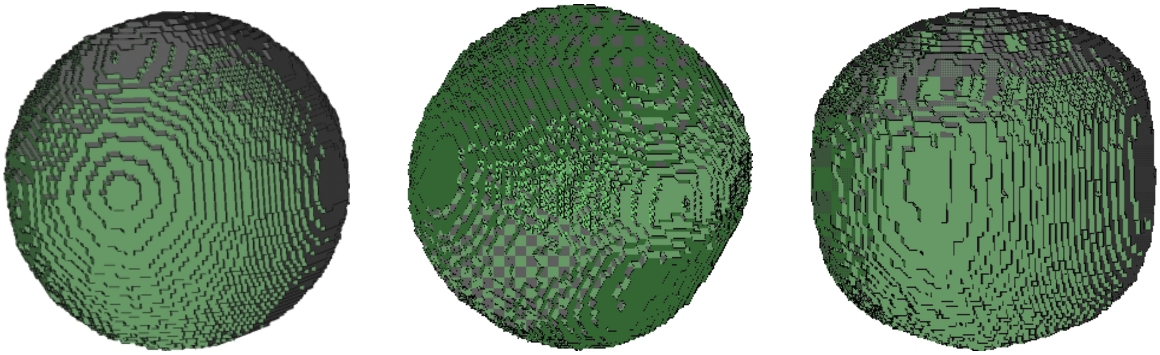

Figure 39: The confocal sphere model from three different viewpoints.

The FDTD grid cell size was set at $\Delta = \lambda_h/30$ with λ_h as the wavelength of the incident light in the host medium. It can be seen from Fig. 40 that the results vary depending on the angle of incidence. The sphere was oriented such that at incident angle $(\theta = 0, \phi = 0)$, the profile with respect to the incident wavefront is symmetric, i.e., a circular shadow would be cast. Like the RBC data, this gives evidence to the fact that the oscillations present in S_{11} are related to the symmetry of the particle. These results demonstrate that the overall trend in the angular distribution of the scattered light remains similar between the sphere model and a perfect sphere generated mathematically. The difference in the oscillation amplitudes can be attributed to shape deformations inherent in the image acquisition and interpolation errors during the model construction process. The characteristic oscillations in the scattering phase function of a sphere are the direct consequence of the spherical symmetry of the shape; thus, this feature is very sensitive to any departure from this symmetry. A slight deformation introduced by the imperfect imaging and construction processes is expected to cause observable changes in the details of the scattering pattern.

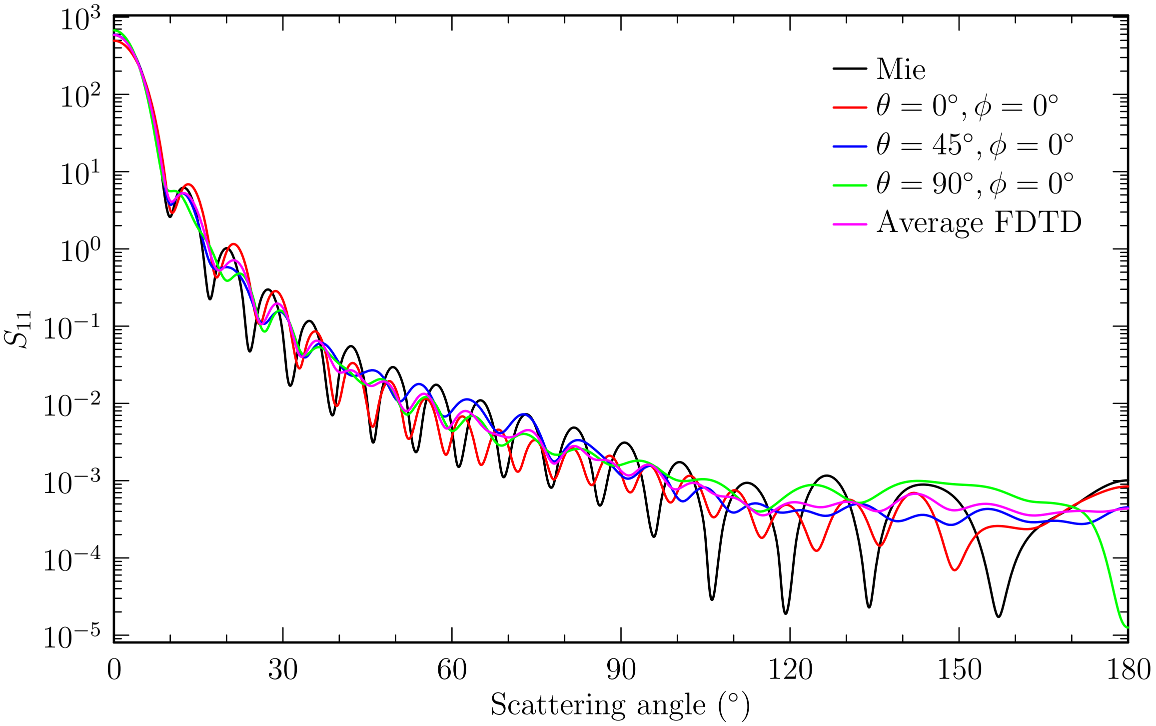

Figure 40: A comparison of the scattering from a perfect sphere and the sphere model obtained from confocal images.

In contrast, biological cells posses very little symmetry in their structures due to their nonspherical shape, irregularities in the surface, and the heterogeneity of the intracellular components. Thus, it is reasonable to expect that the imaging and model construction errors observed in the case of the sphere should have much less impact on the distributions of light scattered by cells. For example, the amplitude of the cell membrane roughness, due to bending and folding, and other nonspherical features in the shape of a typical B-cell observed by electron microscope[42] is typically larger than the imaging and model construction errors of $0.3\mu m$ or less. Therefore, it is much less likely in these cases than in the case of the sphere that such errors will cause significant change in the light scattering patterns. It should be pointed out that further improvement over the present work, which represents a first step in constructing realistic 3D biological cell models for optical simulations, can be achieved by refining the cell preparation, the image acquisition processes, and improving the interpolation procedure.

9.4 Overview of the simulations

All of the cell model simulations discussed use the FDTD program prior to the dispersion correction, unless otherwise noted. To mitigate the effect of numerical errors in comparing simulation results, all of the FDTD simulations discussed use identical numerical parameters, i.e., those parameters not related to the physical system, such as PML parameters. A PML layer of eight cells is used; preliminary studies showed that this is sufficient. The number of cells between the smallest cuboid, aligned with the grid axis, containing the cell model and the TF/SF boundary, see §3.2, is five. The space between the TF/SF boundary and the inner PML boundary is eight cells thick.

In addition, a common set of physical parameters is also used. The refractive indices used for most of the simulations are 1.3500 for the host medium, $1.3675 + i1.5 \times 10^{-5}$ for the cytoplasm, and $1.4000 + i1.5 \times 10^{-5}$ for the nucleus. The purpose of some of the simulations is to determine the effect of the refractive index on the result. For these simulations the various refractive indices will be given in the discussion.

The angles of incidence used are also the same for all simulations. The set of twelve incident angles used are

$$\begin{aligned} \left\{(\theta_i,\phi_i)\middle|\,(\theta_i,\phi_i)\in\{\right.&(28^\circ,13^\circ),(40^\circ,236^\circ),(45^\circ,135^\circ),(72^\circ,306^\circ),\\ &(77^\circ,70^\circ),(88^\circ,187^\circ),(93^\circ,7^\circ),(102^\circ,250^\circ),\,,\\ &\left.(107^\circ,126^\circ),(135^\circ,315^\circ),(139^\circ,56^\circ),(151^\circ,193^\circ)\}\right\} \end{aligned} \tag{9.1}$$

where θ_i and ϕ_i are the polar and azimuthal angles with respect to the z-axis of the FDTD grid, respectively. These angles were chosen to reduce proximity bias in the results. Fig. 41 depicts the solid angle division among the incident angles. The equilateral spherical pentagons represent the areas associated with the incident angles,

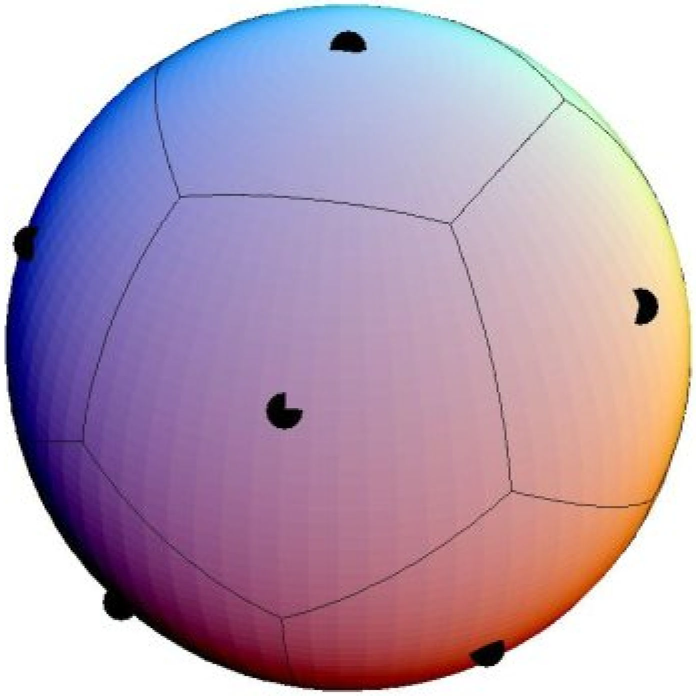

Figure 41: The incident angles used in the simulations are associated with equal portions of the solid angle. These portions are shown by the pentagonal tiling. At the center of each pentagon is a point where a ray at one of the incident angles intersects the sphere.

while the points marked at the geometric center of the pentagons show where rays at the incident angles intersect the sphere. Using this association, the results for each incident angle represent an equal portion of the solid angle, and the distance between any two neighboring angles is equal. Note that there are five such equilateral polygonal tilings; specifically, tilings consisting of four, six, eight, twelve, and twenty polygons. Preliminary testing showed negligible differences between the average results for the twenty angles and twelve angles and significant differences between those of eight and twelve angles. Table 14 shows c_{ext} and g for these tests. Although g remains almost the same, the percentage difference between the eight and twelve angle c_{ext} results is 4.62%, while that between the twelve and twenty angle c_{ext} results is 0.424%. The incident field used in the simulations is a plane wave and approximates

Table 14: Average c_{ext} and average g for 8, 12, and 20 incident angles

no. of angles	c_{ext}	g
8	4.1920	0.9873
12	4.0067	0.9874
20	3.9898	0.9873

a Gaussian pulse. The mean frequency of the pulse is the wavelength of interest. The half-width of the pulse is equal in all simulations and is chosen to be as small as possible to reduce the simulation time while maintaining numerical stability.

The grid discretization, Δ, and the CFL factor are $\lambda/30$ and 0.98 respectively. Preliminary testing showed that $\Delta = \lambda/30$ allows for accurate results within a reasonable simulation time. The ideal CFL factor is 1, and 0.98 was chosen to ensure numerical stability while not significantly increasing the simulation time.

9.5 Volume dependence

To test the dependence of light scattering on the shape of the scattering particle, scattering by the cell models is compared to scattering by sphere models. Two different sphere models are used, the coated sphere and the equivalent sphere. The coated sphere consists of concentric spheres, with the inner sphere having the same volume and refractive index as the nucleus of the cell model. The outer sphere has the volume of the entire cell model, and the region between the sphere surfaces is given the same refractive index as the cytoplasm of the cell model. The equivalent sphere has the same volume as the entire cell model and a refractive index that is the average of the two refractive indices weighted by the respective volumes. The scattering result for the cell models are obtained via the FDTD simulation. The sphere model results are obtained from the program, DMILAY, by Toon and Ackerman which uses Mie theory to calculate the result[43].

Fig. 42 shows S_{11}, averaged over the azimuthal scattering angle, for the confocal models and the sphere models, for all seven of the cells. For the confocal models, the result shown is an average result for all of the incident angles listed in the previous section. In each case, there is little difference between the various models for $\theta < 5°$. This indicates that S_{11} at small scattering angles, $< 5°$, is affected primarily by the volume and refractive index and not by structural details[6]. This phenomenon has also been reported in experimental studies of light scattering by biological cells[35]. For $5° < \theta < 20°$, the coated sphere results and the confocal model results continue to have little difference, while the equivalent sphere results show more oscillation. This indicates that in this region, factors other than the volume and refractive index contribute significantly to the scattering. The fact that the coated sphere and the confocal model both contain a nucleus that the equivalent sphere lacks is evidence that structural features affect the scattering in this region. Further, since the confocal model and coated sphere nuclei differ in small-scale properties, such as surface features, the scattering in this region is affected primarily by the large-scale properties, such as volume. At angles greater than 20°, both results from both types of sphere models exhibit a larger amplitude of oscillation than that of the confocal models. This is characteristic of the symmetries present in the sphere models. These differences indicate that small-scale features also influence the scattering in this region[6]. The differences between the results become progressively more pronounced with increasing angle, which indicates that the influence of both large and small structural features increases as the scattering angle increases.

Fig. 43 shows the confocal results for cell #8 at each of the incident angles along with the results of the sphere models, which are the same at all angles. The cell #8 model's "optical profile" is different when viewed from the various incident angles, thus a different scattering pattern is expected. Although the scattering patterns are different, the small difference in the results for $\theta < 20^\circ$ at the various incident angles lends further support to the conclusion that the scattering in this region is influenced primarily by the volume and refractive index. Fig. 44 shows the confocal results for cell #10 and the results of the associated sphere models. Although cell #8 and cell #10 have nuclei with quite different shapes, see Fig. 37, the same conclusions can be drawn from the cell #10 results. Comparison of each of the other five cell models with their respective sphere model results are analogous to those of the cell #8 and cell #10 models. Other comparisons to the sphere models can be made using the S_{12}, S_{33}, and S_{43} elements. Fig. 9.5 shows the results for cell #8 and the associated sphere models. The cell #8 result follows the same general trend as those of the sphere models; however, it lacks the characteristic oscillations of the sphere models. For the S_{12} and S_{33} elements this indicates that the large scale properties are the primary influence for these elements. For the S_{43} element the magnitude of the cell #8 result is almost flat, making it difficult to draw any conclusions.

Further support for the inflence of the volume on scattering can be seen by comparing the various cell models. Fig. 45 shows the average result for $S_{11}\,(\theta = 0.25°)$ plotted against volume for all of the cell models. Since the refractive index is the same for each of the cell models, these results indicate that the scattering in the forward direction is directly dependent on the volume.

By comparing S_{11} for the various cell models and their associated sphere models, it is clear that the volume is a primary influence on scattering in the forward direction, $\theta < 5°$. Also, comparisons between the cell models and the coated sphere show that large scale properties, such as the presence of a nucleus, affect scattering over a larger range, $\theta < 20°$. However, the equivalent sphere results suggest that the index of refraction also influences scattering in the forward direction, since the equivalent sphere has no nucleus and a different index of refraction.

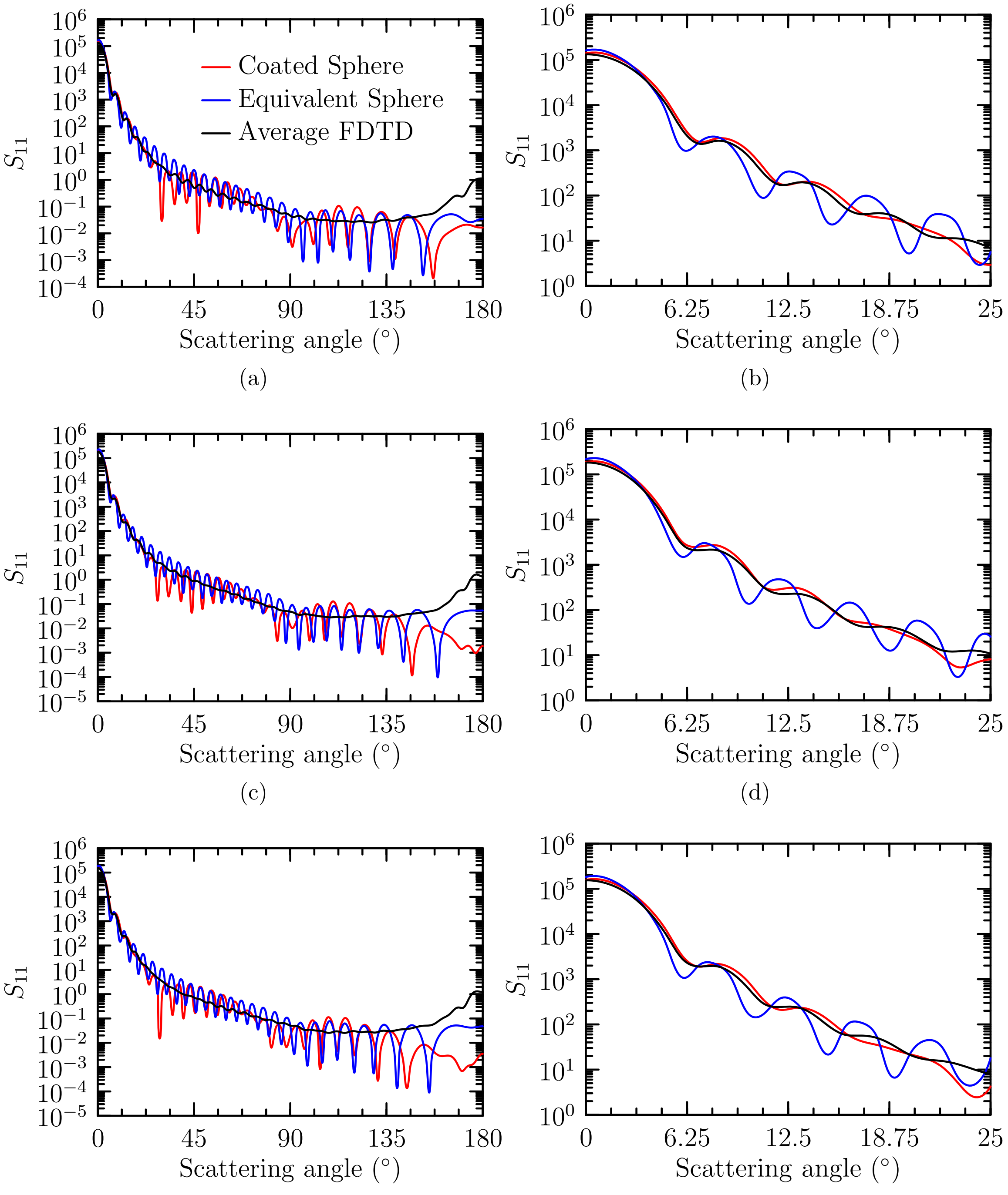

(a) (b)

(c) (d)

(e) (f)

Figure 42: S_{11} of the cell models and the sphere models for (a,b)cell #1, (c,d)cell #2, (e,f)cell #3.

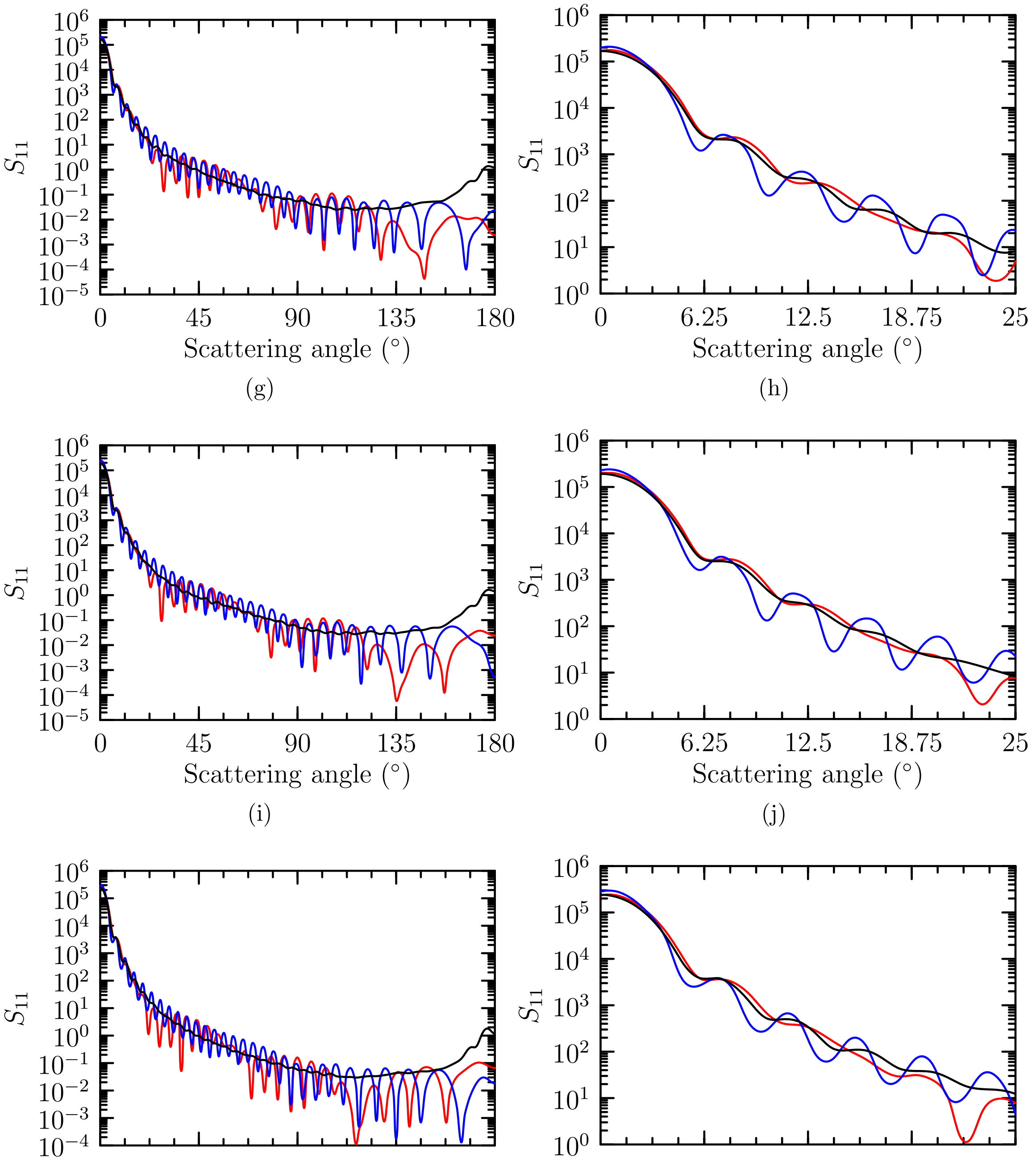

(g) (h)

(i) (j)

(k) (l)

Figure 42: S_{11} of the cell models and the sphere models for (g,h)cell #7, (i,j)cell #8, (k,l)cell #9.

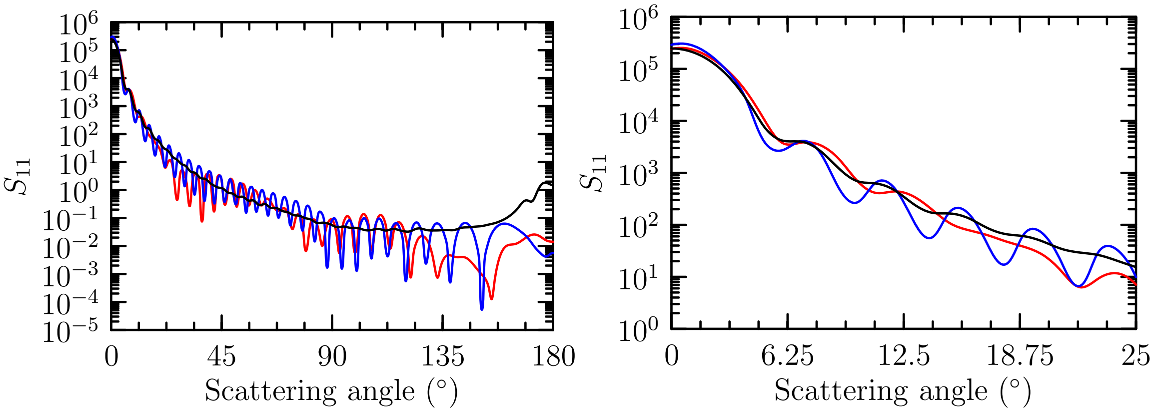

(m)

(n)

Figure 42: S_{11} of the cell models and the sphere models for (m,n)cell #10.

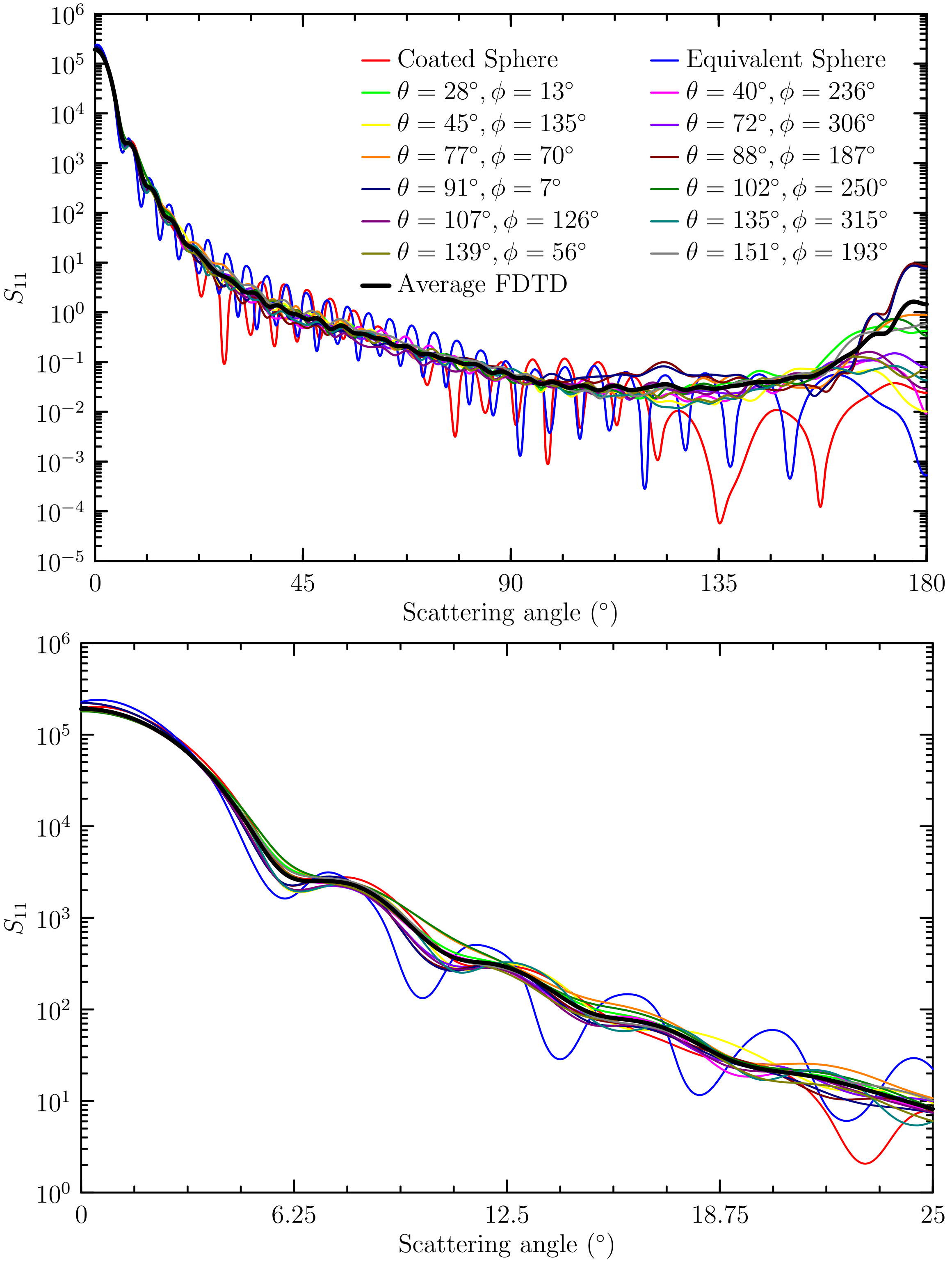

Figure 43: The S_{11} result for the simulations with confocal model and sphere models of cell #8. There is little difference in the results for $\theta < 5°$, while the coated sphere model and the confocal model continue to show little difference up to $\theta \approx 20°$.

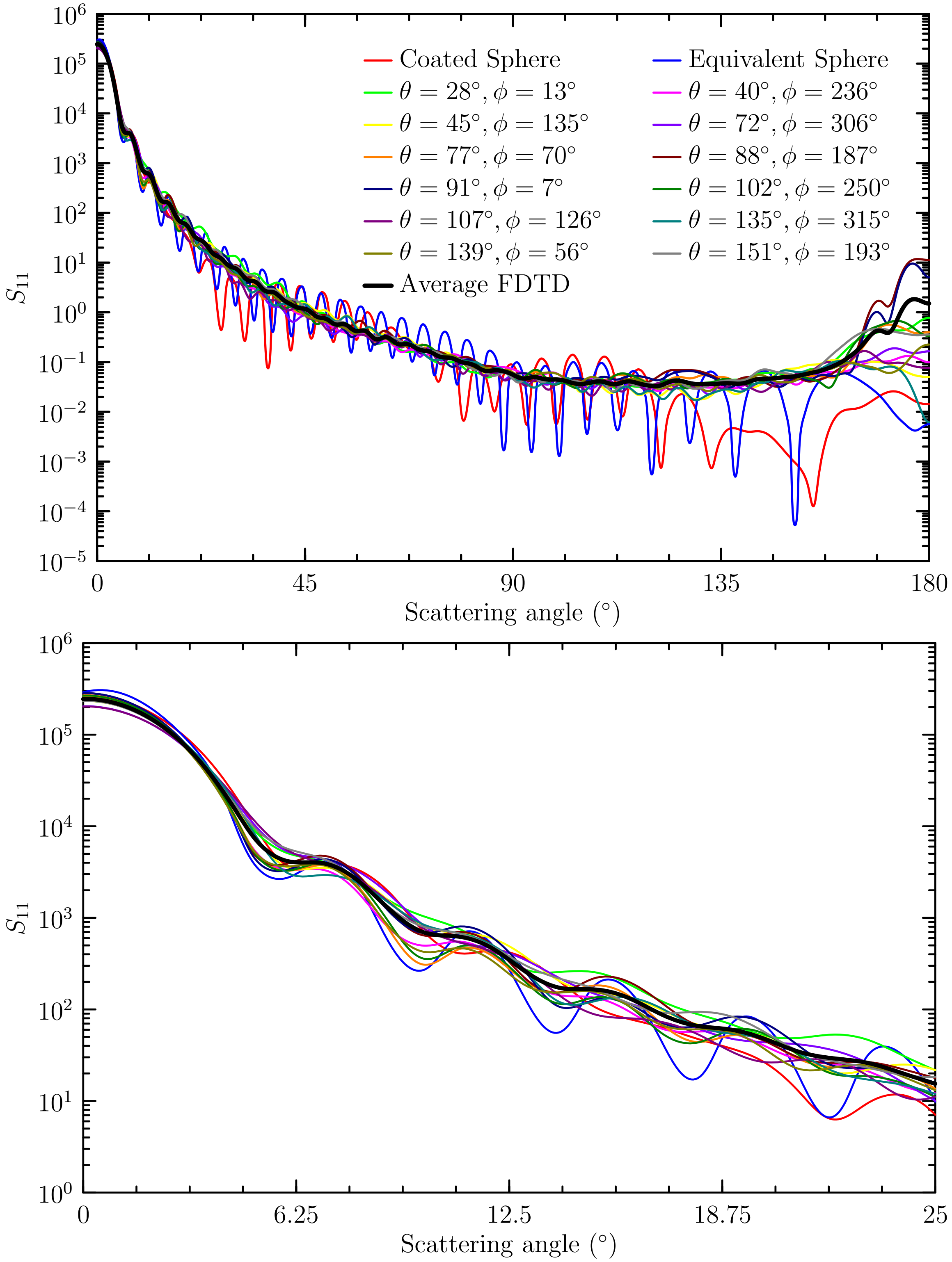

Figure 44: The S_{11} result for the simulations with confocal model and sphere models of cell #10. There is little difference in the results for $\theta < 5°$, while the coated sphere model and the confocal model continue to show little difference up to $\theta \approx 20°$.

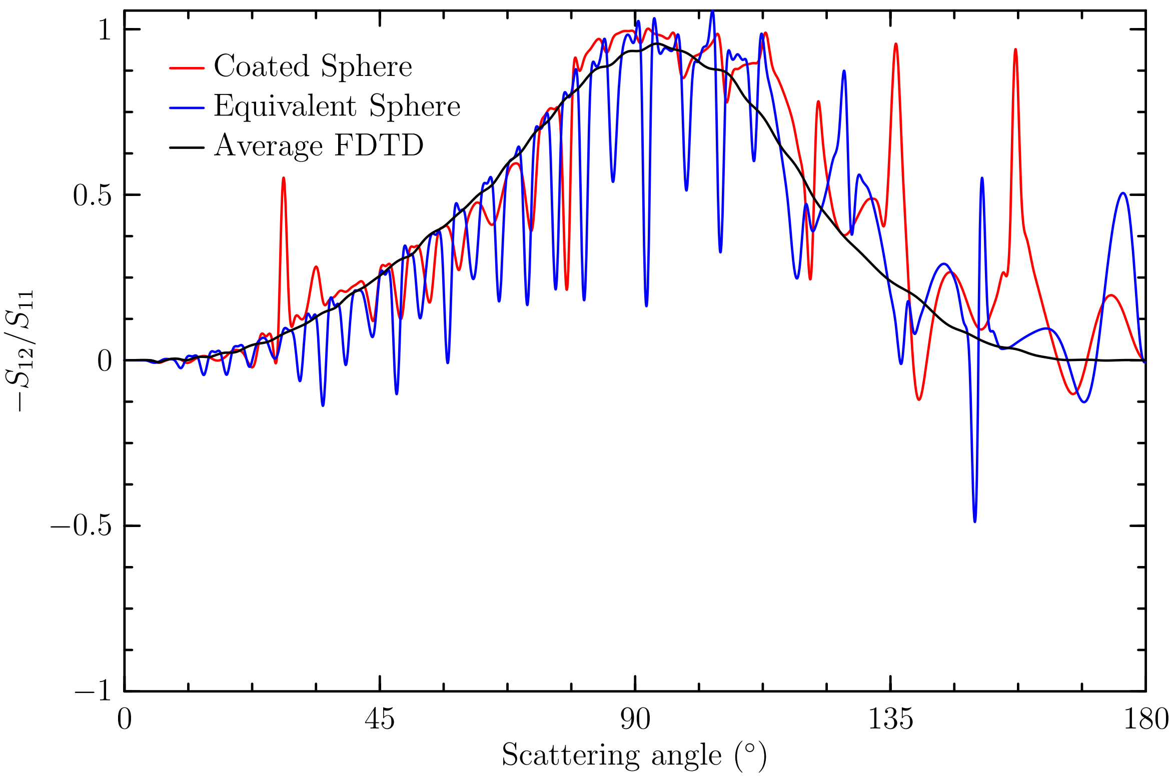
Coated Sphere
Equivalent Sphere
Average FDTD
$-S_{12}/S_{11}$
1
0.5
0
−0.5
−1
0
45
90
135
180
Scattering angle (°)

(a)

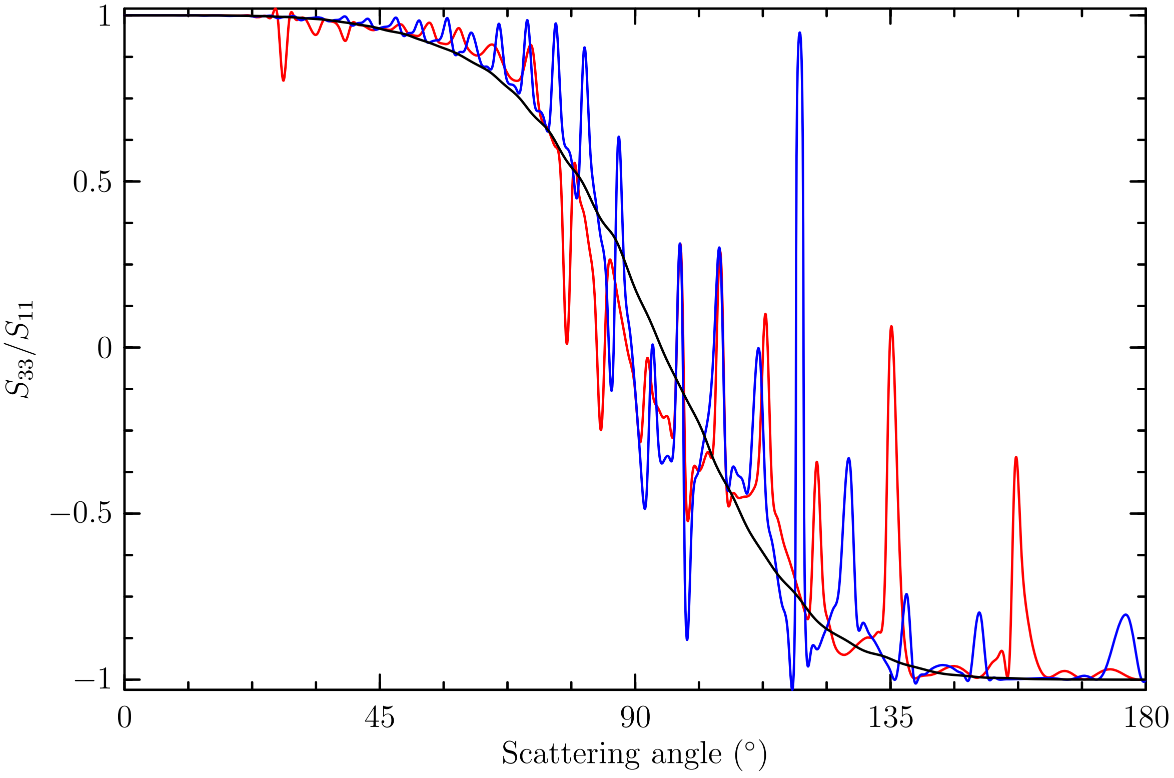
S_{33}/S_{11}
1
0.5
0
−0.5
−1
0
45
90
135
180
Scattering angle (°)

(b)

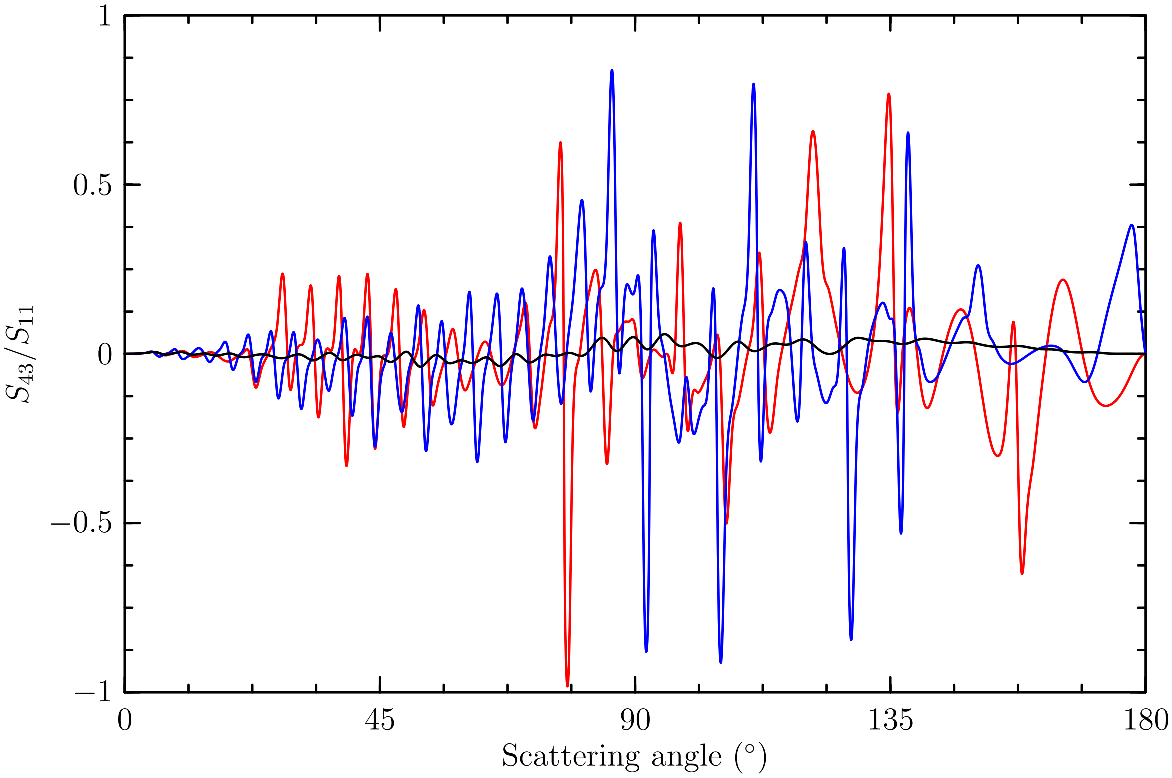

(c)

Figure 44: S_{12}, S_{33}, and S_{43} for the confocal model and sphere models of cell #8. The results in each case have the same general trend; however the confocal model does not show the characteristic oscillations due to symmetry.

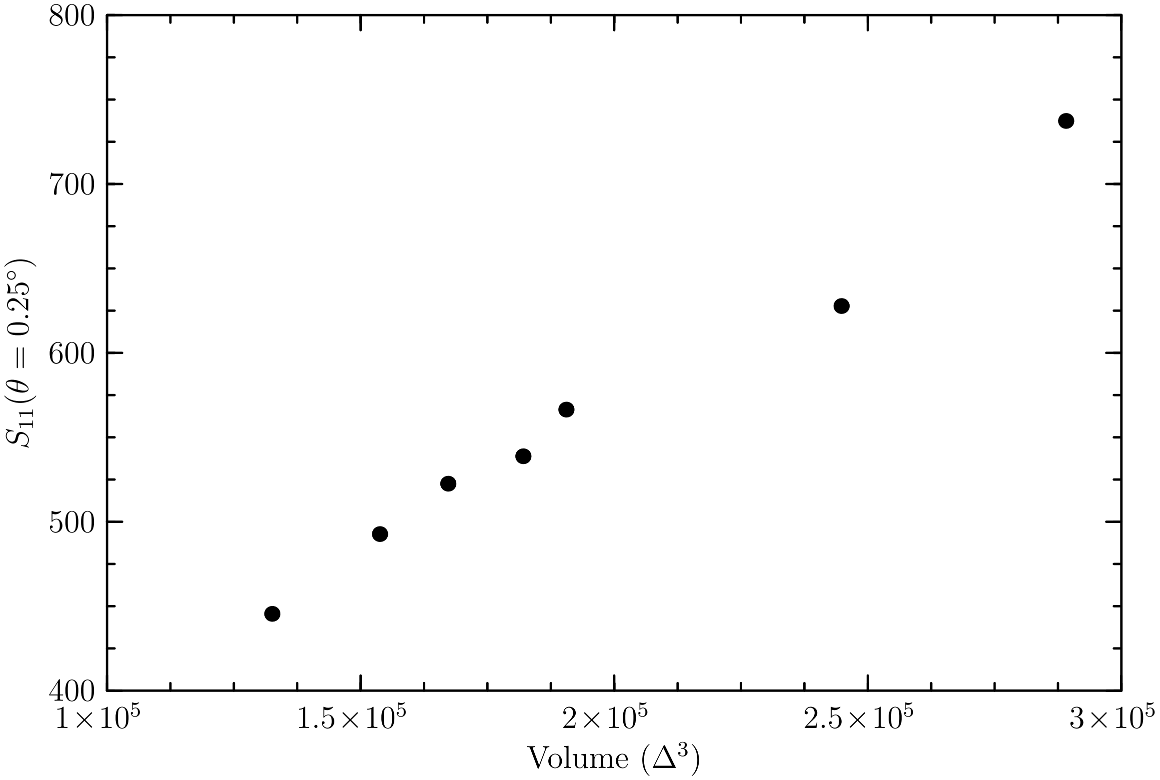

Figure 45: $S_{11}(\theta = 0.25°)$ vs. volume for each of the confocal models. This indicates that the forward scattering is influenced primarily by the volume for a given refractive index.

9.6 Comparison with an ellipsoidal model

A series of tests have been carried out to compare an ellipsoidal model with the confocal model for NALM6 cell #7. The ellipsoidal model consists of two ellipsoids, with one lying completely within the other. The inner ellipsoid has the same volume as the nucleus of the cell #7 model, and the outer ellipsoid has the same volume as that of the cell model. The axes of either ellipsoid are determined using the following process. First, the center of the (cell or nucleus) model is located, call this point o. Then the point on the surface of the model which is furthest from o is found, call this a. Next, the point on the surface which is furthest from the line containing both o and a is found, call it b. Finally, the point on the surface which is furthest from the plane containing o, a, and b is found, call it c. The axes of the ellipsoid will then have lengths of $2|o-a|$, $2|o-b|$, and $2|o-c|$. The ellipsoid is then scaled to have the same volume as that of the original model. Applying this process to both the cell membrane model and the nucleus model will result in two ellipsoids. The resulting ellipsoids are then oriented with respect to each other in a manner that aligns the axes with the points o, a, b, and c of the original models.

The simulations were carried out using a refractive indices of $1.3675 + i1.5 \times 10^{-5}$ for the cytoplasm, $1.4 + i1.5 \times 10^{-5}$ for the nucleus, and 1.35 for the host medium. The resolution was $\lambda_h/\Delta = 20$ and the number of time steps was equal to eight times that required for the incident field to travel across the heterogeneous region. Fig. 46 shows the Mueller matrix elements resulting from both the ellipsoidal and confocal image models. The ellipsoid model shows excellent agreement for S_{11}, S_{12}, and S_{33}. Further testing can be carried out to determine if this is coincidence or if in fact the ellipsoid model is suitable for determining these elements.

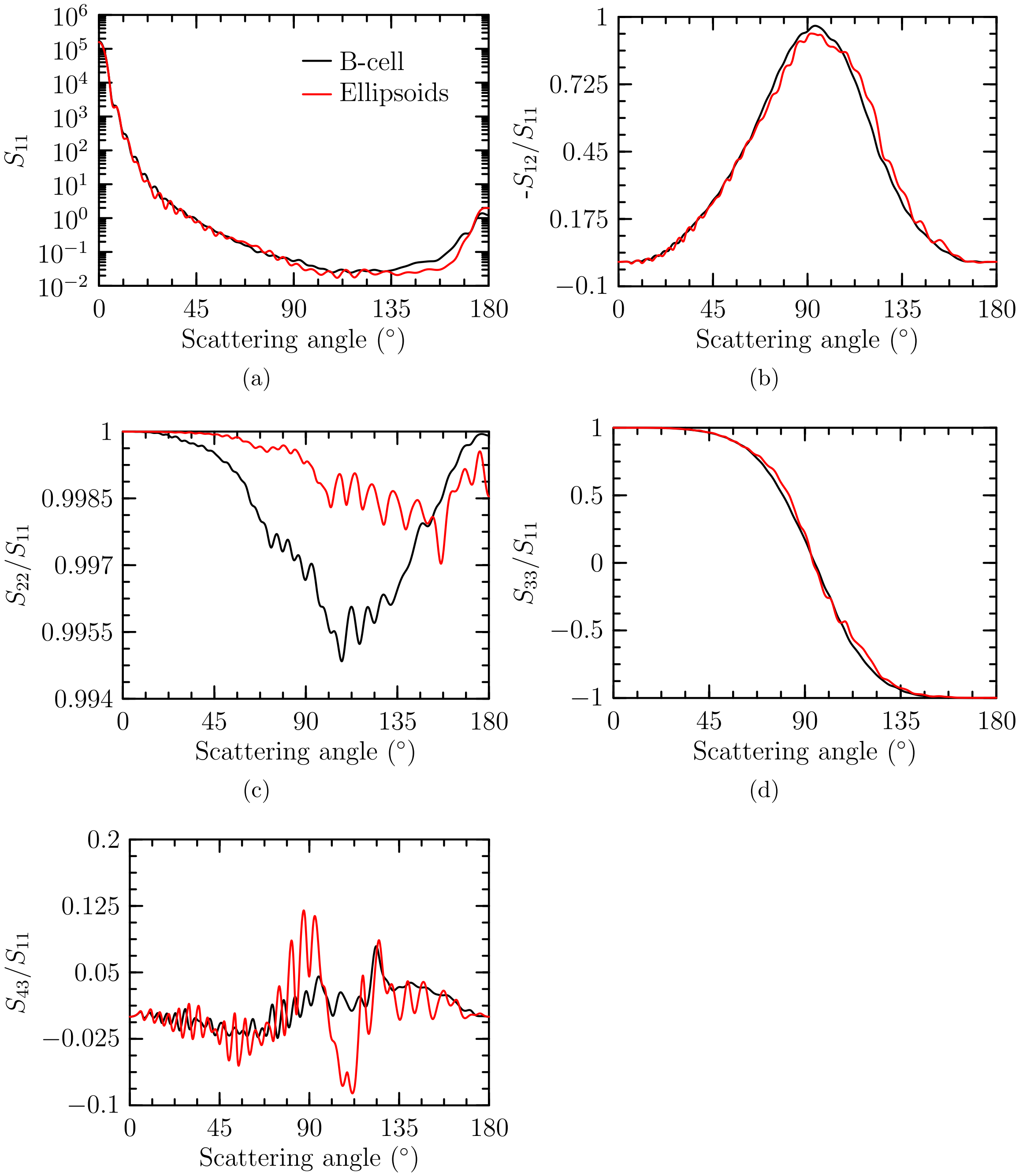

(a)

(b)

(c)

(d)

(e)

Figure 46: Comparison of the ellipsoids model with the cell #8 model. With the exception of S_{22}, the ellipsoids model is a good match for the B-cell model.

9.7 Dependence on the nucleus and refractive index

In the previous section, it was found that light scattering in the forward direction is influenced primarily by the volume and refractive index of the scattering particle. To isolate the effect of the refractive index, simulations with cell models using three different refractive indices for the nucleus have been carried out. The refractive indices are 1.3675, 1.4000, and 1.4325. Note that using 1.3675 as the refractive index effectively eliminates the nucleus since it is not optically distinct from the cytoplasm. In addition, results for the nucleus alone at refractive indices of 1.4000 and 1.4325 have also been obtained.

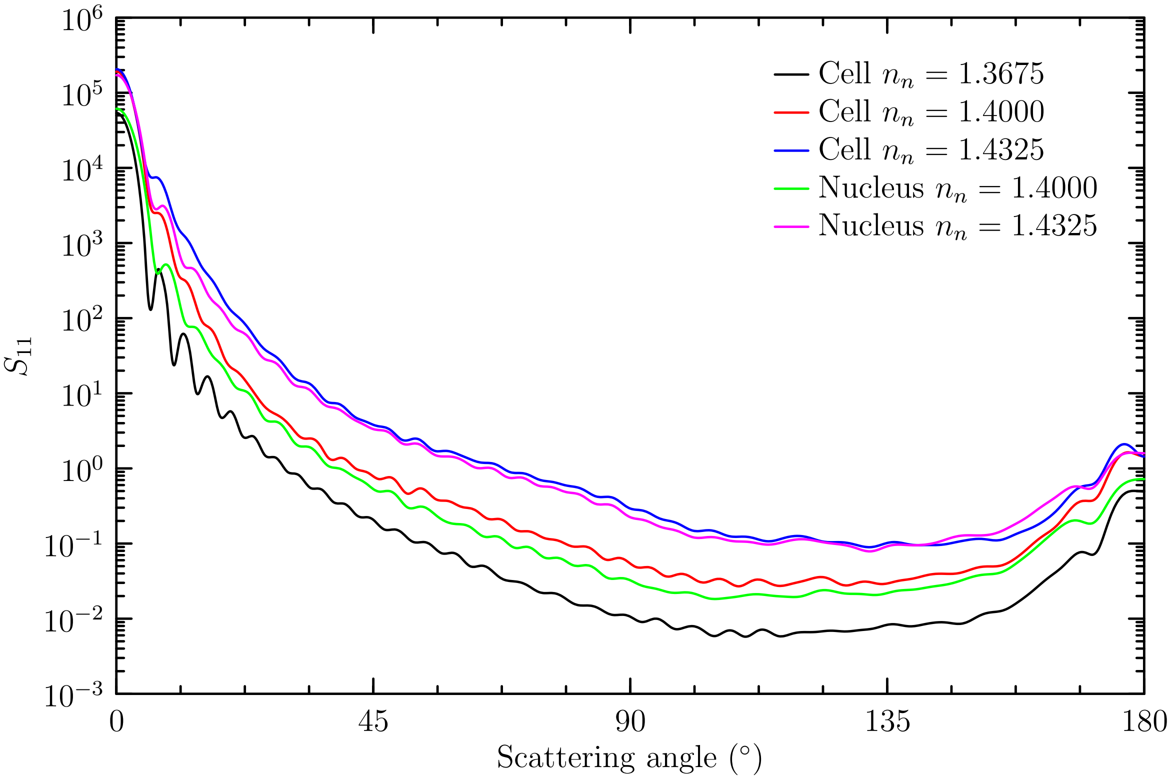

Figure 47: S_{11} result for the confocal model of cell #8 with various refractive indices for the nucleus. As the refractive index increases, the nucleus becomes the dominant factor in scattering intensity.

Fig. 47 shows the S_{11} results for the cell #8 model. It can be seen that the cell model with no nucleus scatters less than either model with a nucleus over the entire range. At $\theta < 5°$, the results for the models having a nucleus show little difference, indicating that the presence of a nucleus contributes significantly to the scattering in this region. Further, the difference between the results for the model with a nucleus and the model of the nucleus alone is less for the higher refractive index than for the lower. This indicates that as the refractive index increases, the nucleus becomes the primary influence on the scattering. The effect of the nucleus can also be seen in the scattering cross section results, shown in Fig. 48. For the model with a lower

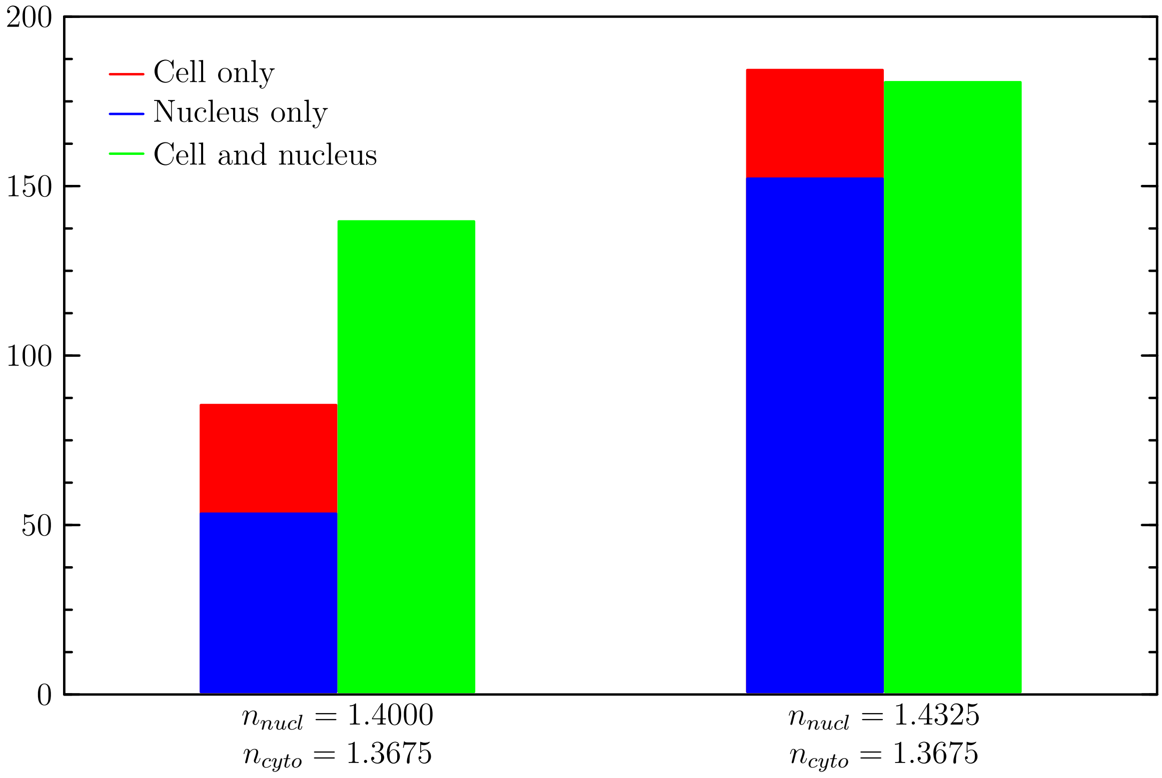

Figure 48: c_{sca} results for the confocal model of cell #8. Taking the sum of the cross sections for the cell and nucleus, shows that for the lower index, the cell and nucleus together act to scatter more light than the sum of the individual results. For the higher index, the nucleus is primarily responsible for the scattering.

index, the sum of the scattering cross sections for the nucleus and cell is a little more than half of the result for the cell with a nucleus, indicating that the presence of the nucleus within the cell model causes more scattering than can be accounted for by the nucleus alone. For the higher index, the nucleus dominates the scattering as the index increases, since the scattering by the nucleus alone is only a little less than the scattering by the cell with the nucleus. This can also be seen in the S_{11} result by looking at the difference between the cell models and the associated nucleus models. For the higher index, the difference for the higher index models is less than that of the lower index models over almost the entire range.

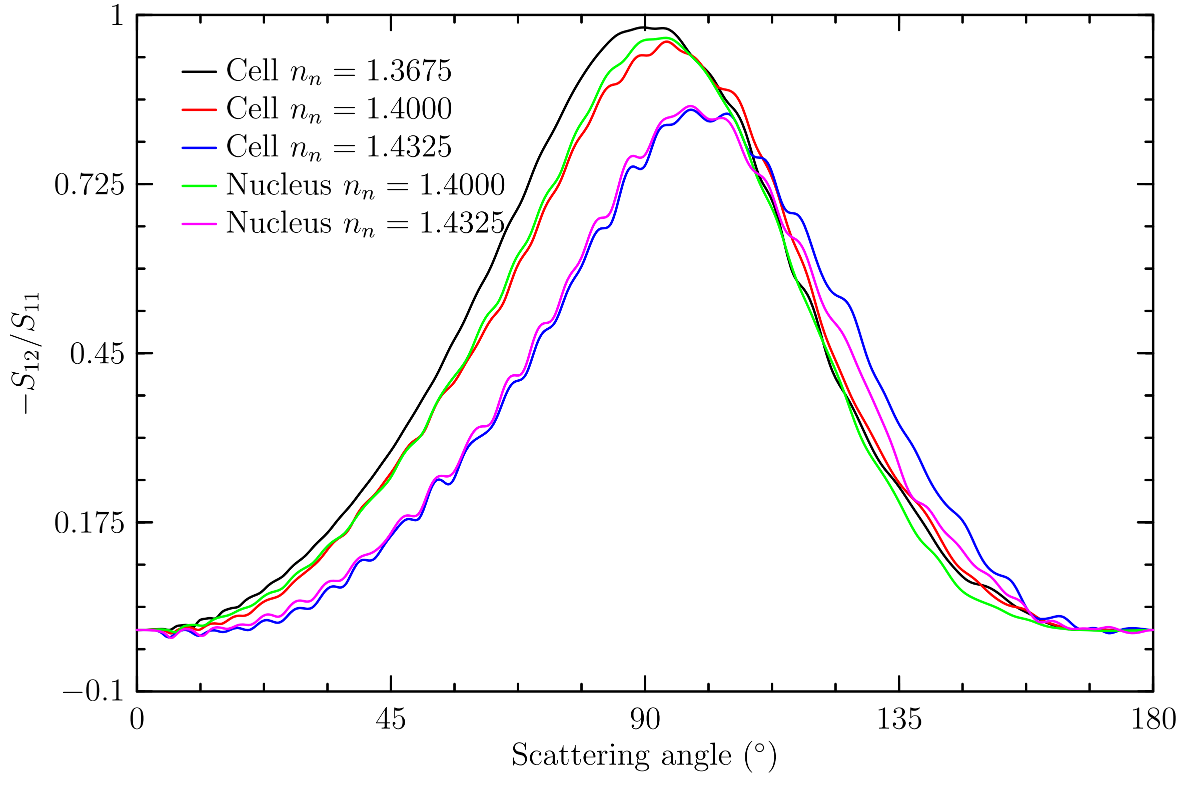

Figure 49: S_{12} result for the confocal model of cell #8 with various refractive indices. As the refractive index of the nucleus increases, the peak magnitude decreases and the peak shift to a wider angle.

Fig. 49 shows the S_{12} results for the cell #8 model, where another effect of the index of the nucleus can be seen. Like the S_{11} results, the S_{12} results show that the result for the models with the higher index show less difference than those of the lower index. In addition, the S_{12} result shows that as the index increases, the peak in the results shifts becoming lower and occurring at a wider angle. This information in conjunction with the information obtained from the S_{11} result could be used to determine the volume and refractive index of the cell.

The cell #1, cell #7, cell #9, and cell #10 models were all tested in the same manner as the cell #8 model. Analysis of these models is analogous to that of the cell #8 model and results in the same conclusions. Fig. 50 shows the S_{11}, S_{12}, and scattering cross section results for the cell #10 model for reference.

The effect of the nucleus and index of refraction can also be seen by analyzing the S_{11} result at particular scattering angles. Fig. 51 shows $S_{11}\,(\theta = 0.25°)$ vs. (a)$\int_{25°}^{45°} S_{11} d\theta$, (b)$\int_{90°}^{110°} S_{11} d\theta$, and (c)$\int_{158°}^{178°} S_{11} d\theta$ for all of the cell models with a nucleus having refractive index of 1.4000 and with the additional models having various refractive indices for cell #9 and cell #10. Each point in the plot represents the result at one of the twelve incident angles discussed previously. As expected, from the previous discussion, the models having the same index are separated vertically according to their respective volumes; also, some horizontal separation indicates that the scattering at $25° < \theta < 45°$ and $90° < \theta < 110°$ indicates a volume dependence as well. However, the models having a higher index of refraction have points separated by only a small amount vertically, but by a larger separation horizontally. Also, the horizontal separation is more pronounced with an increasing index. Together, these indicate the previous conclusion that volume is a primary factor in the forward scattering direction, but in addition, these data indicate that scattering at $25° < \theta < 110°$ is affected to a greater extent by the refractive index, rather than the volume. The data of these plots is typical of the type of data gathered by the use of flow cytometry. This gives another avenue into the determination of volume and index of refraction via the combination computational and experimental research.

Another phenomenon seen in Fig. 51 is the spread of the points for a particular cell. From the three-dimensional visualizations of Fig. 37, it can be seen that the nuclei of cell #9 and cell #10 have a more complex structure than those of the other cells. Again referring to Fig. 51, this manifests as a wider spread in the distribution of the points associated with these models when compared to those with a more spherical nuclear structure. This indicates that for cells with a complex nuclear structure, the difference in scattering results for the various angles is larger than those with the less complicated structure.

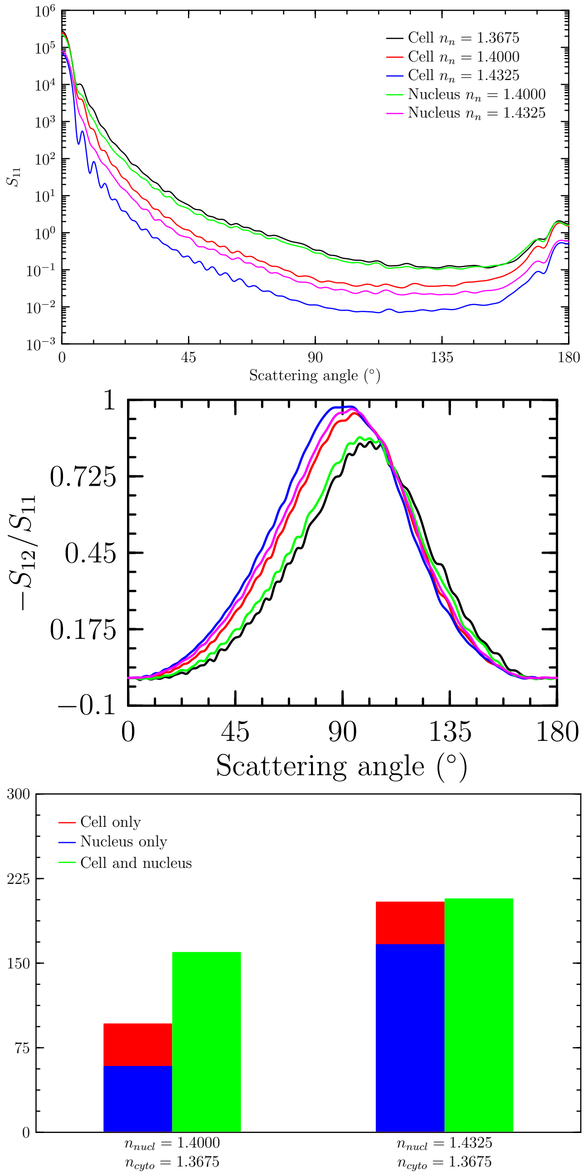

Figure 50: The results obtained using the confocal model of cell #10, lead to the same conclusions as those determined for cell #8, although cell #8 and cell #10 have nuclei which differ in shape.

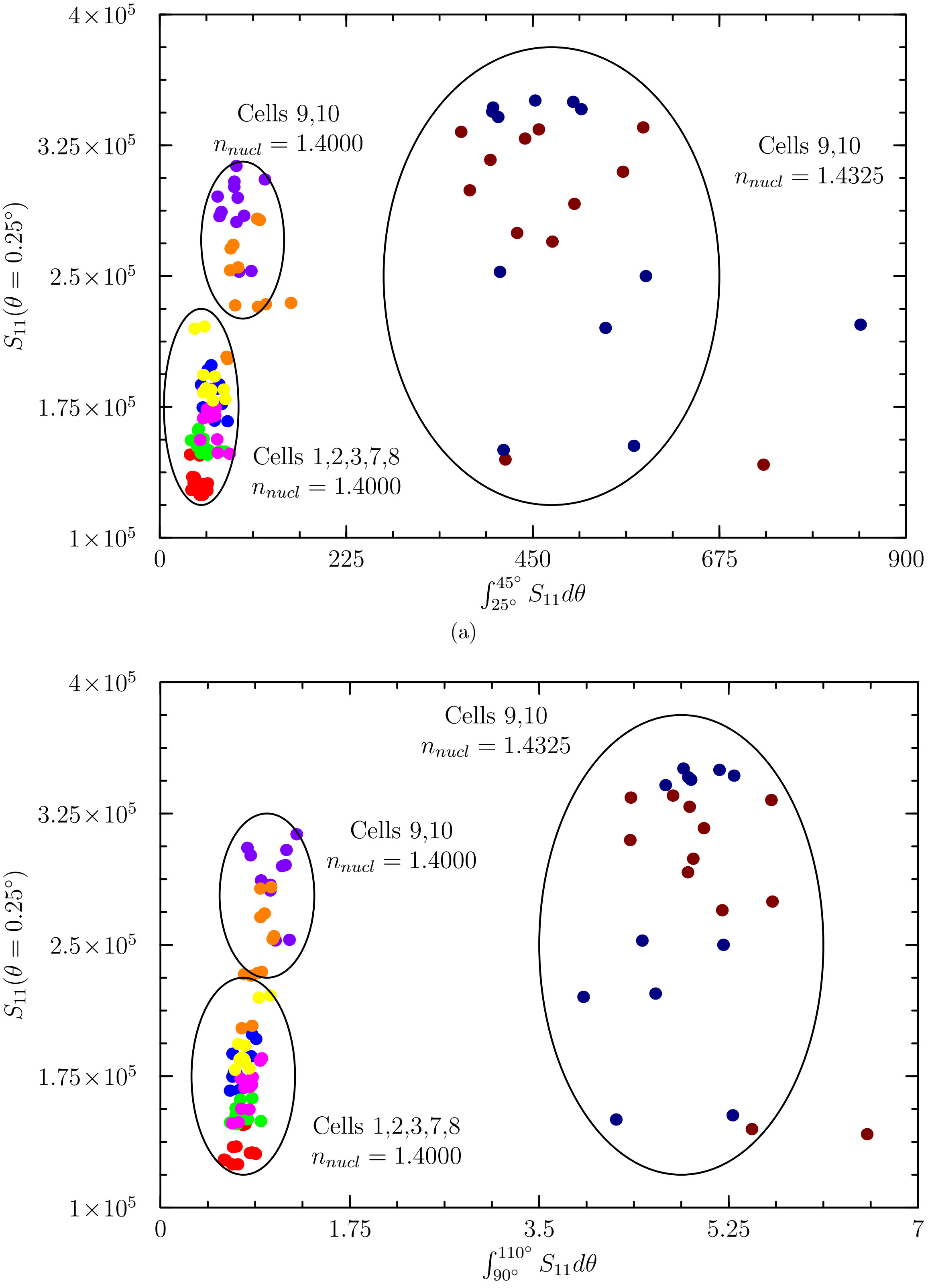
4×10^5
3.25×10^5
2.5×10^5
1.75×10^5
1×10^5
$S_{11}(\theta = 0.25°)$
0
225
450
675
900
$\int_{25°}^{45°} S_{11} d\theta$
Cells 9,10
$n_{nucl} = 1.4000$
Cells 9,10
$n_{nucl} = 1.4325$
Cells 1,2,3,7,8
$n_{nucl} = 1.4000$
4×10^5
3.25×10^5
2.5×10^5
1.75×10^5
1×10^5
$S_{11}(\theta = 0.25°)$
0
1.75
3.5
5.25
7
$\int_{90°}^{110°} S_{11} d\theta$
Cells 9,10
$n_{nucl} = 1.4325$
Cells 9,10
$n_{nucl} = 1.4000$
Cells 1,2,3,7,8
$n_{nucl} = 1.4000$

(a)

(b)

Figure 51

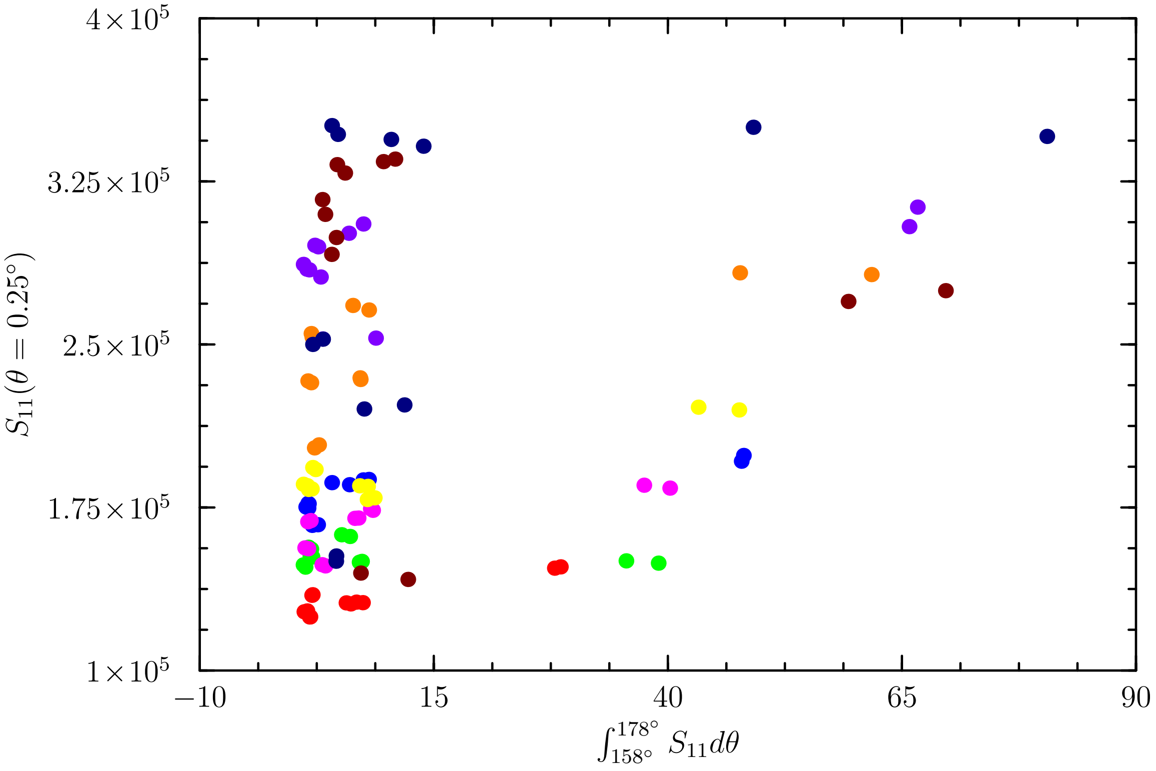

(c)

Figure 51: The scatter plot of $S_{11}(\theta = 0.25^\circ)$ vs. (a)$\int_{25^\circ}^{45^\circ} S_{11} d\theta$, (b)$\int_{90^\circ}^{110^\circ} S_{11} d\theta$, and (c)$\int_{158^\circ}^{178^\circ} S_{11} d\theta$. From (a) and (a) the cells having a complex nucleus or a higher refractive index can be identified.

9.8 Internal nuclear structure dependence

From the results presented in the previous section, it is apparent that internal structure, specifically the nucleus, has a direct effect on the scattering by cells. The next step in this investigation is to determine if structures within the nucleus will affect the scattering similarly. To test this, cell models with an inhomogeneous nucleus have been simulated. Recall from §9.2 that the intensity of the red component of the pixel data corresponds to the response of the SYTO 61 dye which is found in higher concentrations within the nucleus. Assuming that this concentration is associated with the refractive index allows structures within the nucleus to be modeled. Although further investigation is needed to determine the validity of such an assumption, this investigation can still show trends in scattering results due to the presence of internal structure.

To test the dependence on internal structure, four types of nucleus models are used. These will be referred to as the unfiltered model, the 0.71 model, the 0.90 model, and the 2-bin model. The unfiltered, 0.71, and 0.90 models are given internal structure by transforming the confocal images and removing the high frequency components (possibly none), which will be discussed. The 2-bin model also gives internal structure to the nucleus, but does so by dividing the pixels within the nucleus domain into two groups and assigning a different index of refraction to each one, also to be discussed.

Construction of the unfiltered, 0.71, and 0.90 models begins in the same manner as previously discussed, see §6, by analyzing the images and determining which pixels belong to the cytoplasm domain and which pixels belong to the nucleus domain. Next, the confocal images are transformed using a Fourier transform to give the spatial frequency components of the images. Then, a filter is applied to remove the high frequency components. This process is depicted in Fig. 52. Fig. 52b

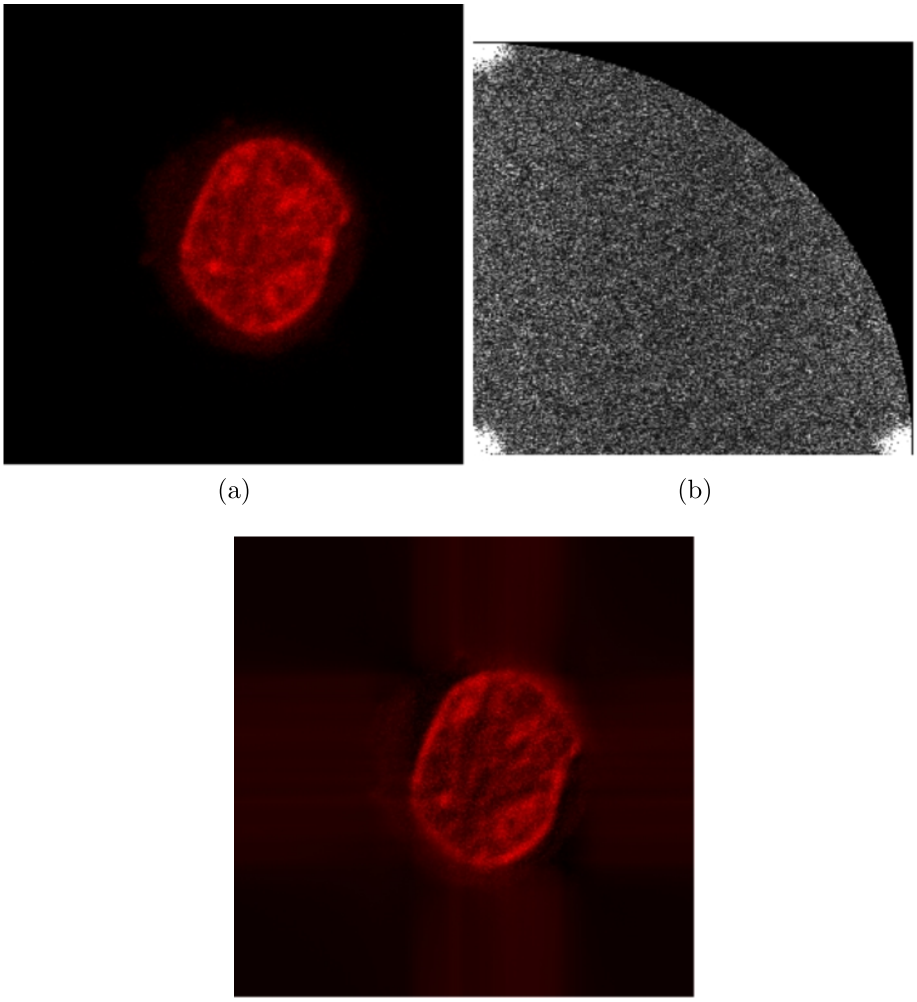

(a)

(b)

(c)

Figure 52: To simulate nuclear structure, the original image(a) is filtered by cutting out high-frequency componets. (c)The image obtained by applying the filter depicted in (b).

shows the transformed image with the filter applied. The difference between the unfiltered, 0.71, and 0.90 models is in the number of high frequency components removed. 0.71 and 0.90 refer to the length of the line segment "r" shown in the figure, and the unfiltered model has $r = 1$. Thus, the unfiltered image has no components removed, while the 0.90 model has fewer frequency components removed than the 0.71 model. Following the removal of the high frequency components, the altered image is transformed using an inverse Fourier transform to give a new spatial domain image, as seen in Fig. 52c. Comparison of the initial and final images shows that the final image has less variation in the intensity distribution, resulting in a more "clustered" structure within the nucleus. After the transformation, the various intensity values are associated with a refractive index. To do this, a function is derived which maps the intensity value to the refractive index according to constraints which limit the average and maximum difference of the refractive index values. More specifically, given an average refractive index of $\bar{n}$, a maximum difference of $\Delta\left(I_m - I_1\right)$, N_i points having intensity $I_i, i = 1, 2, \cdots, m$, and a characteristic function f, find n_i such that

$$\begin{gathered} \sum_i N_i n_i = \bar{n} \sum_i N_i \\ n_i = n_1 + \Delta \frac{f\left(I_i\right) - f\left(I_1\right)}{f\left(I_m\right) - f\left(I_1\right)}, \end{gathered} \tag{9.2}$$

which has the solution

$$n_i = \bar{n} + \frac{\Delta}{f\left(I_m\right) - f\left(I_1\right)} \left(f\left(I_i\right) - \frac{\sum_j N_j f\left(I_j\right)}{\sum_j N_j} \right). \tag{9.3}$$

The average refractive index used is 1.4000, and Δ is chosen as 0.04. Two characteristic functions have been used; the identity function, Id, and the natural logarithm, ln. Fig. 53 shows an example of the mapping using these characteristic functions.

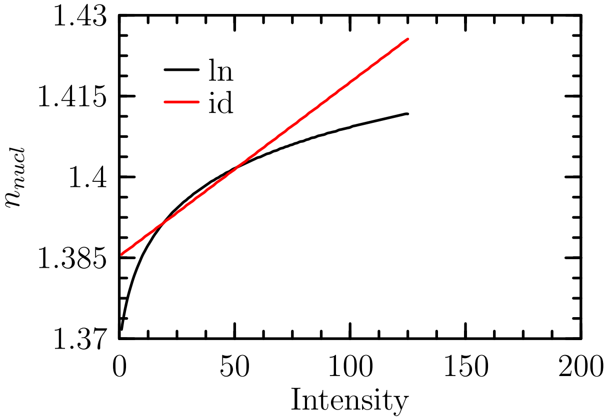

Figure 53: Two characteristic functions are used to determine the refractive index associated with the various intensities within the nucleus.

The construction process continues as previously described with the exception that voxels located between slides have an interpolated index of refraction rather than a strict inside/outside criterion.

Construction of the 2-bin model also begins in the same manner as previously described. Once the domains have been identified, the pixels of the nucleus domain are divided into two groups according to whether their associated intensities are higher or lower than some cut-off value. The pixels of higher intensity are given an index of refraction of 1.4325 and those of lower intensity are given an index of 1.3675. The cut-off value is determined such that the average refractive index is 1.4000. The construction process then continues with voxels located between slides assigned a value determined by whether the interpolated intensity is lower or higher than the cut-off value.

Fig. 54 shows model cross sections for the unfiltered, 0.71, and 2-bin models in the xy, xz, and yz planes passing through the center of the model. Since the original images are in the xy-plane, the best resolution is seen in this plane. The xz and yz planes show the blending of the data for voxels located between the images.

Simulations have been carried out using the cell #8 model with an inhomogeneous

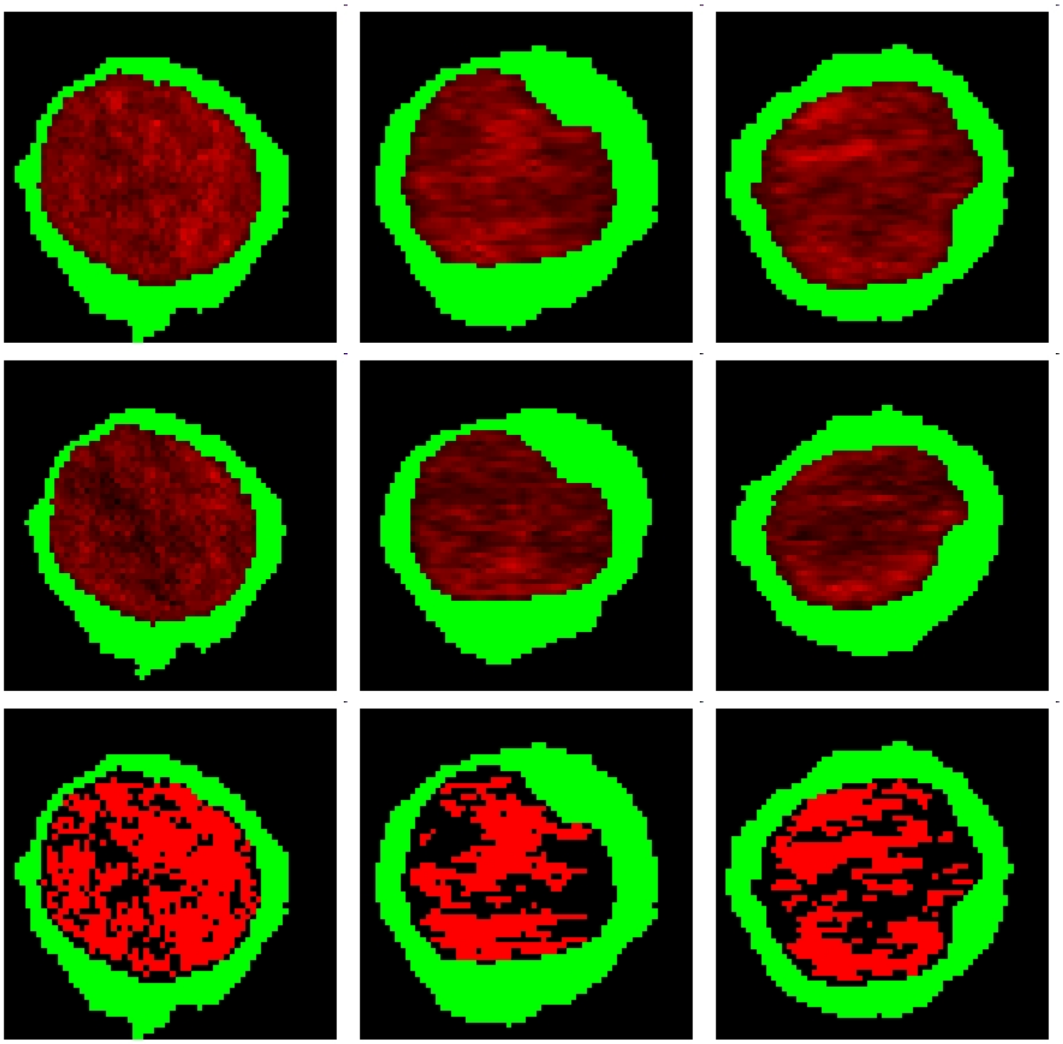

Figure 54: Domain images showing the nuclear structure resulting from (top row)no filtering, (middle row)$r = 0.71(\ln)$ filtering, and (bottom row) a 2-bin model. Three different cross-sections are shown, (left column)xy-plane, (middle column)xz-plane, and (right column)yz-plane.

nucleus. The nucleus models used are the unfiltered, 0.71 Id, 0.71 ln, and 0.90 ln models. A 2-bin model has been constructed, but results have not yet been obtained for this model. Fig. 55 shows a comparison of S_{11} and S_{12} for the homogeneous, 0.71 Id, and 0.71 ln models. The results are almost identical and there is no obvious way to discriminate between any of the models. This could be due to the choice of $\Delta = 0.04$ resulting in a "smooth" spatial distribution in the index of refraction. Fig. 57 shows the comparison for all of the ln model results along with the homogeneous result. Like Fig. 55, there is little difference in the scattering by the various models.

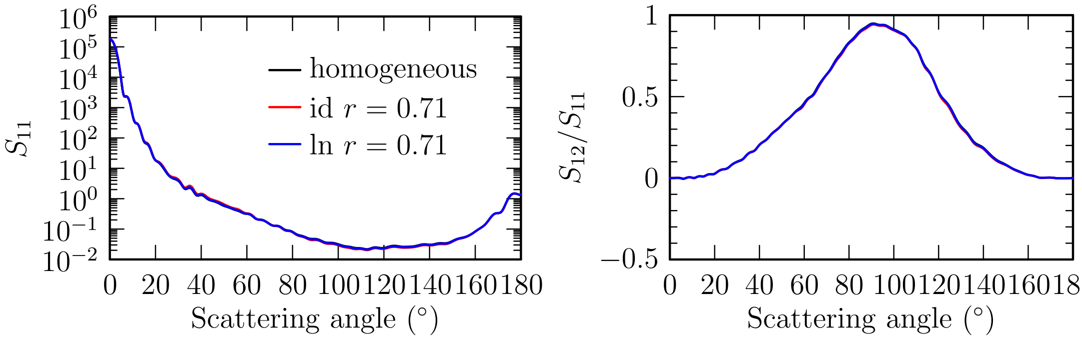

Figure 55: The natural log and identity models

Figure 56: Little difference can be seen in S_{11}(left) and S_{12}(right) for natural log and identity models.

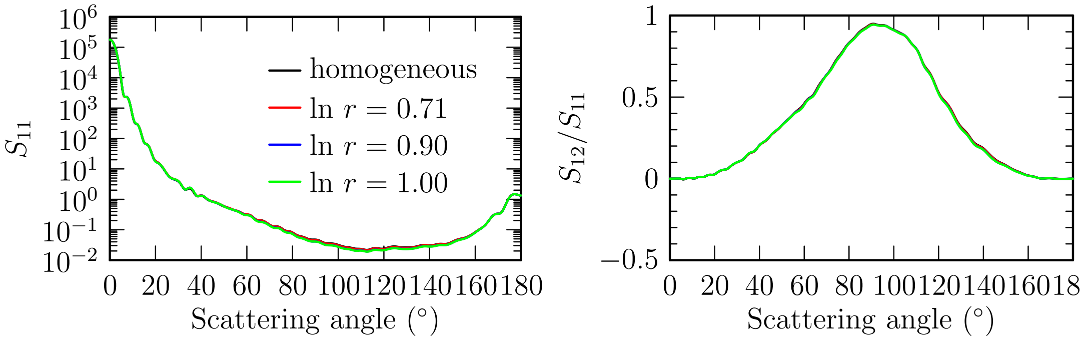

Figure 57: Little difference can be seen in S_{11}(left) and S_{12}(right) for natural log models created with differing filters.

The other Mueller matrix elements also show little difference between the various models.

Recall from the previous section that a plot of $S_{11}\left(\theta = 0.25°\right)$ vs. $S_{11}\left(\theta = 35°\right)$ allowed discrimination between nuclei having various refractive indices. Fig. 58 shows $S_{11}\left(\theta = 0.25\right)$ vs. $\int_{25°}^{45°} S_{11}\left(\theta\right) d\theta$ for the homogeneous and inhomogeneous models of cell #8. Using this analysis is also not helpful in distinguishing the various models.

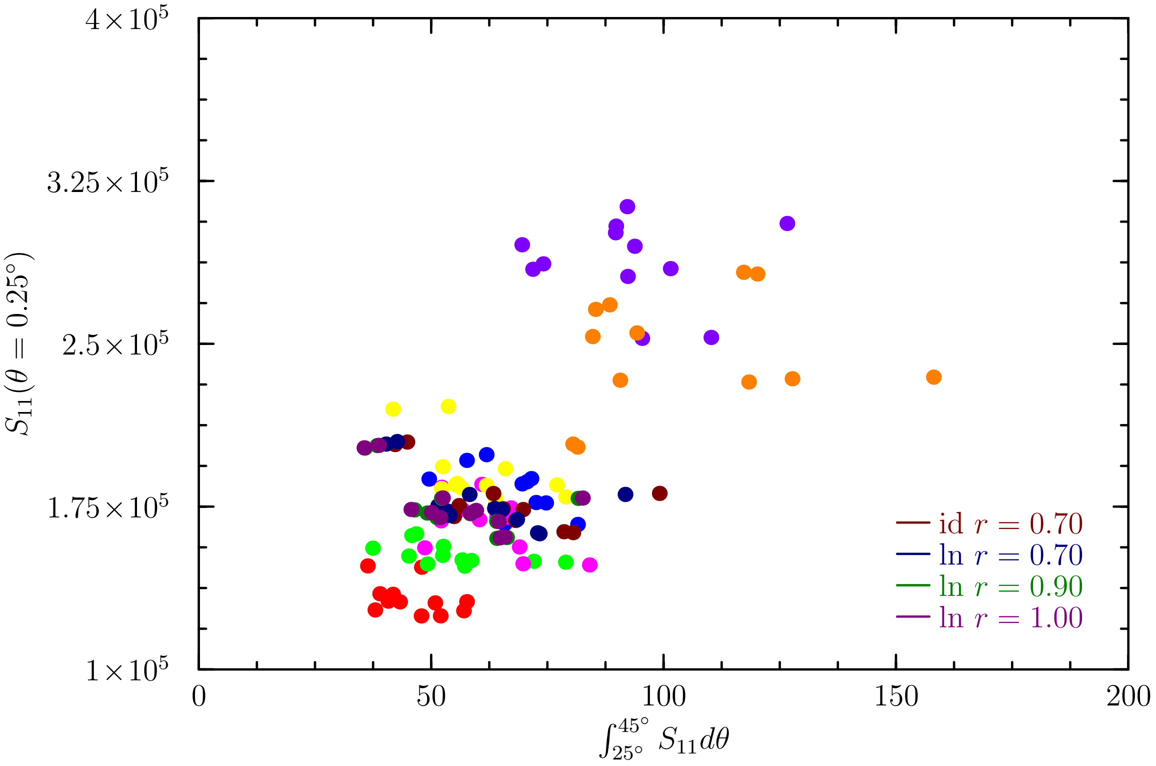

Figure 58: Forward vs. $25° - 45°$ scattering shows that the models having an inhomogeneous nucleus are not distinguishable from those having a homogeneous nucleus.

Recall from Eq. (2.6) that a change in ε results in a different scattered field. Although the scattered field must be different for the various models, this difference is not obvious in the Mueller matrix elements. Further investigation using a larger value for Δ or using an additional stochastic process to determine the refractive index between slides may help in understanding the circumstances under which observable changes in the Mueller matrix will occur.

9.9 Comparison with experimental results

Experiments to determine the Mueller matrix for NALM6 cells have been carried out at the Biomedical Laser Laboratory at East Carolina University[13]. The cells used in the experiment are from the same cell line, NALM6, and from the same source as those used for the computational results. A dilute solution of about $2.34 \times 10^2 cells/\mu L$ was used to obtain results that approximate those of single scattering events. For experimental details refer to [13].

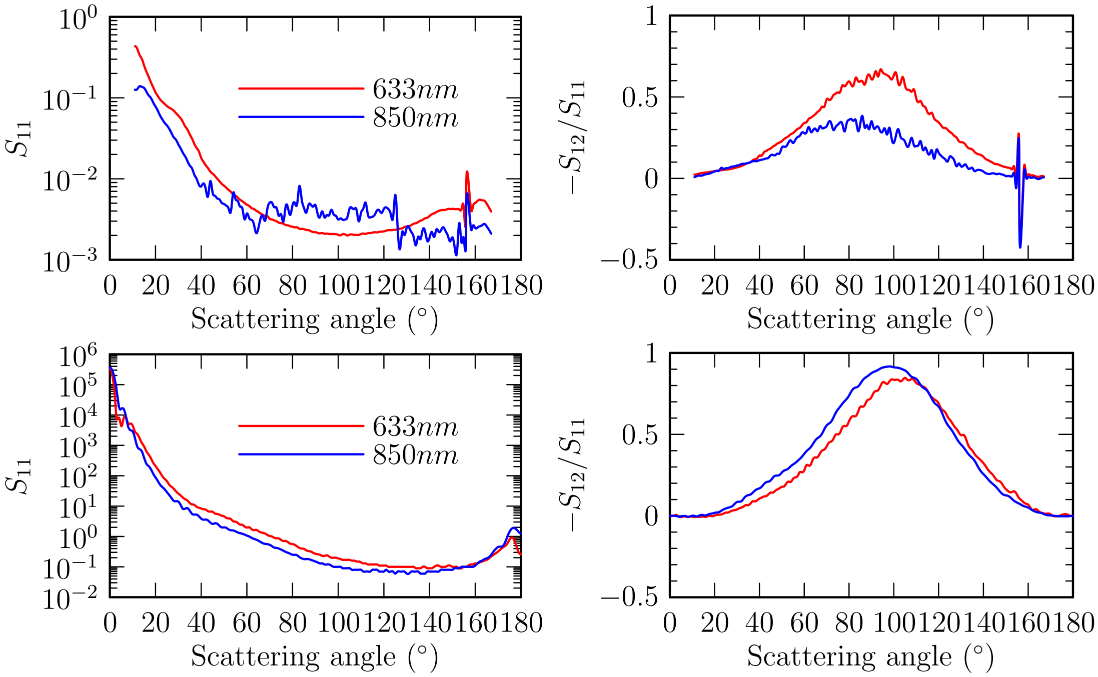

Figure 59: The experimental results(top) and simulation results(bottom) differ in behavior. For S_{11} the 850nm and 633nm curves show differences in the sidescattering region. For S_{12}, both show a peak shift to the right for the lower wavelength; however, the magnitude peaks are not in agreement.

Fig. 59 shows the experimental results for wavelengths of 850nm and 633nm along with the FDTD results for the cell #8 model. For the FDTD simulations at 850nm, 1.330[13] was used as the refractive index of the host medium, 1.368 for the cytoplasm[9], and 1.400[8] for the nucleus. For the simulations at 630nm, 1.336 was used as the refractive index of the host medium, 1.380 for the cytoplasm, and 1.430 for the nucleus. The S_{11} results differ in the side scattering region, $60° < \theta < 120°$, where the experimental results show that the $850nm$ scattering is greater than that of $633nm$. The S_{12} results are also quite different. The experimental result shows the peak for the $850nm$ result is lower and to the left of that of the $633nm$ result; while the FDTD result shows the $850nm$ peak being higher and to the right of that of the $633nm$. One possible reason for the differences is that the computational results are for a single cell, whereas the experimental results are for a large group of cells. Although the experimental results approximate single scattering, the result is an average result of many approximate single scattering events. Another possibility is that some physical cell structure that is not modeled in the simulation, such as the cell membrane, affects the scattering to an extent that significantly changes the results.

Further investigation is needed to resolve the differences between the experimental results and computational results. Such investigation could include adding a cell membrane and/or an endoplasmic reticulum to the cell model. Previous studies show that the cell membrane has a refractive index of 1.46[28], significantly higher than that of the cytoplasm, 1.36. Future investigation could also vary the refractive index of each component of the cell model to determine the influence on the scattering.

Chapter 10: Conclusion

Understanding light scattering from biological cells is critical to furthering research that will help in the diagnosis and treatment of diseases such as cancer. Because most biological cells have size parameters approximately the same as the wavelength of the light used to analyze them, the wave nature of the light must be taken into account when modeling the light-cell interaction. A program has been developed to simulate the interaction and return results in the form of cross sections, anisotropy factor, and Mueller matrix. The program implements the FDTD method, which was chosen for suitability in simulating scattering from particles with sizes over a range which includes most biological cells. Parallel methods have been employed, allowing more computational resources to be used in simulating the interaction.

The basis of the FDTD method is the replacement of continuous derivative operators with finite difference operators. This allows systems having complicated shapes to be simulated without having to obtain simultaneous solutions and without having to use complicated boundary conditions at the "edges" of the scattering particle. The method has been in use in many areas of research for decades and thus has large body of supporting literature and development. The implementation of the FDTD method uses a cubic grid which allows parallel methods to be easily implemented along planes of the grid. The program has been validated against Mie theory calculations. Berrenger's perfectly matching layer absorbing boundary condition is used to terminate the grid. The simulation time and parallel efficiency have also been evaluated, and it was shown that the program can produce realistic scattering results within a reasonable time frame.

Models of red blood cells having various shapes, due to pressure, have been created. Simulations using the models have shown that the shape of the scattering particle is a primary factor in the scattering of light. However, it was found that for practical purposes, further study is needed to be able to distinguish these shapes according to their "average" behavior. These simulations also gave evidence that the peaks and valleys of the S_{11} matrix element are related to the symmetry of the particle.

Two other programs have been created to model cells using confocal images. One of these uses the data obtained from the confocal microscope to produce a set of domain images. The other takes the domain images and produces a three-dimensional model. These models are then input into the FDTD program along with the refractive index values. Seven different B-cell models have been created. The results of the simulations carried out using these models have shown that both homogeneous and coated sphere models are not suitable substitutes for actual B-cell models when determining the Mueller matrix elements at scattering angles greater than 20°. An ellipsoid model has also been tested, and it was found that the ellipsoid model is suitable for the calculation of matrix elements S_{11}, S_{12}, and S_{33}. Using all of the models, it was shown that scattering at small angles is influenced primarily by the global properties of the shape of the scattering particle such as the volume and the presence of the nucleus. The dependence on small scale properties such as variations in the refractive index of the nucleus was also tested. A comparison of the results showed little difference for various nuclei simulated; however, the variation in the refractive index was small and further testing may reveal differences when using larger variations. Finally, a comparison with experimental results revealed discrepancies. Further computational testing using average Mie theory results showed the same behavior as that of the FDTD results. Further experimental data and more comprehensive B-cell simulation (using more than seven models) are needed to resolve these discrepancies.

Bibliography

[1] V. Backman, R. Gurjar, K. Badizadegan, I. Itzkan, R. Dasari, l. Perelman, and M. Feld. Polarized light scattering spectroscopy for quantitative measurement of epithelial cellular structures *in situ*. *IEEE Journal of Selected Topics in Quantum Electronics*, 5:1019–1026, 1999.

[2] C. Bohren and D. Huffman. *Absorption and scattering of light by small particles.* John Wiley & Sons, New York, 1983.

[3] A. G. Borovoi, E. I. Naats, and U. G. Oppel. Scattering of light by a red blood cell. *Journal of Biomedical Optics*, 3:364–372, 1998.

[4] C. D. Bortner and J. A. Cidlowski. *Methods in Cell Biology*, chapter Flow cytometric analysis of cell shrinkage and monovalent ions during apoptosis. Academic Press, San Diego, 2000.

[5] R. S. Brock, X.-H. Hu, P. Yang, and J. Q. Lu. Evaluation of a parallel FDTD code and application to modeling of light scattering by deformed red blood cells. *Optics Express*, 13:5279–5292, 2005.

[6] R. S. Brock, X.-H. Hu, D. A. Weidner, J. R. Mourant, and J. Q. Lu. Effect of detailed cell structure on light scattering distribution: FDTD study of a B-cell with 3D structure reconstructed from confocal images. *Journal of Quantitative Spectroscopy & Radiative Transfer*, 102:25–36, 2006.

[7] J. P. Brooks, K. K. Ghosh, E. Harrigan, D. S. Katz, and A. Taflove. *Computational electromagnetics and supercomputer architecture, PIERS*, chapter Progress in Cray-based algorithms for computational electromagnetics, pages 23–55. EMW Publishing, 1993.

[8] A. Brunsting and P. Mullaney. Differential light scattering from spherical mammalian cells. *Biophysical Journal*, 14:439–453, 1974.

[9] J. Bruthan, O. Minet, J. Helfmann, M. Herrig, and G. Muller. The spatial variation of the refractive index in biological cells. *Physics in Medicine and Biology*, 41:369–382, 1996.

[10] C. Chen, J. Q. Lu, H. Ding, K. M. Jacobs, Y. Du, and X.-H. Hu. A primary method for determination of optical parameters of turbid samples and application to intralipid between 550 and 1630 nm. *Optics Express*, 14:7420–7435, 2006.

[11] K. C. Chew and V. F. Fusco. A parallel implementation of the finite-difference time-domain algorithm. *International Journal of Numerical Modeling: Electronic Networks, Devices and Fields*, 8:293–299, 1995.

[12] K. S. de Boer, M. A. Jura, and M. J. Shull. *Exploring the universe with the IUE satellite*, chapter Diffuse and dark clouds in the interstellar medium, pages 485–515. D. Reidel Publishing Co., Dordrecht, 1987.

[13] H. Ding, J. Q. Lu, R. S. Brock, T. J. McConnell, J. F. Ojeda, K. M. Jacobs, and X.-H. Hu. Angle-resolved Mueller matrix study of light scattering by B-cells at three wavelengths of 442, 633 and 850nm. *Journal of Biomedical Optics*, to be published.

[14] R. Drezek, A. Dunn, and R. Richards-Kortum. Light scattering from cells: finite-difference time-domain simulations and goniometric measurements. *Applied Optics*, 38:3651–3661, 1999.

[15] P. S. Excell, A. D. Tinniswood, and K. Haigh-Hutchinson. Parallel computa-

tion of large-scale electromagnetic field distributions. *Applied Computational Electromagnetics Society Journal*, 13:179–187, 1998.

[16] S. D. Gedney. Finite-difference time-domain analysis of microwave circuit deviceson high performance vector/parallel computers. *IEEE Transactions on Microwave Theory and Techniques*, 43:2510–2514, 1995.

[17] G. H. Goedecke and S. G. OBrien. Scattering by irregular inhomogeneous particles via the digitized Greens function algorithm. *Applied Optics*, 15:2431–2437, 1988.

[18] R. Guerrieri, R. K. Tadros, J. Gamelin, and A. Neureuther. Massively parallel algorithms for scattering in aptical lithography. *IEEE Trans. Computer-Aided Design*, 10:1091–1100, 1991.

[19] A. Hoekstra, B. Hertzberger, and P. Sloot. The optical "fingerprints" of cells: Catching the bad guys. *IEEE Computational Science & Engineering*, 3:4–5, 1996.

[20] A. G. Hoekstra, V. P. Maltsev, and G. Videen, editors. *Optics of Biological Particles*. Springer, London, 2007.

[21] H. Hoteit, R. Sauleau, B. Philippe, P. Coquet, and J. P. Daniel. Vector and parallel implementations for the FDTD analysis of millimeter wave planar antennas. *International Journal of High Speed Computing*, 10(2):209–234, 1999.

[22] H. R. Hurwitz, J. Hozier, T. LeBien, J. Minowada, K. Gajl-Peczalska, I. Kubonishi, and J. Kersey. Characterization of a leukemic cell line of the pre-B phenotype. *International Journal of Cancer*, 23:174–180, 1979.

[23] J. D. Jackson. *Classical Electrodynamics*. John Wiley & Sons, New York, 3 edition, 1998.

[24] J. Q. Lu, P. Yang, and X.-H. Hu. Simulations of light scattering from a biconcave red blood cell using the FDTD method. *Journal of Biomedical Optics*, 10:2431–2437, 2005.

[25] J. Q. Lu, R. S. Brock, P. Yang, and X.-H. Hu. *Optics of Biological Particles*, chapter Modeling of light scattering by single red blood cells with an FDTD method. Springer, London, 2007.

[26] J. Lumpp, S. K. Maxumdar, and S. D. Gedney. Performance modeling of the finite-difference time-domain method on parallel systems. *ACES Journal*.

[27] X. Ma, J. Q. Lu, R. S. Brock, K. M. Jacobs, P. Yang, and X.-H. Hu. Determination of complex refractive index of polystyrene microspheres from 370 to 1610 nm. *Physics in Medicine and Biolog*, 48:4165–4172, 2003.

[28] J. Maier, S. Walker, S. Fantini, M. Franceschini, , and E. Gratton. Possible correlation between blood glucose concentration and the reduced scattering coefficient of tissues in the near infrared. *Optics Letters*, 19:2062–2064, 1994.

[29] V. P. Maltsev. Scanning flow cytometry for individual particle analysis. *Review of Scientific Instruments*, 71:243–255, 2000.

[30] J. Mourant, A. Hielscher, A. Eick, T. Johnson, and J. Freyer. Evidence of intrinsic differences in the light scattering properties of tumorigenic and nontumorigenic cells. *American Cancer Society*, 84:366–374, 1998.

[31] J. Mourant, T. M. Johnson, S. Carpenter, A. Guerra, T. Aida, and J. P. Freyer. Polarized angular dependent spectroscopy of epithelial cells and epithelial cell nuclei to determine the size scale of scattering structures. *Journal of Biomedical Optics*, 7:378–387, 2002.

[32] A. Nilsson, P. Alsholm, A. Karlsson, and S. Andresson-Engels. T-matrix computations of light scattering by red blood cells. *Applied Optics*, 37:2735–2748, 1998.

[33] A. Perlik and S. Moraites. *Computational electromagnetics and supercomputer architecture, PIERS*, chapter Electromagnetic wave analysis using FD-TD and its implementation on the connection machine, pages 266–308. EMW Publishing, 1993.

[34] A. Perlik, T. Opsahl, and A. Taflove. Predicting scattering of electromagnetic fields using FD-TD on a connection machine. *IEEE Trans. Magnetics*, 25:2910–2912, 1989.

[35] G. C. Salzman, S. B. Singham, R. G. Johnston, and C. F. Bohren. *Flow Cytometry and Sorting*, chapter 5. John Wiley & Sons, New York, 2 edition, 1990.

[36] T. W. Secomb, R. Skalak, N. Ozkaya, and J. F. Gross. Flow of axisymmetric red blood cells in narrow capillaries. *The Journal of Fluid Mechanincs*, 163:405–423, 1986.

[37] T. W. Secomb, R. Hsu, and R. Pries. Motion of red blood cells in a capillary with an endothelial surface layer: effect of flow velocity. *American Journal of Physiology - Heart and Circulatory Physiology*, 381:H629–H636, 2001.

[38] R. Skalak and P. I. Branemark. Deformation of red blood cells in capillaries. *Science*, 164:717–719, 1969.

[39] G. Streekstra, A. Hoekstra, E. Nijhof, , and R. Heethaar. Light scattering by red blood cells in ektacytometry: Fraunhofer versus anomalous diffraction. *Applied Optics*, 32:2266–2272, 1993.

[40] A. Taflove. *Classical Electrodynamics.* John Wiley & Sons, New York, 1998.

[41] S. Tanev, W. Sun, R. Zhang, and A. Ridsdale. The fdtd approach applied to light scattering from single biological cells. volume 5474, pages 162–168. SPIE, 2004.

[42] J. A. Terzakis. Distinguishing B and T lymphocytes by scanning electron microscopy. *Ultrastructural Pathology*, 24:205–209, 2000.

[43] O. B. Toon and T. P. Ackerman. Algorithms for the calculation of scattering by stratified spheres. *Applied Optics*, 20:3657–3660, 1981.

[44] V. Varadarajan and R. Mittra. Finite-difference time-domain analysis using distributed computing. *IEEE Microwave and Guided Wave Letters*, 4:144–145, 1994.

[45] G. Videen and D. Ngo. Light scattering multipole solution for a cell. *Journal of Biomedical Optics*, 3:212–220, 1998.

[46] P. Yang and K. N. Liou. Finite-difference time domain method for light scattering by small ice crystals in three-dimensional space. *Journal of the Optical Society of America A*, 13:2072–2085, 1996.

[47] S. K. Yee. Numerical solutions of initial boundary problems involving Maxwell's equations in isotropic materials. *IEEE Transactions on Antennas and Propagation*, 14.

[48] M. A. Yurkin, A. G. Hoekstra, R. S. Brock, and J. Q. Lu. Systematic comparison of the discrete dipole approximation and the finite difference time domain method. In preparation, 2007.

[49] P. R. Zarda, S. Chien, and R. Skalak. Elastic deformations of red blood cells. *Journal of Biomechanics*, 10:211–221, 1977.

[50] P. R. Zarda, S. Chien, and R. Skalak. *Computational Methods for Fluid-Solid Interaction Problems*, chapter Interaction of viscous incompressible fluid with an elastic body, pages 65–82. American Society of Mechanical Engineers, New York, 1977.